

1.47 187**8**

MICHIGAN STATE UNIVERSITY LIBRARIES
3 1293 01026 9862

This is to certify that the

dissertation entitled
NMR INVESTIGATIONS OF CHEMICAL SHIELDING,
STRUCTURE, AND MULTIPLE QUANTUM-DYNAMICS

OF APATITES presented by

Gyunggoo Cho

has been accepted towards fulfillment of the requirements for

Ph.D degree in Chemistry

Date 29 Sept. 1993

MSU is an Affirmative Action/Equal Opportunity Institution

0-12771

James L. Alge Major professor

LIBRARY Michigan State University

PLACE IN RETURN BOX to remove this checkout from your record.

TO AVOID FINES return on or before date due.

DATE DUE	DATE DUE	DATE DUE

MSU is An Affirmative Action/Equal Opportunity Institution

NMR INVESTIGATIONS OF CHEMICAL SHIELDING, STRUCTURE, AND MULTIPLE-QUANTUM DYNAMICS OF APATITES

by

Gyunggoo Cho

A DISSERTATION

Submitted to Michigan State University in partial fulfillment of the requirements for the degree of

DOCTOR OF PHILOSOPHY

Department of Chemistry

1993

ABSTRACT

NMR INVESTIGATIONS OF CHEMICAL SHIELDING, STRUCTURE, AND MULTIPLE-QUANTUM DYNAMICS OF APATITES

by

Gyunggoo Cho

The ¹⁹F MAS-NMR spectra of a series of fluorapatites, $M_5F(PO_4)_3$, where M = Ca^{2+} , Sr^{2+} and Ba^{2+} , and solid solutions of Ca/Sr fluorapatite have been obtained. The crystallographic symmetry about the fluoride ions requires that the chemical shielding tensors be axially symmetric. The principal components of the ¹⁹F shielding tensor of $M_5F(PO_4)_3$ are obtained from ¹⁹F MAS-NMR spectra using the moments method and Herzfeld and Berger graphical method. The usefulness of these two methods is demonstrated by using the comparison between experimental spectra and simulated spectra obtained from the chemical shielding tensors. The measured chemical shielding tensors enable us to separate the contributions to the Ramsey paramagnetic shielding term from the sigma- and pibonding between the alkaline earth metal ions and the fluoride ions. The values of sigma- and pi-bonding contributions to ¹⁹F shielding for $M_5F(PO_4)_3$ (M = Ca^{2+} , Sr^{2+} and Ba^{2+}) are 81.7 ppm and 24.6 ppm, 97.6 ppm and 26.0 ppm, and 138.4 ppm and 32.1 ppm respectively with respect to free fluoride ion.

The preference of Sr²⁺ ions for the Ca(2) site for fluorapatite have been studied using ¹⁹F MAS-NMR spectra of a solid solution of composition

Ca_{8.97}Sr_{1.03}F₂(PO₄)₆. The peak intensities obtained from the centerband and sidebands as well as the deconvolution peak indicate that Sr²⁺ ions have a 23% preference for the Ca(2) site, which is adjacent to the fluoride ion. The assignment of the spectra of Ca_{8.97}Sr_{1.03}F₂(PO₄)₆ is aided by the existence of spin diffusion performed by the SPARTAN pulse sequence.

The dimensionality of the distribution of spins in solids influences their multiplequantum NMR dynamics. We have studied these dynamics for the quasione-dimensional distribution of uniformly spaced proton spins in hydroxyapatite. Ca₅(OH)(PO₄)₃, and related compounds, using a phase-incremented even order selective MQ pulse sequence. The increase in effective size N with preparation times for stoichiometric monoclinic hydroxyapatite is linear at early times, in agreement with calculations based on the incremental shell model; however, the experimental slope is three times greater than the predicted slope. An upward curvature observed at longer preparation times is qualitatively ascribed to the incomplete isolation of linear chains. A slight deficiency of hydroxyl groups in a sample of hydroxyapatite in the commonly-occurring hexagonal crystal form leads to a measurable decrease in the slope of the linear portion of the curve. The ¹H multiple-quantum dynamics of a series of fluorohydroxyapatite solid solutions, $Ca_5(OH)_xF_{1-x}(PO_4)_3$, exhibit decreased slopes for lower hydroxyl levels (smaller x), and requires consideration of the different lengths of spin "clusters" in order to model the behavior. The defect densities of apatites (clusters) are estimated by using 1-D cluster model.

We have also studied the ¹⁹F multiple-quantum NMR of a single crystal of mineral fluorapatite at different orientations with respect to the external magnetic field. The observed oscillatory behavior of the multiple-quantum dynamics is

interpreted in terms of 1-D clusters of fluoride ions in the defect-containing sample.

To my mother, wife, and son

ACKNOWLEDGMENTS

I would like to sincerely thank Dr. James P. Yesinowski for his continuous guidance and enthusiastic encouragement throughout my research. I would also like to thank Dr. Dye, Dr. Cukier, and Dr. Schwendeman for helpful discussions.

My special thanks go to Liam B. Moran for helpful discussions of my research. I would like to thank Mr. Kermit Johnson for helpful discussions of new NMR techniques and aid with computers. Thanks are also extended to the members of the NMR facility and the members of machine shop, in particular to Dr. L. Le, Mr. D. Jablonski, and R. Geyer. I would also like to acknowledge GTE Electrical Products Corporation for partial financial support of this work. I would also liked to thanks Dr. Chung-Nin Chau of GTE Electrical Products Corp. for preparing the fluorapatite samples and Dr. B. Fowler of National Institute of Standards and National Institute of Dental Research for lending us the samples of monoclinic hydroxyapatite and single-crystal fluorapatite.

I would like to thank my Korean friends at Michigan State University who encouraged me when I was discouraged.

Finally, my special thanks are reserved for my family: my wife, Sukhee, my son, Nammyoung, and my mother, who have prayed and waited patiently for my success.

TABLE OF CONTENTS

LIST OF TABLES	X
LIST OF FIGURES	χi
I. INTRODUCTION TO APATITE STRUCTURE AND CHEMISTRY	1
References	6
II. PART 1	
¹⁹ F MAS-NMR Investigation of Alkaline Earth Fluorapatites:	
Measurement of Chemical Shielding Tensors and Characteria	Z-
ation of Sites in Ca/Sr Fluorapatite Solid Solutions	
1. Introduction	9
2. Nuclear Spin Interactions in Solids	11
A. Zeeman Interaction	11
B. Radiofrequency Interaction	12
C. Chemical Shielding Interaction	12
D. Dipolar Interaction	14
3. Magic Angle Spinning (MAS)	۱7
4. Methods for Measuring the Chemical Shift Anisotropy	
from MAS-NMR Spectra	20
A. Moments Method	20
B. Herzfeld and Berger Graphical Method	21
5. Experimental	22
A. MAS-NMR Studies	22
B. Simulation of ¹⁹ F MAS-NMR Spectra of Fluorapatite Samples	24
6. Results	25

	A. Alkaline Earth Fluorapatites	25
	B. Solid Solutions of Ca/Sr Fluorapatite	34
7.	Discussion	42
	A. Measurement of the ¹⁹ F Chemical Shift Anisotropies of M ₅ F(PO ₄	ь)з
	Using Different Methods	42
	B. Separation of Metal-Fluoride Sigma- and Pi-Bonding Contribution	ıs
	to the ¹⁹ F Shielding Tensor	44
	C. Study of Site-Preference of Sr ²⁺ in Ca/Sr Fluorapatite Solid	
	Solutions Using ¹⁹ F MAS-NMR	53
8.	Conclusions	63
9.	References	65
II. PA	RT 2	
¹ H	l and ¹⁹ F Multiple-Quantum NMR Dynamics of Quasi-One	9-
Di	manalanal Onla Blatelle ettana la Anatitaa	
1.	mensional Spin Distributions in Apatites	
• •	. Introduction	69
	·	
	Introduction	
	Introduction	75
	Multiple-Quantum NMR Dynamics	75
	Introduction	75 75
	Introduction Multiple-Quantum NMR Dynamics A. Density Operator Description of Multiple-Quantum NMR Dynamics B. Time Development of the Density Operator in the Rotating	75 75 79
	Introduction Multiple-Quantum NMR Dynamics A. Density Operator Description of Multiple-Quantum NMR Dynamics B. Time Development of the Density Operator in the Rotating Frame	75 75 79 81
	Introduction Multiple-Quantum NMR Dynamics A. Density Operator Description of Multiple-Quantum NMR Dynamics B. Time Development of the Density Operator in the Rotating Frame C. Pulse Sequence for Multiple-Quantum NMR.	75 75 79 81 91
	Introduction Multiple-Quantum NMR Dynamics A. Density Operator Description of Multiple-Quantum NMR Dynamics B. Time Development of the Density Operator in the Rotating Frame C. Pulse Sequence for Multiple-Quantum NMR. D. Statistical Model of MQ Coherence Intensities	75 79 81 91

3.	Experimental
	A. Multiple-Quantum NMR Studies
	B. Sample Preparation and Characterization
4.	Results
	A. ¹ H Multiple-Quantum NMR Study of Resonance-Offset Effects 114
	B. ¹ H Multiple-Quantum NMR of Hydroxyapatite and Fluorapatite
	Samples
	C. ¹⁹ F Multiple-Quantum NMR of a Single Crystal of Fluorapatite . 131
5.	Discussion
	A. Effect of Resonance Offsets in PI-MQ NMR Pulse Sequence
	on the Formation of Multiple-Quantum Coherence
	B. Dimensionality Effects in the Multiple-Quantum NMR of
	hydroxyapatite
	C. One-Dimensional Cluster Model
	D. Estimation of Defect Densities Using the 1-D Cluster Model 139
	E. ¹⁹ F Multiple-Quantum NMR Dynamics of Single Crystal
	Fluorapatite
6.	Conclusions
7	References 154

Appendix A. Phase-incremented multiple-quantum pulse
sequence program for solids (Varian VXR
400 spectrometer)
Appendix B. Selection rule of the 1-spin/2-quantum average
Hamiltonian
Appendix C. C program for calculation of the ratio of 4Q/2Q
intensities for 1-D chain with different defect
densities

LIST OF TABLES

Table 1.	¹⁹ F NMR chemical shift anisotropies and asymmetry parameters of	
	$M_5F(PO_4)_3$ calculated using the moments method	26
Table 2.	The ¹⁹ F chemical shift anisotropy and asymmetry	
	parameter of M ₅ F(PO ₄) ₃ obtained using the Herzfeld and Berger	
	graphical method	32
Table 3.	¹⁹ F chemical shielding tensors of M ₅ F(PO ₄) ₃ , calculated from	
	the moments method using peak intensities obtained	
	from deconvolution	32
Table 4.	19 F NMR paramagnetic shielding parameters a_σ and a_π for	
	$M_5F(PO_4)_3$	51
Table 5.	Calculated probabilities of configurations A-D in Ca/Sr solid solution .	58
Table 6.	Calculated probabilities of configurations I-III in Ca/Sr solid solution.	58

LIST OF FIGURES

Figure 1. Structure of hydroxyapatite
Figure I-1. Chemical shielding powder pattern
Figure I-2. Cartesian axis system and polar coordinates for the dipolar
coupling of two nuclei
Figure I-3. Orientation of magnetic field and spinning axis vectors for magic
angle spinning experiments
Figure I-4. SPARTAN pulse sequence for monitoring spectral spin diffusion 23
Figure I-5. Contour plots of Ca ₅ F(PO ₄) ₃ spinning at 6.12 kHz and 10.18 kHz
using the Herzfeld and Berger graphic method
Figure I-6. Contour plots of Sr ₅ F(PO ₄) ₃ spinning at 6.26 kHz and 10.20 kHz
using the Herzfeld and Berger graphic method
Figure I-7. Contour plots of Ba ₅ F(PO ₄) ₃ spinning at 6.23 kHz and 10.18 kHz
using the Herzfeld and Berger graphic method
Figure I-8. The experimental and simulated spectra of $M_5F(PO_4)_3$ 35
Figure I-9. ¹⁹ F MAS-NMR center band HHLW vs spinning speed for
M ₅ F(PO ₄) ₃
Figure I-10 ¹⁹ F MAS-NMR of Ca _{8.97} Sr _{1.03} F ₂ (PO ₄) ₆ spinning at 8.23 kHz and
at 10.80 kHz
Figure I-11. Deconvolution spectrum of the 64 ppm peak in Fig. I-10b 39
Figure I-12. ¹⁹ F MAS-NMR spin diffusion experiment of Ca _{8.97} Sr _{1.03} F ₂ (PO ₄) ₆
using the SPARTAN pulse sequence and spinning at 10.87 kHz . 40
Figure I-13. ¹⁹ F MAS-NMR of Ca ₅ Sr ₅ F ₂ (PO ₄) ₆ spinning at 8.25 kHz and
at 10.3 kHz

Figure I-14.	. Comparison of the simulated and experimental ¹⁹ F MAS-NMR	
	stick spectra of $M_5F(PO_4)_3$ at the same spinning speed 45	5
Figure I-15.	. a_σ and a_π for M ₅ F(PO ₄) ₃ vs. ¹⁹ F isotropic chemical shift	
	with respect to free F ⁻ ion	2
Figure I-16	. Substitution of Sr ²⁺ in the three nearest neighbor Ca(2) sites of	
	Ca/Sr fluorapatite solid solutions	4
Figure I-17.	. Possible configurations for single and double Sr ²⁺ substitution	
	in the six next-nearest neighbor Ca(2) sites of Ca/Sr solid	
	solutions of fluorapatite	57
Figure I-18.	. Variation in the instantaneous chemical shifts during a rotor	
	cycle of 64 ppm and 79 ppm peaks of the solid solution	
	under the MAS condition at the different crystallite orientations 6	32
Figure II-1.	Schematic idealized arrangement of linear columns of protons	
	in calcium hydroxyapatite (Ca ₅ OH(PO ₄) ₃)	73
Figure II-2.	Random phases and correlated phases in an ensemble of	
	two level systems	77
Figure II-3.	General form of the pulse sequence of MQ NMR experiments 8	32
Figure II-4.	Pulse sequence for multiple-quantum NMR in solids 8	35
Figure II-5.	Time-domain MQ interferogram of hexamethylbenzene	
	using the TPPI	36
Figure II-6.	Frequency-domain ¹ H MQ spectrum of hexamethylbenzene	
		_

Figure II-7.	Time-domain MQ interferogram of hexamethylbenzene
	using the phase-incremented method
Figure II-8.	Frequency-domain ¹ H MQ spectrum of hexamethylbenzene
	using the phase-incremented method
Figure II-9.	Schematic energy level diagram for an N (odd) spin-1/2 system
	in a Zeeman field, and the degeneracy number of each state 93
Figure II-10	. Symbolic representation of the spreading of multiple spin corre-
	lations in a coupling network with increasing preparation time 94
Figure II-11	. Projection of Liouville space onto a two-dimensional plane 97
Figure II-12	. Pathways of the growth of MQ coherences in Liouville space
	for a 6-spin system under the 1-spin/2-quantum Hamiltonian 98
Figure II-13	. Evolution of n-quantum coherences predicted by the hopping
	model in 6 and 20 spin systems
Figure II-14	. Development of effective size with increasing preparation times
	for a 20 spin system predicted by the hopping model 103
Figure II-15	. Diagram representing the average M spin operator and its
	constituent operators of M = 4 in a 9 spin system
Figure II-16	. Schematic diagram of the growth of MQ coherence of different
	dimensionalities
Figure II-17	. Values of effective size N predicted by the incremental shell
	model for spin-1/2 nuclei evenly spaced on a line (1-D), square
	(2-D), and cubic (3-D) lattice

Figure II-18.	¹ H PI-MQ-NMR spectra of hexamethylbenzene with different	
	transmitter carrier frequencies	115
Figure II-19.	¹ H 1-dimensional spectra of apatite samples	116
Figure II-20.	¹ H MQ NMR spectrum of HAP-M using a preparation time	
	of 864 μs	18
Figure II-21.	Intensities of the ¹ H PI NMR MQ order of HAP-M for various	
	resonance offsets using a preparation time of 864 μ s	119
Figure II-22.	Intensities of the 1H PI NMR MQ order of HAP-M for various	
	resonance offsets using a preparation time of 1872 μ s	120
Figure II-23.	The normalized intensities of even-order MQ coherences of	
	apatite samples as a function of preparation time	122
Figure II-24.	Effective size N vs. MQ preparation time for HAP-M	125
Figure II-25.	$\ln(N)$ vs. $\ln(\tau/\tau_c)$ for all of the samples of hydroxyapatite and	
	fluorohydroxyapatite	126
Figure II-26.	Decay of absolute MQ coherences of apatites	128
Figure II-27.	The normalized intensities of 0Q and 2Q coherences of	
	a single crystal mineral sample of FAP with preparation times	
	at two orientations	129
Figure II-28.	In(absolute intensity of MQ orders) vs. preparation time of	
	single crystal fluorapatite at two different orientation	130
Figure II-29.	The effective magnetic field in the rotating frame in the presence	Э
	of an applied of field	132

Figure II-30.	Arrangement of hydroxyl groups separated by vacancies and/or	•
	fluoride ion substitutions in apatite samples	.138
Figure II-31.	Run number distributions for various defect densities in a one-	
	dimensional chain	.141
Figure II-32.	1-D cluster model of MQ growth for various defect densities in	
	apatite, compared to experimental data	142
Figure II-33.	Comparison between experimental 4Q/2Q intensities and	
	calculated 4Q/2Q intensities for FOHAP samples after	
	excluding two hydroxyl groups adjacent to fluorine ions	.143
Figure II-34.	Simulated MQ dynamics of 2, 3, 4, and 5 spin systems under	
	\mathcal{H}_{yx} for an oriented linear chain using ANTIOPE	.145
Figure II-35.	Mole fraction of spins in various run numbers and sum of the	
	mole fraction with different defect densities using percolation	
	theory	150
Figure II-36.	Comparison between experimental 2Q intensities of single crys	tal
	FAP and calculated 2Q intensities of two assumed defect dens	ities
	at two different orientations	151

I. INTRODUCTION TO APATITE STRUCTURE AND CHEMISTRY

Although the chemical reactions leading to mineral formation in biological systems are not fully understood, it is believed that a nonstoichiometric "defect" form of calcium hydroxyapatite, Ca₅(OH)(PO₄)₃, is the primary mineral phase of bone, dentin and dental enamel.¹⁻³ Apatites are also important in the production of fertilizer, in the lighting industry as a phosphor in fluorescent lamps, and in chromatography.⁴ At the pH values typically found in biological systems, the stability of calcium phosphates increases and the solubility decreases as the molar Ca/P ratio increases. Thus, in vivo dicalcium phosphate dihydrate CaHPO_{4·2}H₂O (DCPD, Ca/P=1.00) hydrolyzes into octacalcium phosphate Ca₈H₂(PO₄)_{6·5}H₂O (OCP, Ca/P=1.33), which hydrolyzes into hydroxyapatite (HAP) (Ca/P=1.67).⁵ Although amorphous calcium phosphate (ACP) is not found in bone and teeth, it can occur *in vivo* and is transformed into crystalline apatite via an octacalcium phosphate-like phase.⁶

The substitution of numerous impurities in the apatite lattice changes the properties of apatites. For example, the fluoride ion is effective in prevents the dental caries, since it increases the rate of remineralization and lessens the acid demineralization.^{7,8} The surface of HAP reacts with fluoride ions to yield calcium difluoride (CaF₂), fluorohydroxyapatite (Ca₅(OH)_{1-x}F_x(PO₄)₃), and fluorapatite (Ca₅F(PO₄)₃), depending upon conditions. Although the fluoridation of hydroxyapatite is not completely understood, several mechanisms have been suggested, including the ionic exchange of F⁻ for OH⁻ in the apatite structure,⁹ direct precipitation of fluorapatite mineral, and dissolution of hydroxyapatite and recrystallization of fluorapatite in the presence of F⁻.¹⁰ Carbonate ions can also replace hydroxyl groups or phosphate groups in the apatite lattice. A carbonate ion

can substitute for two hydroxyl groups in hydroxyapatite, forming type A carbonate apatite. This reaction takes place at high temperature, ¹¹ and results in an increase of the a axis length. ¹² The substitution of phosphate groups by carbonate ions decreases the a axis and increases the c axis. ^{13,14} The product is referred to as type B carbonate apatite. ¹¹ Calcium ions in apatites can be replaced by strontium ions. The presence of strontium ions in bone and teeth increases susceptibility to caries. The incorporation of strontium ions increases the a axis and c axis length. ¹⁵

From X-ray crystallographic analysis, hydroxyapatites have either a hexagonal crystal system with the space group P63/m or, for very stoichiometric samples, a monoclinic system with the space group P2₁/b. In the hexagonal crystal system, there are two $Ca_5(OH)(PO_4)_3$ groups in a unit cell of dimensions a (=b) = 942 pm and c = 688 pm.⁵ The structure of hexagonal hydroxyapatite is shown in Figure 1 projected down the c axis. There are two types of calcium ions in the structure, Ca(1) and Ca(2). Hydroxyl groups are surrounded by three Ca(2) ions in an equilateral triangle. Infinite linear chains of protons have a uniform spacing of 344 pm. The position of the hydroxyl protons is located about 130 pm from the plane of the triangle of Ca(2) ions. The central column of hydroxyl groups has six hexagonally-situated neighboring columns at distances of 942 pm. Statistical disorder of the hydroxyl groups result, on average, in protons in three of these six columns being located about 130 pm below the Ca(2) triangle, and about 130 pm above the Ca(2) triangle in the other three columns. When viewed down the (hexagonal) c axis, the Ca(2) ions form two displaced equilateral triangles of Ca(2) ions which are rotated by 60°. The distance between the two triangles is 344 pm. Columns of Ca(1) ions are parallel to the c axis. Each Ca(1) column

is located at the middle of a large equilateral triangle of three hydroxyl groups. The unit cell dimensions of monoclinic apatite are a=942 pm, b=2a, c=688 pm, and $\gamma=120^{\circ}.^{16,17}$ The space group of monoclinic hydroxyapatite, $P2_1/b$, indicates that the monoclinic form is regarded as twins occurring at 120° rotations about the c axis. 16,17 In the monoclinic crystal form, the protons in four of the six neighboring columns are located about 130 pm below the plane of the three Ca(2) ions, and those in the other two columns are located about 130 pm above the plane of the three Ca(2) ions. Fluorapatite, which has a structure similar to that of hydroxyapatite, has the same unit cell dimensions except that a=937 pm. Fluoride ions are exactly in the middle of the plane of the three Ca(2) ions, which forms a mirror plane. 18

Apatites have been investigated using various methods such as X-ray crystallography, IR, Raman, NMR, etc. The chemical environment of fluorine ions in alkaline earth fluorapatites and the preference of Sr²⁺ ions for Ca(2) sites of Sr/Ca fluorapatite solids solutions are studied using ¹⁹F MAS-NMR. The high level of defects found in naturally-occurring apatites is of interest in its own right, since they presumably reflect the conditions of formation of the mineral. Fluoride ions of fluorapatite are interrupted by charge-coupled vacancies, or substitution of fluoride ions by carbonate groups, hydroxyl groups, or chlorine ions. Hydroxyl chains in hydroxyapatite also have vacancies, or hydroxyl group substitutions by carbonate groups, fluorine ions, or chloride ions. Vacancies of hydroxyl groups in hydroxyapatite have been quantitatively determined by using IR and ¹H MAS-NMR.²⁰ However, these methods cannot reveal the presence of microscopic heterogeneity of various types of anions. The ¹H and ¹⁹F multiple-quantum NMR experiments in this thesis provide for the defect in the hydroxyl or fluorine chains and make

it possible to calculate the defect densities of apatites. Furthermore, the quasione-dimensional spin distributions in apatites represent a valuable model system in which to study the effects of dimensionality upon multiple-quantum NMR dynamics.

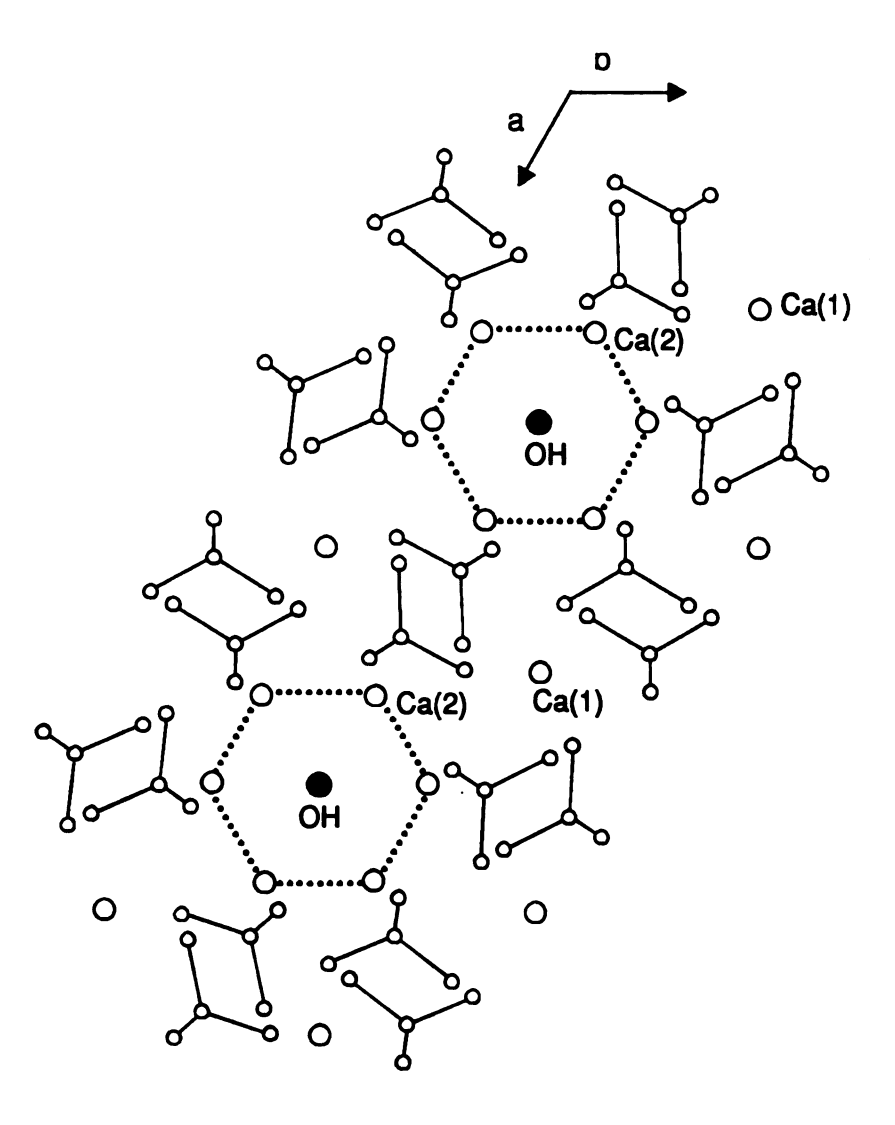


Figure 1. Structure of hydroxyapatite. Calcium ions (large open circle), hydroxyl groups (dotted circle), and phosphorus group (small open circles connected by a line). See text. Taken from Ref. 5.

References

- 1. W. E. Brown, Clin. Orthop. 44, 205 (1966).
- 2. D. G. A. Nelson, J. D. B. Featherstone, *Calcif Tissue Int.* **34**, (Suppl.2) S69 (1982).
- 3. R. Z. LeGeros and J. P. LeGeros, in "Phosphate Minerals" (J. O. Niragu and P. B. Moore, Eds), pp. 351-385, Springer-Verlag, Berlin, 1984.
- 4. S. J. Joris and C. H. Amberg, J. Phys. Chem. 75, 3167 (1971)
- 5. W. E. Brown, M. Mathew, and M. S. Tung, *Prog. Cryst. Growth Charact.* 4, 59 (1981).
- 6. J. L. Meyer and C. C. Weatherall, J. Colloid Sci, 89, 257 (1982).
- 7. L. M. Silverstone, Caries Res. 11, 59 (1977).
- 8. D. J. White, Caries Res. 22, 27 (1988).
- 9. S. A. Leach, Brit. Dent. J. 106, 133 (1959)
- 10. M. A. Spinelli, G. Brudevold, and E. C. Moreno, *Arch. Oral Biol.* 16, 187 (1971).
- 11. G. Bonel and G. Montel, C.R. Acad. Sci. [D] (Paris) 258, 923 (1964).
- 12. J. C. Elliott, "The crystallographic structure of dental enamel and related apatites", Ph.D. Thesis, University of London, 1964.
- 13. R. Z. LeGeros, *Nature*, **206**, 403 (1965).
- R. Z. LeGeros, J.P. LeGeros, O.R. Trautz, and E. Klein, *J. Dent. Res.* 43, 751 (1964).
- 15. H. J. M. Heijigers, F. C. M. Driessen, and R. M. H. Verbeeck, Calcif Tissue Int. 29, 127 (1979).
- 16. J. C. Elliott, Nature Phys. Sci., 230, 72 (1971).
- 17. J. C. Elliot, P. E. Mackie, and R. A. Young, Science, 180, 1055 (1973).

- 18. K. Sudarsanan, P. E. Mackie and R. A. Young, *Mater. Res. Bull.*, **7**, 1331 (1972).
- 19. E. C. Moreno, M. Kresak, and R. T. Zaradnik, Caries Res. Suppl. 1 142 (1977)
- 20. J. Arends, J. Christofferson, M. R. Christofferson, H. Eckert, B. O. Fowler,
 - J. C. Heughebaert, G. H. Nancollas, J. P. Yesinowski and S. J. Zawacki,
 - J. Cryst. Growth, 84, 515 (1987).

PART 1

¹⁹F MAS-NMR Investigation of Alkaline Earth Fluorapatites: Measurement of Chemical Shielding Tensors and Characterization of Sites in Ca/Sr Fluorapatite Solid Solutions

1. Introduction

The chemical shielding tensors of ¹⁹F in metal fluoride salts have been of widespread experimental and theoretical interest.¹⁻⁵ Line narrowing techniques such as multipulse "dipolar decoupling," magic-angle spinning (MAS),^{6,7} or the combination of these two techniques (CRAMPS)⁸ have been employed to obtain more accurate values for the isotropic chemical shift. However, knowledge of the three components of an anisotropic chemical shielding tensor can provide a more detailed understanding of the factors governing the chemical shielding, if the structural environment of the fluorine atom is known. Although single-crystal NMR studies are generally required to orient an arbitrary chemical shielding tensor in the crystallographic axis system, if the shielding tensor is axially-symmetric, one of its principal axes must necessarily be along the corresponding symmetry axis of the crystal.

The fluoride ion in the alkaline earth fluorapatites (M₅F(PO₄)₃, M = Ca, Sr, Ba) resides on a crystallographic hexagonal screw axis,⁹⁻¹¹ and therefore possesses such an axially symmetric ¹⁹F chemical shielding tensor. The ¹⁹F chemical shift anisotropy (CSA) for calcium fluorapatite has been determined from single-crystal NMR measurements,^{12,13} and an accurate isotropic chemical shift has been obtained from ¹⁹F MAS-NMR studies (because of the special arrangement of the fluoride ions in a linear chain, sharp spectra are obtained at modest spinning speeds without using multiple-pulse techniques, as discussed in references 6 and 7). However, corresponding data for the strontium and barium analogues have not been reported. We have therefore measured the ¹⁹F chemical shielding tensors of these compounds, using three different methods that yield the CSA from the spinning sideband patterns (spectral moments.¹⁴ Herzfeld-Berger graphical

analysis, 15 and spectral simulation), and will discuss briefly the relative merits of these methods.

Knowing both the chemical shielding tensor components and the absolute chemical shielding scale relative to the free fluoride ion enables one to separate contributions to the shielding from the sigma- and the pi-bonding between metal and fluoride ion for the three different metals investigated. This approach enables us to predict chemical shielding tensors in other systems, such as solid solutions of calcium/strontium fluorapatite.

The broad linewidth typical of powder samples arising from dipolar interactions and CSA obscures identification of individual peaks having different chemical environments in many solids of interest. Since MAS-NMR averages out these anisotropies, and results in sharp peaks at each isotropic chemical shift, it is extremely useful for the structural study of solids having many components. For example, the site preference of solid solutions of a semiconductor alloy was studied by using ³¹P MAS-NMR and peak deconvolution. ¹⁶ and ¹⁹F MAS-NMR has been also used to quantitatively studying fluoride ions perturbed by antimony ions in antimony-doped fluorapatites.²⁰ Since the chemical shift of fluorine is very sensitive to its chemical bonding environment, we have used high speed ¹⁹F MAS-NMR for the study of solid solutions of calcium/strontium fluorapatite. The ¹⁹F NMR parameters measured for the pure alkaline earth fluorapatites $(M_5F(PO_4)_3, M = Ca, Sr, Ba)$ are used in the interpretation of the data from the solid solutions. Since the ¹⁹F chemical shift difference between strontium and calcium fluorapatites is 33.2 ppm, the isotropic chemical shifts of samples having different ratios of calcium to strontium can be distinguished by using high field/high speed ¹⁹F MAS-NMR. The integrated intensity of the non-overlapped peaks and the deconvolution of asymmetric broad peaks arising from the perturbation by strontium substitution yield the ratios of each component. The results were used to study the site preference of Sr²⁺ ion substitution in a solid solution having the composition Ca_{8.97}Sr_{1.03}F₂(PO₄)₆.

2. Nuclear Spin Interactions in Solids

A typical nuclear spin Hamiltonian of a diamagnetic solid is given by

$$\mathcal{H} = \mathcal{H}_z + \mathcal{H}_{rf}(t) + \mathcal{H}_{CS} + \mathcal{H}_D + \mathcal{H}_O + \mathcal{H}_J$$
 (I-1)

where the various Hamiltonians on the right represent respectively the Zeeman, radiofrequency, chemical shift, dipolar, quadrupolar, and scalar interactions of the nuclei. The first two terms are determined by external static magnetic and applied rf fields. Thus, they describe "external" interactions of the spins. The other terms depend on the fundamental characteristics of the nucleus and its environment. In the solids that we have studied, the quadrupolar and scalar interaction are not relevant, and will not be discussed.

A. Zeeman Interaction

The interaction between a nuclear magnetic moment, $\vec{\mu}$, and an applied static field, \vec{H}_0 is represented by the Zeeman Hamiltonian

$$\mathcal{H}_{z} = -\frac{1}{2\pi} \sum_{i} \vec{\mu}_{i} \cdot \vec{H}_{0} = -\sum_{i} \gamma_{i} \hbar \vec{I}_{i} \cdot \vec{H}_{0}$$
 (I-2)

where \hbar is Planck's constant divided by 2π , γ_i is the magnetogyric ratio of nucleus i, and $\vec{I_i}$ is the angular momentum spin operator for nucleus i. The eigenvalues of this term alone are

$$E_z/h = \sum_i \gamma_i \hbar m_i H_0 \tag{I-3}$$

where m; is the magnetic quantum number.

B. Radiofrequency Interaction

In NMR spectroscopy, transitions between energy levels are generally induced by an applied rf field, which is applied perpendicular to the static field direction. The Hamiltonian term for the radiofrequency (rf) field along the x direction is given by

$$\mathcal{H}_{rf}(t) = 2\pi \vec{\mu}_x \mathsf{H}_1 \cos(2\pi \nu \mathsf{t}) \tag{I-4}$$

where $\vec{\mu}_x$ is the nuclear magnetic moment in the x direction, H_1 is the magnitude of the rf field applied in the x direction, and ν is the Larmor frequency.

C. Chemical Shielding Interaction

The screening of the nuclei from the external magnetic field by the surrounding electrons slightly modifies the Zeeman interaction. The shielding generated at the nuclei from the external magnetic field results in the Hamiltonian

$$\mathcal{H}_{CS} = \gamma \hbar \vec{I} \cdot \hat{\sigma} \cdot \vec{H}_0 \tag{I-5}$$

where $\hat{\sigma}$ is the chemical shielding tensor, a dimensionless second rank tensor. In solutions, the chemical shielding interactions are averaged out by rapid isotropic tumbling. Thus, a single line in solution is observed at the isotropic average of the shielding tensor $(Tr\{\hat{\sigma}\})$. In solids, since molecular motions are typically slow or absent, a broad powder pattern is observed. The chemical shielding tensor $\hat{\sigma}$ is symmetric in larger static magnetic field. In the principal axis system (PAS), all off-diagonal elements of shielding tensor zero. The chemical shielding tensor can ne described by the three principal values σ_{11} , σ_{22} , and σ_{33} , and three angles which specify the orientation of the principal axis system. If \mathcal{H}_{CS} are the dominant interactions, the three components of the chemical shielding tensor can be "read-off" directly from the spectrum since a powder pattern is related the chemical shielding. The theoretical powder patterns for a shielding tensor with different

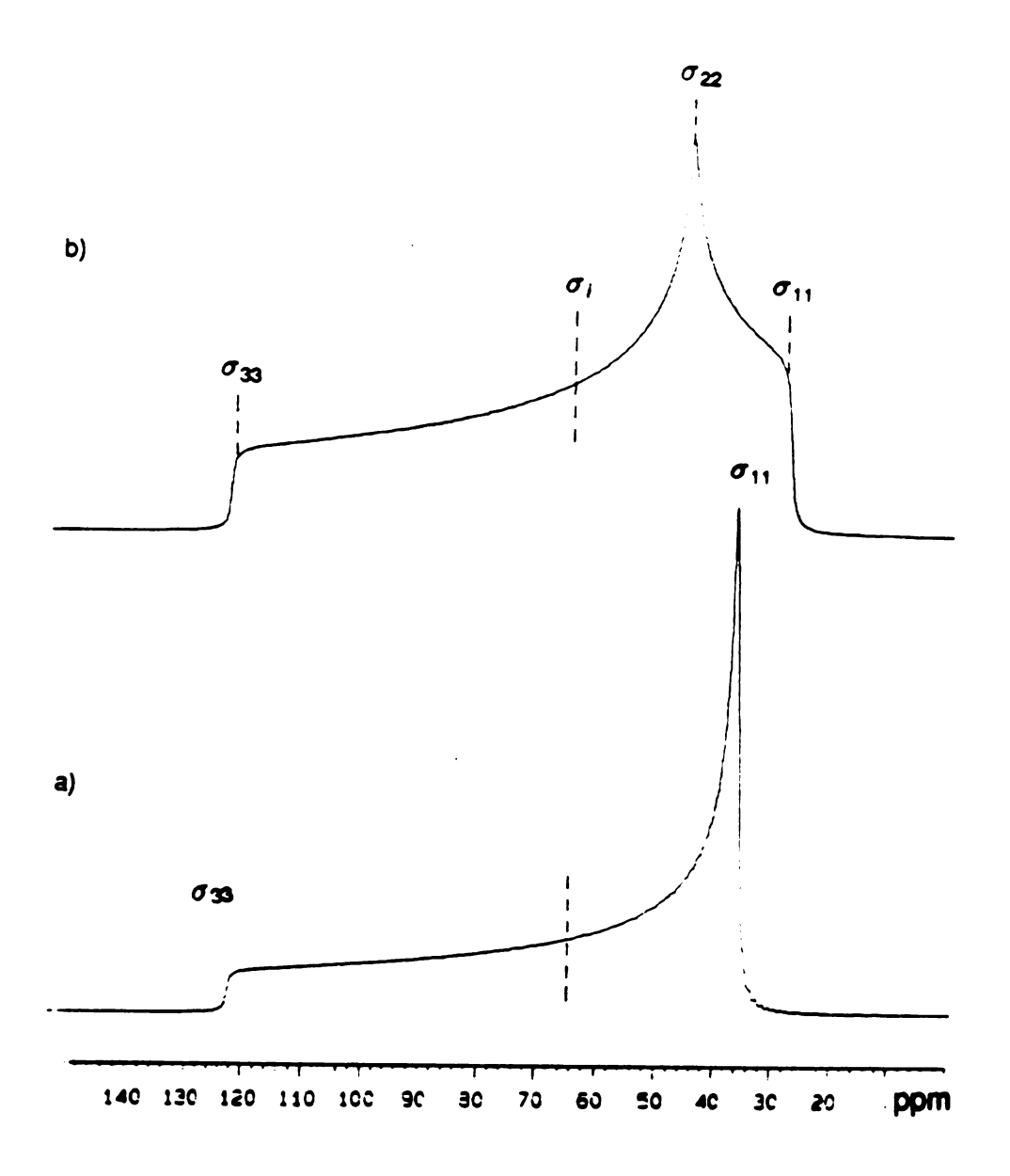


Figure I-1. Calculated chemical shielding powder patterns (σ_i = 64 ppm): (a) axially symmetric shielding tensor (CSA = 84 ppm and η = 0); (b) non-axially symmetric shielding tensor (CSA = 84 ppm and η = 0.3). The dashed line denotes the isotropic chemical shift. An exponential apodization function corresponding to a 500 Hz line broadening was applied to the calculated FID before Fourier transformation.

asymmetry parameters η are shown in Fig. I-1. The asymmetry parameter η is defined as

$$\eta = \frac{\sigma_{22} - \sigma_{11}}{\sigma_{33} - \sigma_{1}}.\tag{I-6}$$

Conventionally, the order of the principle values of the chemical shielding tensors is $\sigma_{11} \le \sigma_{22} \le \sigma_{33}$. The chemical shift anisotropy is defined as

$$CSA = \sigma_{33} - 1/2(\sigma_{11} + \sigma_{22}). \tag{I-7}$$

The chemical shielding tensor is generally obtained from single crystal NMR studies or as in the present work, from MAS-NMR spectra on polycrystalline samples.

D. Dipolar Interaction

The dipolar interaction is the consequence of direct magnetic coupling of nuclei through space. The dipolar Hamiltonian of two nuclear spins (spin 1 and spin 2) is represented by

$$\mathcal{H}_{D} = \left(\gamma_{i}^{2}/r_{12}^{3}\right)\hbar^{2} \vec{I}_{1} \cdot \hat{D}_{12} \cdot \vec{I}_{2} \tag{I-8}$$

where r_{12} is distance between the nuclei and \hat{D}_{12} is the dipolar coupling tensor.

In a Cartesian coordinate system x, y, z (see Fig. I-2),

$$\hat{D}_{12} = 1/r_{12}^{2} \begin{bmatrix} \left(r_{12}^{2} - 3x^{2} \right) & -3xy & -3xz \\ -3xy & \left(r_{12}^{2} - 3y^{2} \right) & -3yz \\ -3xz & -3yz & \left(r_{12}^{2} - 3z^{2} \right) \end{bmatrix}$$
 (I-9)

The trace of \hat{D}_{12} is zero, and it is axially symmetric: $D_{12} = D_{21}$, $D_{23} = D_{32}$, and $D_{13} = D_{31}$. In the principal axis system, with r_{12} along the z axis, all off-diagonal elements are zero. The dipolar tensor can then be rewritten as

$$\hat{D} = 1/r_{12}^{5} \begin{bmatrix} 1 & 0 & 0 \\ 0 & 1 & 0 \\ 0 & 0 & -2 \end{bmatrix}$$
 (I-10)

It is useful to transform from Cartesian coordinates to polar coordinates (Fig. I-2).

The Cartesian coordinates x, y, and z are represented by the following

$$x = r \sin \theta \cos \phi$$

$$y = r \sin \theta \sin \phi$$

$$z = r \cos \theta.$$
(I-11)

Eq. (I-8) can be rewritten in the polar coordinate system as

$$\mathcal{H}_{D} == \gamma/r_{12}^{3}\hbar \left(A + B + C + D + E + F \right) \tag{I-12}$$

$$A = \left(1 - 3\cos^{2}\theta \right) I_{1z} I_{2z}$$

$$B = -\frac{1}{4} \left(1 - 3\cos^{2}\theta \right) \left[I_{1}^{+} I_{2}^{-} + I_{1}^{-} I_{2}^{+} \right] = \frac{1}{2} \left(1 - 3\cos^{2}\theta \right) \left(I_{1z} I_{2z} - \vec{I}_{1} \cdot \vec{I}_{2} \right)$$

$$C = -\frac{3}{2} \sin\theta \cos\theta e^{-i\phi} \left[I_{1z} I_{2}^{+} + I_{1}^{+} I_{2z} \right] \tag{I-13}$$

$$D = -\frac{3}{2} \sin\theta \cos\theta e^{+i\phi} \left[I_{1z} I_{2}^{-} + I_{1}^{-} I_{2z} \right]$$

$$E = -\frac{3}{4} \sin^{2}\theta e^{-2i\phi} I_{1}^{+} I_{2}^{+}$$

$$F = -\frac{3}{4}\sin^2\theta e^{+2i\phi}I_{\perp}^{-}I_{2}^{-}$$

where I^+ and I^- are the ladder operators, $I^+ = \vec{I}_x + i\vec{I}_y$ and $I^- = \vec{I}_x - i\vec{I}_y$. $I^+|\alpha\rangle = 0$, $I^+|\beta\rangle = |\alpha\rangle$, $I^-|\alpha\rangle = |\beta\rangle$, and $I^-|\beta\rangle = 0$. The various ladder operators can change the nuclear spin quantum numbers m_1 and m_2 in a characteristic way. Term 'A' does not shift the nuclear spin quantum number; term 'B' alters both spins by \pm 1, but $I_1^+I_2^-$ and $I_1^-I_2^+$ do not change the sum $(m_1 + m_2)$; the others change $(m_1 + m_2)$ by \pm 1 or \pm 2. Since, at high magnetic fields, the perturbations due to the off-diagonal elements C, D, E, and F are negligible compared to the terms 'A' and 'B', Eq. (I-13) can be rewritten as the truncated homonuclear dipolar Hamiltonian in terms of the A and B terms

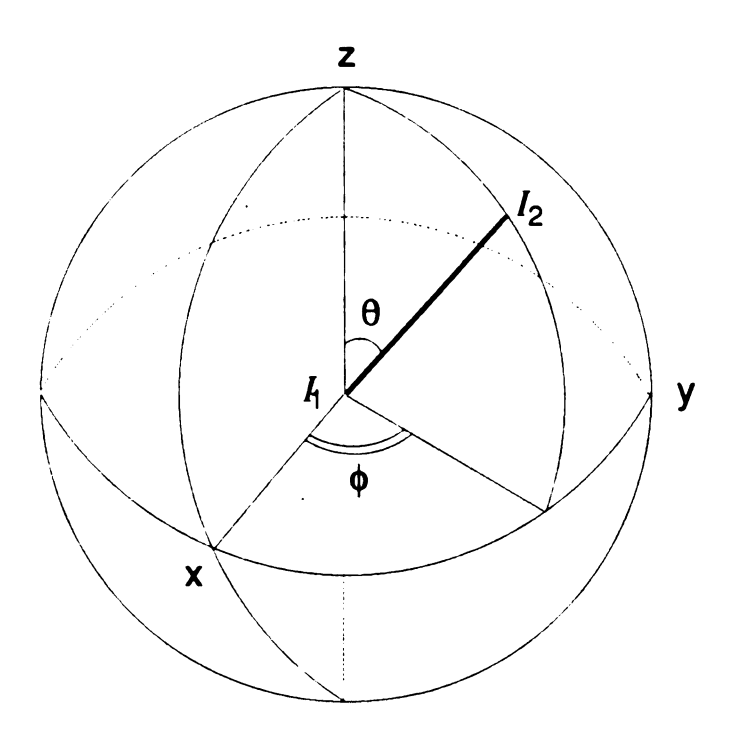


Figure I-2. Cartesian axis system and polar coordinates for the dipolar coupling of the two nuclei.

$$\mathcal{H}_{D} = (\gamma_{1}^{2}/2r_{12}^{3})\hbar \left(1 - 3\cos^{2}\theta\right) \left(\vec{I}_{1} \cdot \vec{I}_{2} - 3I_{1z}I_{2z}\right). \tag{I-14}$$

The truncated heteronuclear dipolar Hamiltonian remains only the term 'A' that is replaced I_1 and I_2 by I and S.

3. Magic Angle Spinning (MAS)

In solids, anisotropic interactions such as the chemical shielding interaction, dipolar couplings and electric quadrupole couplings can result in very broad NMR spectra. These anisotropies can be efficiently removed by spinning the sample about an axis making an angle of approximately 54.7° with respect to the external magnetic field $^{17-19}$ (Fig. I-3) (see below). The rotation of the sample about an angle β with respect to the external magnetic field makes the anisotropic terms of the Hamiltonian time-dependent with the periodicity of the sample rotation frequency $\omega_{\rm r}$. The three anisotropic terms mentioned above are generally small compared to a Zeeman term and are treated as perturbations. The Hamiltonian is divided into two parts

$$\mathcal{H} = \bar{\mathcal{H}} + \mathcal{H}'(t) \tag{I-15}$$

where $\bar{\mathcal{H}}$ is the time-average of the Hamiltonian and $\mathcal{H}'(t)$ is time-dependent. In this section, the effect of sample rotation on each of two anisotropic terms will be discussed in turn.

Since the chemical shielding tensor is of small size relative to the Zeeman term, it can be truncate it. We can rewrite Eq. (I-5) as

$$\mathcal{H}_{cs} = \gamma \hbar \sigma_{zz} \mathbf{H}_0 \tag{I-16}$$

where

$$\sigma_{zz} = \lambda_{11}^2 \sigma_{11} + \lambda_{22}^2 \sigma_{22} + \lambda_{33}^2 \sigma_{33}. \tag{I-17}$$

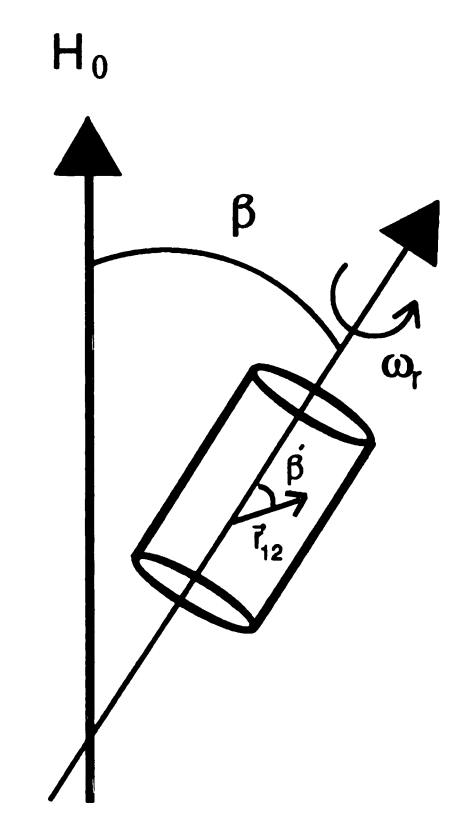


Figure I-3. Orientation of magnetic field H_0 and spinning axis vectors for magic angle spinning experiments.

In these equation, the terms $\sigma_{\alpha\alpha}$ (α = 1, 2, 3) are the principal values of the chemical shielding tensor and $\lambda_{\alpha\alpha}$ are the direction cosines of the principal axes with respect to the external magnetic field. The rotation of the sample makes the direction cosines time-dependent

$$\lambda_{p} = \cos \beta \cos \chi_{p} + \sin \beta \sin \chi_{p} \cos (\omega_{r} t + \psi_{p})$$
 (I-18)

where β is the angle between the rotation axis and the external magnetic field, χ_p is the angle between the rotation axis and the p-th principal axis of the chemical shielding tensor, and ψ_p is the azimuthal angle of the p-th principal axis at t=0. By substituting Eq. (I-18) into Eq. (I-17) and taking the time-average, we obtain the following equation

$$\sigma_{zz} = \frac{1}{2}\sin^2\beta Tr\{\hat{\sigma}\} + \frac{1}{2}(3\cos^2\beta - 1)\sum_{p}\sigma_{p}\cos\chi_{p}.$$
 (I-19)

Only the isotropic chemical shift σ_i (=1/3 $Tr\{\hat{\sigma}\}$) in Eq. (I-19) remains if β is 54.7° $[(3\cos^2\beta-1)=0]$, the so-called "magic angle".

Since the rotation of the solid sample makes $\cos\theta$ in the dipolar Hamiltonian time-dependent, we can rewrite $\cos\theta$ as

$$\cos \theta(t) = \cos \beta \cos \beta' + \sin \beta \sin \beta' \cos \left(\omega_{\tau} t + \phi'\right) \tag{I-20}$$

where β' is the angle between the axis of rotation and \vec{r}_{12} , and ϕ' is the azimuthal angle of \vec{r}_{12} at t=0. The time average of $\cos^2\theta(t)$ is

$$\overline{\cos^2 \theta} = \cos^2 \beta \cos^2 \beta' + \frac{1}{2} \sin^2 \beta \sin^2 \beta' = \frac{1}{6} (3 \cos^2 \beta - 1) \left(3 \cos^2 \beta' - 1 \right) + \frac{1}{3} \quad \text{(I-21)}$$

Substituting Eq. (I-21) into Eq. (I-14), we can write the average (time-independent) dipolar Hamiltonian as

$$\mathcal{H}_{D} = \frac{\gamma_{1}^{2}}{\pi^{3}}\hbar (3\cos^{2}\beta - 1) (3\cos^{2}\beta' - 1) (\vec{I}_{1} \cdot \vec{I}_{2} - 3I_{1z}I_{2z}). \tag{I-22}$$

The time-independent dipolar interaction is averaged out at the magic angle.

Under the MAS condition, the averaged time-independent Hamiltonian yields only isotropic chemical shifts, but time-dependent Hamiltonians are modulated by

the periodicity of the spinning speed of a sample. From Eq. (I-14) and (I-22), the time-dependent part of the dipolar interaction is given by

$$\mathcal{H}_{D}(t) = (3\gamma_{1}^{2}/2r^{3})\hbar \left(\vec{I}_{1} \cdot \vec{I}_{2} - 3I_{1}I_{2}\right) \left[\sin 2\beta \sin 2\beta' \cos (\omega_{r}t + \psi) + \sin^{2}\beta \sin^{2}\beta' \cos 2(\omega_{r}t + \psi)\right]$$
(I-23)

The time-dependent Hamiltonians of the other two interactions (chemical shift and quadrupolar interactions) also show the same periodicity in ω_{τ} and $2\omega_{\tau}$ as the time-dependent dipolar Hamiltonian. The modulations of ω_{τ} and $2\omega_{\tau}$ in the time-domain give rise to peaks in the frequency-domain, referred to as sidebands, which appear at integral multiples of the spinning speed from a centerband. The intensities of sidebands that are related to the CSA,^{14,15} and enable one to measure the chemical shielding tensors.

4. Methods for Measuring Chemical Shift Anisotropy (CSA) from MAS-NMR Spectra

In this study, three methods were used to calculate the principal components of the chemical shielding tensor: the moments method of Maricq and Waugh,¹⁴ a graphical procedure developed by Herzfeld and Berger that is based on spectral simulation,¹⁵ and a MAS-NMR spectral simulation program.

A. Moments Method

The *I*-th moment of an NMR spectrum¹⁴ is obtained using the following definition (integral) and approximation (summation):

$$M_{l} = \int_{-\infty}^{\infty} \omega^{l} \mathbf{g}(\omega) d\omega \simeq \omega_{r}^{l} \Sigma_{N} N^{l} \mathbf{g}(N\omega_{r})$$
 (I-24)

with ω the frequency of an isochromat (with respect to the isotropic chemical shift position), $g(\omega)$ the intensity of the area normalized to one at frequency ω , N the

order of the N-th sideband (positive or negative integer, 0 for the centerband), $g(N\omega_r)$ the normalized area (or peak height) of the N-th sideband at frequency $N\omega_r$; and ω_r the spinning frequency. For a reasonably "sharp" experimental MAS-NMR spectrum, the summation in Eq. I-24 yields moments very close to the true moments defined by the integral expression

The moments method yields the components of the chemical shielding tensor by relating them to the measured second and third moments of the MAS-NMR spectrum with the following equations:¹⁴

$$M_2 = (\delta^2/15)(3 + \eta^2) \tag{I-25}$$

$$M_3 = (2\delta^3/35)(1 - \eta^2)$$
 (I-26)

where M_2 and M_3 are the second and third moments respectively, and δ and the asymmetry parameter η (Eq. I-6) are related to the shielding tensor components. δ and an isotropic chemical shift are represented by the following equations:

$$\delta = \sigma_{33} - \sigma_i \tag{I-27}$$

$$\sigma_i = \frac{1}{3} (\sigma_{11} + \sigma_{22} + \sigma_{33}). \tag{I-28}$$

Using experimentally determined values of the second and third moments, and of the isotropic chemical shift (σ_i) , we can determine the individual components of the shielding tensor σ_{11} , σ_{22} , and σ_{33} . The chemical shift anisotropy (CSA) can be calculated from Eq. I-7.

B. Herzfeld and Berger Graphical Method

The Herzfeld and Berger graphical method was used to obtain the chemical shielding tensors by overlaying the various calculated contours corresponding to the measured ratios $l_{\pm i}/l_o$, where $l_{\pm i}$ is the intensity of the $\pm i$ -th sideband and l_o is the intensity of the centerband. The region of overlap provides both values

and error limits for the intermediate parameters μ and ρ , which are then used to calculate the chemical shift tensor from equations (I-29) and (I-30):¹⁵

$$\mu = (\gamma H_0) (\sigma_{33} - \sigma_{11}) / \omega_r$$
 (I-29)

$$\rho = (\sigma_{11} + \sigma_{33} - 2\sigma_{22}) / (\sigma_{33} - \sigma_{11}). \tag{I-30}$$

5. Experimental

A. MAS-NMR Studies

Alkaline earth fluorapatites were synthesized and provided by Dr. Chung-Nin Chau of GTE Chemicals, Towanda, PA. The ¹⁹F MAS-NMR spectra were recorded at 376MHz on a 9.4T Varian Associates VXR-400 spectrometer at the Max T. Rogers NMR Facility at Michigan State University. The fluorine radiofrequency was amplified by an AMT model 3137/3900-2 amplifier. A high speed 19 F MAS-NMR probe from Doty Scientific with 5 mm o.d. Si₃N₄ rotors with Vespel caps was used. The spinning speed was measured with a fiber optic detector, and was constant to within ±10 Hz during acquisitions. The magic angle was set by minimizing the linewidth of calcium fluorapatite, which also provided a secondary chemical shift reference (64.0 ppm with respect to hexafluorobenzene at 0.0 ppm). The $\pi/2$ pulse length was 4.0-4.2 μ s, and spectral widths of 100 - 120 kHz were used. An exponential apodization corresponding to a line-broadening of 37-80Hz was applied to the free-induction decay, which was the result of four scans with a relaxation delay greater than five times the spin-lattice relaxation time T₁. The T₁ values of centerbands were obtained by using an inversion-recovery sequence, and are 85, 87, 88, 101, and 112 second for Ca₅F(PO₄)₃, Sr₅F(PO₄)₃, $Ba_5F(PO_4)_3$, $Ca_{8.97}Sr_{1.03}F_2(PO_4)_6$, and $Ca_5Sr_5F_2(PO_4)_6$ respectively. The SPAR-

TAN pulse sequence, shown in Fig. I-4, was employed for ¹⁹F MAS-NMR spectral spin diffusion measurement.²⁰ The centerband and assorted sidebands were selectively inverted by a 180° DANTE pulse train²¹ consisting of twelve 15° (2 μ s) pulses given at the same point of each rotor cycle (rotor-gated synchronization).

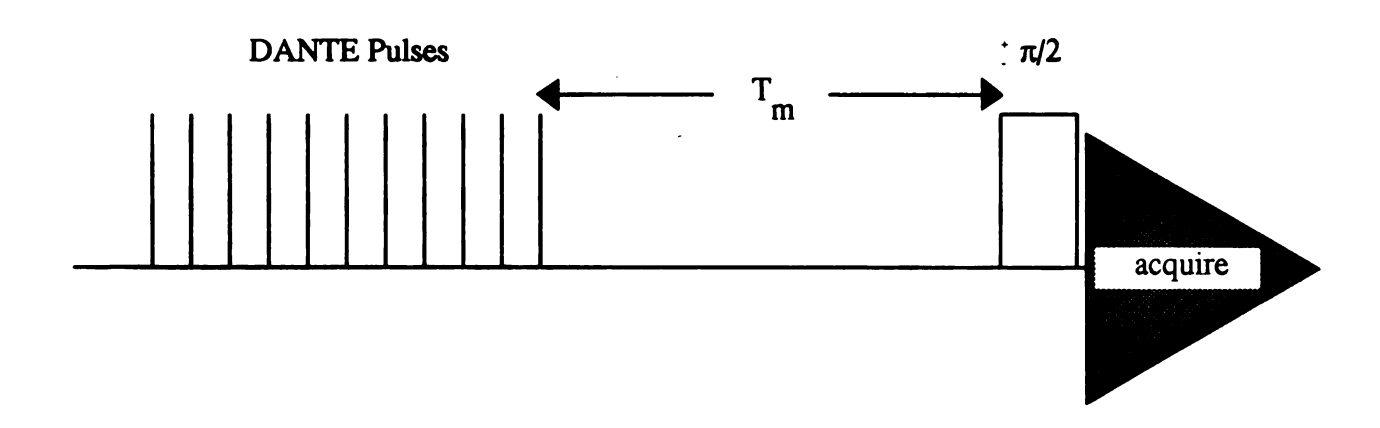


Figure I-4. SPARTAN pulse sequence for monitoring spectral spin diffusion.²⁰ (see text)

The power levels and pulse lengths of the pulses in the DANTE train were adjusted to make the excitation profile suitably selective. After the mixing period, a nonselective 90° read pulse (12 μ s) was given with alternated phases to cancel out imperfections in the DANTE pulse trains²² that resulted in incomplete inversion of the magnetization at a specific frequency.

The peak intensities used to calculate the moments at the different spinning speeds were obtained both from integration and from deconvolution of the individual peaks using VNMR 3.2 software, and the peak intensities from integration rather than peak heights were used for the Herzfeld and Berger analysis, since the half-height linewidths ($\Delta\nu_{1/2}$) of the centerband and sidebands can be somewhat different. All ¹⁹F NMR spectra were baseline-corrected prior to integration and deconvolution to remove a "dip" presumedly due to receiver overload. Since there are impurity peaks that overlap the peaks of strontium fluorapatite and barium fluorapatite in the ¹⁹F NMR spectra, the CSA values determined by using the deconvolution data are assumed to be more accurate than those obtained using integrated intensities. A Lorentzian shape was assumed for the deconvolutions, and the half-height linewidth and frequency of each peak was allowed to vary.

B. Simulation of ¹⁹F MAS Spectra of Fluorapatite Samples

Simulations of the ¹⁹F MAS-NMR spectra that take into account of the CSA but not dipolar couplings were performed by using the MAS-NMR simulation routine provided with the Varian VNMR 3.2 software. The input parameters are the chemical shift anisotropy, the asymmetry parameter, the isotropic chemical shift, the Lorentzian linewidth, and the spinning speed. The peak widths of the simulated spectra were chosen to agree with the experimental ones, and 8K complex points and 8K zero-filling were used. Alternatively, the PC-based

computer program ANTIOPE,²³ which takes account for dipolar couplings, was used to simulate the spectrum of five linear spins 3.44 Angstroms apart, with a CSA tensor corresponding to that of $Ca_5F(PO_4)_3$. The ANTIOPE simulation was performed by observing magnetization of the middle spin (+3) of a 5 spin system, since the homonuclear dipolar coupling pattern between the middle spin and its neighbors better reflects the couplings of the infinite linear spin chains in $Ca_5F(PO_4)_3$. The 256 complex data points calculated were zero-filled to 8K to avoid errors from inadequate digital resolution and apodized with a linebroadening of 200Hz.

6. Results

A. Alkaline Earth Fluorapatites

Table 1 shows the measured ¹⁹F MAS-NMR spectral moments of $Ca_5F(PO_4)_3$, $Sr_5F(PO_4)_3$ and $Ba_5F(PO_4)_3$, and the calculated CSA and η values at different spinning speeds obtained from the moments method. The existence of imaginary values of η , obviously lacking any physical significance, arises from experimental errors in the moments measurements. From equations (I-7), (I-27), and (I-28), we can rewrite the CSA in the following form;

$$CSA = \frac{3}{2}(\sigma_{33} - \sigma_i) = \frac{3}{2}\delta.$$
 (I-31)

Therefore, we can calculate the value of a CSA without knowing the value of η .

Theoretically, the second and third moments are independent of the spinning speed.¹⁴ The changes in the second and third moments with spinning speed seen in Table 1 are the result of experimental error; therefore, we use the average value of the moments over all the spinning speeds to calculate an average CSA and η .

Table 1. 19 F NMR chemical shift anisotropy and asymmetry parameter η of $M_5F(PO_4)_3$ (M = Ca, Sr, and Ba) calculated using the moments method, from both integration and deconvolution. The numbers in parentheses are obtained from the integration data.

	ν _τ (kHz)	M ₁ (ppm)	M ₂ ((ppm) ²)	M ₃ ((ppm) ³)	Measured η	Measured CSA (ppm)
	4.12	-0.25 (0.20)	660 (664)	10690 (11740)	0.092 (0.219i)	86.0 (87.1)
	5.12	-0.09 (0.14)	662 (663)	11340 (11950)	0.167i (0.248i)	86.7 (87.3)
	6.12	-0.13 (0.20)	651 (653)	10980 (11830)	0.150 (0.266i)	85.9 (86.8)
£() 3	7.12	-0.08 (-0.12)	646 (649)	10610 (10480)	0.095i (0.073)	85.4 (85.4)
Ca ₅ F(PO4) ₃	8.12	-0.03 (-0.06)	636 (638)	10310 (10470)	0.068i (0.110)	84.6 (84.9)
Ö	9.12	-0.01 (0.18)	638 (634)	10420 (10800)	0.089i (0.195i)	84.8 (85.0)
	10.18	0.01 (0.10)	643 (643)	10440 (10290)	0.008i (0.062)	85.1 (84.9)
	average	-0.08± 0.08 (0.090± 0.08)	648 ±12 (649± 11)	10680 ±340 (11080 ±660)	0.095i (0.179i)	85.5 ±0.7 (85.6 ±1.0)
	4.29	-0.48 (0.05)	1059 (1069)	20690 (22530)	0.204 (0.08i)	108.4 (109.8)
	5.63	-0.21 (-0.45)	921 (917)	17700 (17090)	0.077 (0.158)	101.7 (101.2)

	6.26	-0.37 (-0.83)	1054 (1036)	20630 (19460)	0.194 (0.243)	108.2 (106.9)
204)3	7.00	-0.30 (0.52)	1077 (1095)	23980 (24340)	0.201i (0.184i)	110.8 (111.6)
	8.20	-0.38 (-0.54)	1036 (1025)	19940 (18770)	0.207 (0.268)	107.2 (106.1)
Sr ₅ F(PO ₄₎₃	10.20	0.11 (0.16)	1033 (1047)	21180 (22110)	0.026 (0.121i)	107.8 (108.2)
	average	-0.26 ±0.21 (-0.18 ±0.46)	1030 ±51 (1032 ±56)	20690 ±1820 (20720 ±2480)	0.117 (0.119)	107.4 ±2.8 (107.5 ±3.3)
	6.23	0.10 (0.74)	2314 (2304)	69840 (73820)	0.110 (0.170i)	161.8 (161.0)
(PO ₄) ₃	6. <i>2</i> 3 8.19					
Ba ₅ F(PO ₄) ₃		0.74)	(2304) 2209	(73820) 58000	(0.170i) 0.267	(161.0) 157.2
Ba ₅ F(PO ₄) ₃	8.19	(0.74) 0.02 (-0.53) 0.03	(2304) 2209 (2248) 2227	(73820) 58000 (61030) 63410	(0.170i) 0.267 (0.295) 0.190	(161.0) 157.2 (155.4) 157.3

The values for the CSA and moments in parentheses in Table1 are those determined from integration data, and the standard deviations are larger than those obtained from the deconvolution data.

The CSA values can be also obtained by using the graphical procedure of Herzfeld-Berger, which involves measurement of the sideband intensities. Fig. I-5 shows the two graphical plots of Herzfeld-Berger for $Ca_5F(PO_4)_3$ spinning at 6.12 and 10.18 kHz. The measured intensity ratios I_{\pm}/I_0 of $Ca_5F(PO_4)_3$ spinning at 6.12 kHz do not overlap at any region of the plot. At the higher spinning speed of 10.18kHz, a region of overlap is observed, centered around $\rho=0.95\pm0.05$ and $\mu=3.19\pm0.19$. Other plots using the Herzfeld and Berger graphical method for $Sr_5F(PO_4)_3$ spinning at 6.26 and 10.20 kHz are shown in Fig. I-6. From Fig. I-6a, only four lines out of the ten lines overlap around $\rho=0.46\pm0.05$ and $\mu=6.4\pm0.20$, and the CSA and η value (92 ± 4 and 0.47 ± 5) are quite different from those obtained at a 10.20 kHz spinning speed (see Table 2). However, the overlap of the contour lines of I_{\pm}/I_0 for $Sr_5F(PO_4)_3$ spinning at 10.20 kHz occurs at around $\rho=0.96\pm0.04$ and $\mu=4.0\pm0.19$.

Fig. I-7 shows the Herzfeld and Berger plots of Ba₅F(PO₄)₃ at two different spinning speeds (6.23 kHz and 10.18 kHz). Unlikely the other fluorapatite samples, all contours of Ba₅F(PO₄)₃ at 6.23 kHz except for I₊₃ intersect at one point around $\rho = 0.8 \pm 0.04$ and $\mu = 10.4 \pm 0.13$, and those at a 10.18kHz spinning speed intersect at around $\rho = 0.78 \pm 0.02$ and $\mu = 6.2 \pm 0.13$. The ρ and μ values of the intersection points are used to obtain the chemical shielding tensors (CSA and η) from Eq. (I-29) and (I-30).

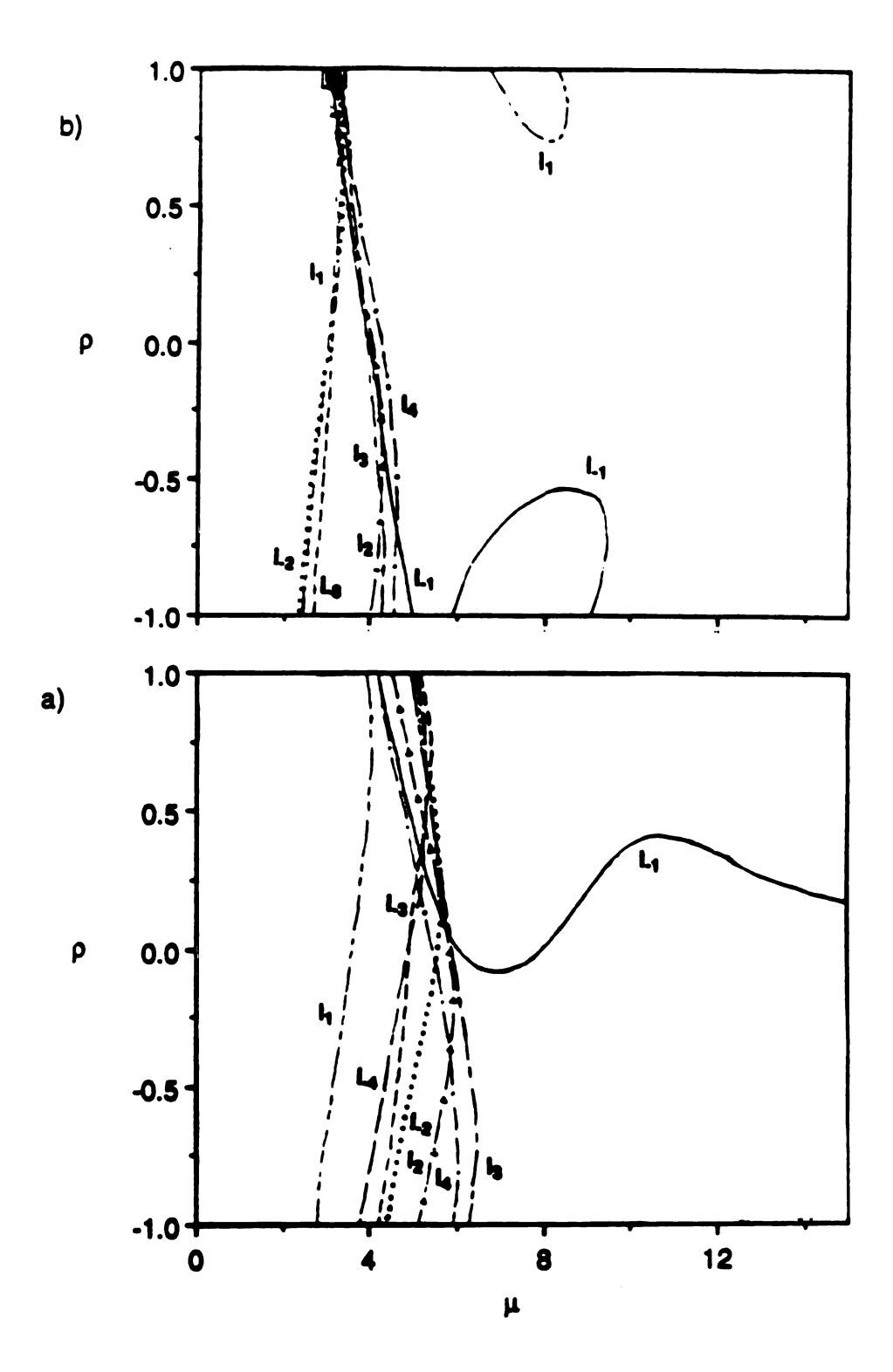


Figure I-5. Contour plots of $Ca_5F(PO_4)_3$ spinning at 6.12 kHz (a) and 10.18 kHz (b) using the Herzfeld and Berger graphical method.

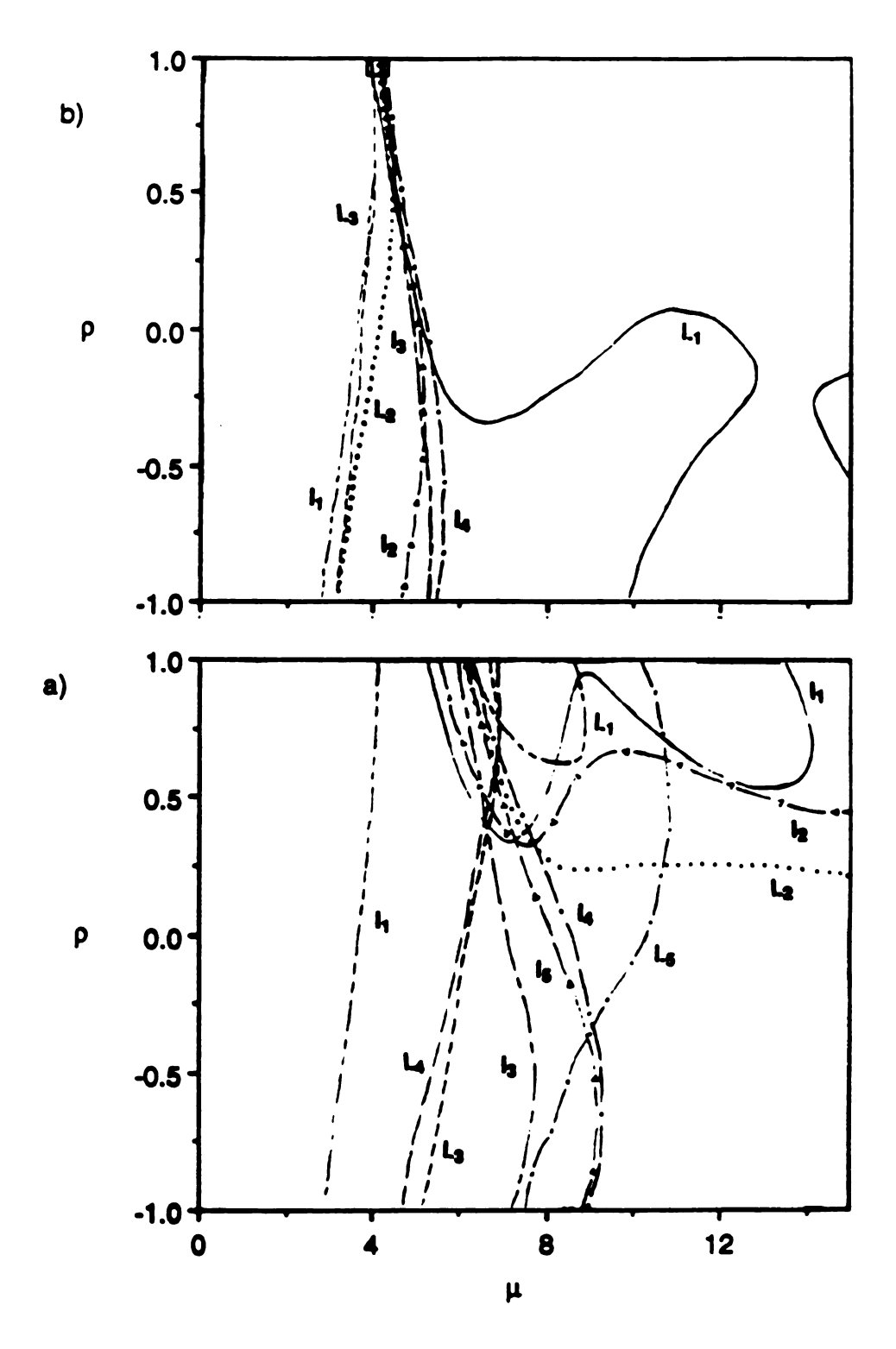


Figure I-6. Contour plots of $Sr_5F(PO_4)_3$ spinning at 6.26 kHz (a) and 10.20 kHz (b) using the Herzfeld and Berger graphical method.

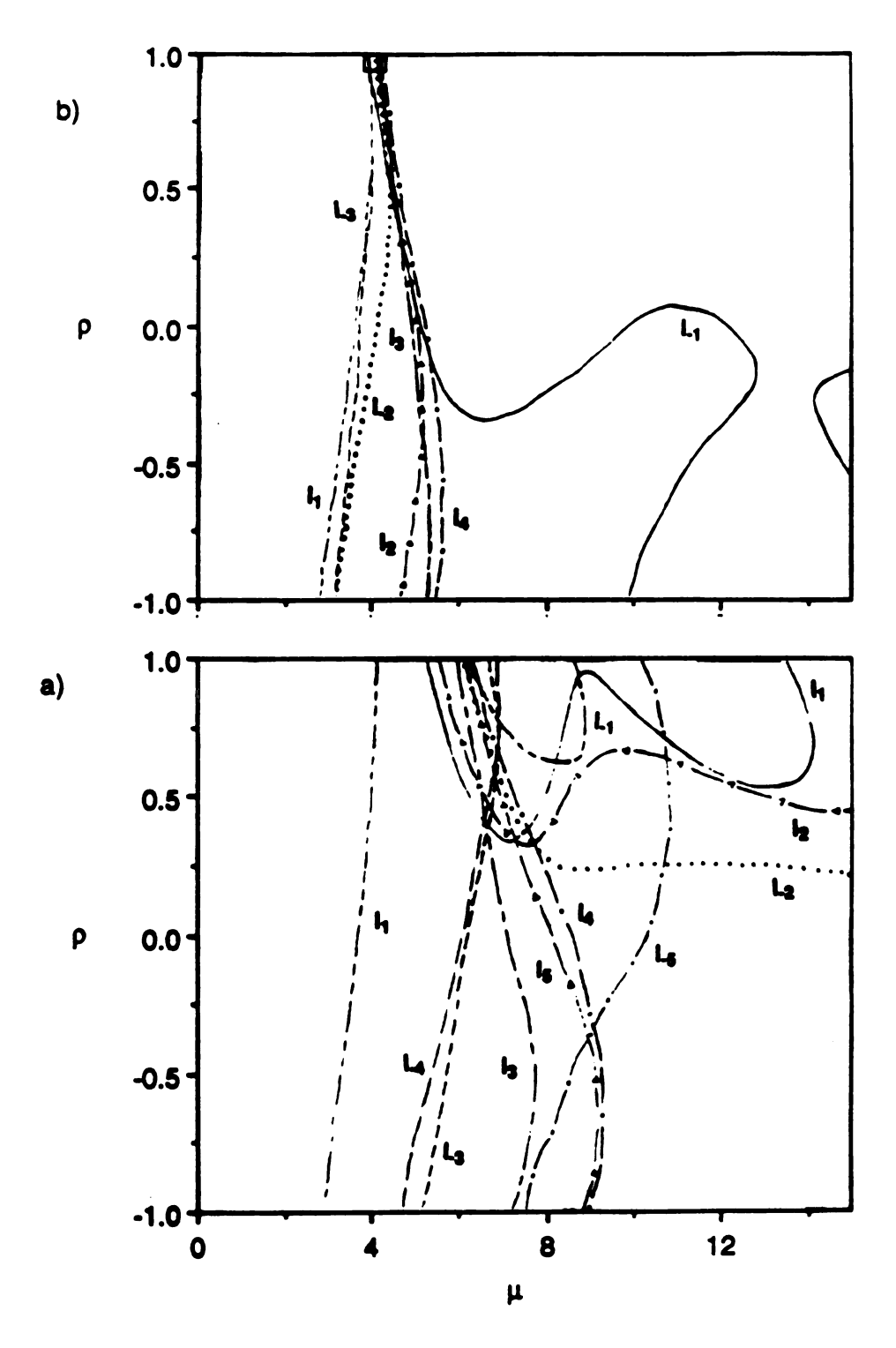


Figure I-6. Contour plots of $Sr_5F(PO_4)_3$ spinning at 6.26 kHz (a) and 10.20 kHz (b) using the Herzfeld and Berger graphical method.

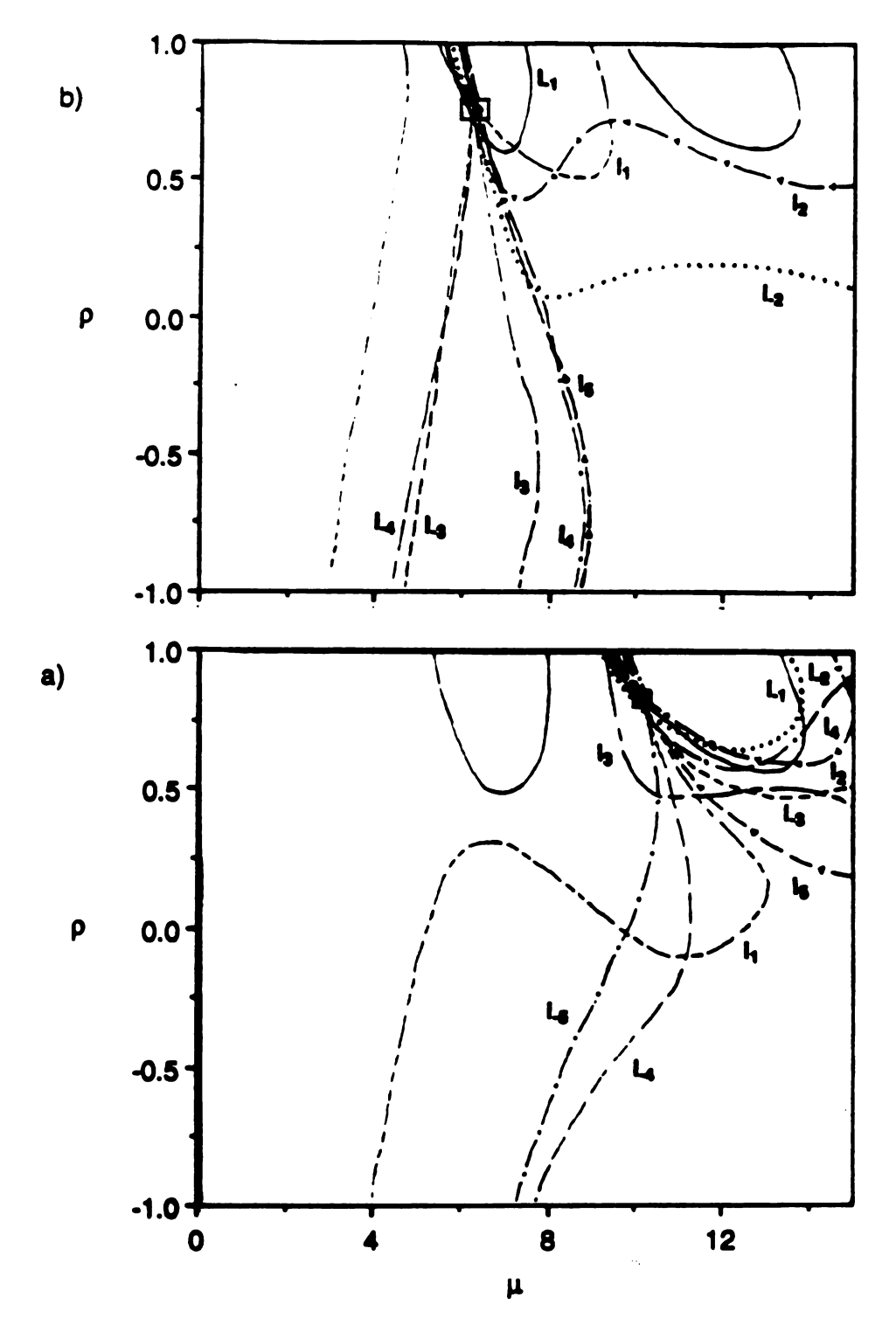


Figure. I-7. Contour plots of $Ba_5F(PO_4)_3$ spinning at 6.23 kHz (a) and 10.18 kHz (b) using the Herzfeld and Berger graphical method.

Table 2. The ¹⁹F chemical shift anisotropy (CSA) and asymmetry parameter η of M₅F(PO₄)₃ obtained using the Herzfeld and Berger graphical method and integrated peak intensities.

	ν_r (kHz)	Measured η	Measured CSA
			(ppm)
Ca ₅ F(PO ₄) ₃	10.18	0.04 ± 0.04	86 ± 5
Sr ₅ F(PO ₄) ₃	10.20	0.06 ± 0.04	107 ± 7
	6.23	0.16 ± 0.03	164 ± 4
Ba ₅ F(PO ₄) ₃	8.19	0.23 ± 0.04	157 ± 7
	10.10	0.18 ± 0.01	158 ± 4
	10.87	0.20± 0.04	160 ± 5

Table 3. 19 F chemical shielding tensors of $M_5F(PO_4)_3$, calculated from the moments method using peak intensities obtained from deconvolution. An average value of the CSA at various spinning speeds was used, along with an assumed η value of zero, to obtain the principal components with respect to C_6F_6 and free F^- ion (parentheses).

	$\sigma_{11}(ppm) \ (= \sigma_{22})$	σ ₃₃ (ppm)	
Ca ₅ F(PO ₄) ₃	35.5 ± 0.2	121.0 ± 0.5	
	(159.5 ± 0.2)	(245.0 ± 0.5)	
Sr ₅ F(PO ₄) ₃	61.4 ± 1.1	168.8 ± 1.9	
	(185.4 ± 1.1)	(292.8 ± 1.9)	
Ba ₅ F(PO ₄) ₃	131.8±0.6	290.8 ± 1.2	
	(255.9 ± 0.6)	(414.9 ± 1.2)	

Table 2 shows the CSA and η values obtained by the graphical procedure of Herzfeld-Berger. The standard deviations are determined by the intersection area (box size in Fig. I-5, I-6 and I-7). The contours of the experimental ratios $l_{\pm i}/l_0$ for $Ca_5F(PO_4)_3$ and $Sr_5F(PO_4)_3$ fail to overlap at spinning speeds below 9kHz but they overlap at 10.18 and 10.20kHz respectively. Therefore, the CSA values of $Ca_5F(PO_4)_3$ and $Sr_5F(PO_4)_3$ are obtained at the high spinning speed. The $l_{\pm i}/l_0$ contours of $Ba_5F(PO_4)_3$ overlap within a small region, and the resultant CSA values are close regardless of the spinning speed.

Even though the measured asymmetry parameters of $M_5F(PO_4)_3$ are different and non-zero at various spinning speeds, the chemical shift tensors of $M_5F(PO_4)_3$ must be axially symmetric on the basis of the X-ray crystal structure. $^{9-11}$ Therefore, we constrain η to be equal to 0 and use the average CSA determined using the moments method to calculate the chemical shift tensors in Table 3. It is necessary to know the chemical shift tensor values on an absolute chemical shielding scale with respect to free fluoride ion in order to be able to calculate the contribution of the sigma- and pi-bonding to the paramagnetic shielding. The isotropic chemical shift of C_6F_6 has been calculated to be 124 ppm with respect to free fluoride ion. 19 The chemical shift tensors of $M_5F(PO_4)_3$ with respect to both C_6F_6 and free F^- (parentheses), obtained using the average CSA from the deconvolution data in Table 1 and assuming $\eta=0$, are shown in Table 3.

Experimental and simulated ¹⁹F MAS-NMR spectra of $M_5F(PO_4)_3$ samples at spinning speeds near 6kHz, using the chemical shift tensor components in Table 3, are shown in Fig. I-8. The isotropic chemical shifts of $M_5F(PO_4)_3$ (M=Ca, Sr, and Ba) are 64.0, 97.2, and 184.8 ppm from hexafluorobenzene respectively. The half-height linewidths of the centerbands of $Ca_5F(PO_4)_3$, $Sr_5F(PO_4)_3$, and

Ba₅F(PO₄)₃ without line-broadening are 164 Hz, 385 Hz and 438 Hz respectively.

Brunner et. al. have used average Hamiltonian theory to provide a general expression for the MAS-NMR linewidths of spins with axially symmetric shielding tensors. Their expression takes into account homo- and heteronuclear dipolar interactions and CSA, and predicts a half-height linewidth (HHLW) that is inversely proportional to the spinning speed. Figure I-9 shows a plot of the ¹⁹F MAS-NMR centerband HHLW vs. spinning speed for $M_5F(PO_4)_3$ (M = Ca, Sr, and Ba). The HHLW of $Ca_5F(PO_4)_3$ decreases monotonically with increasing spinning speed within experimental error, but those of $Sr_5F(PO_4)_3$ and $Ba_5F(PO_4)_3$ do not. The dependence of the linewidth of $M_5F(PO_4)_3$ upon spinning speed indicates that the linewidth is broadened homogeneously. The "plateau" value of the HHLW increases as the CSA increase (from Ca to Sr to Ba); this may simply reflect larger effects of crystal imperfections upon the isotropic shifts of $Sr_5F(PO_4)_3$ and $Ba_5F(PO_4)_3$.

B. Solid Solutions of Ca/Sr Fluorapatite

The ¹⁹F MAS-NMR spectrum of Ca_{8.97}Sr_{1.03}F₂(PO₄)₆ spinning at 8.23 kHz is shown in Fig. I-10a. It is very difficult to unravel the isotropic chemical shifts and their sidebands at a fixed spinning speed due to the overlap of the different centerbands and sidebands. Since the sidebands are located at integral multiples of the spinning speed from the centerband, we can differentiate between the centerband of one peak and a sideband from another peak with a different isotropic chemical shift simply by increasing the spinning speed. In this way, three isotropic chemical shifts of the peaks in Ca_{8.97}Sr_{1.03}F₂(PO₄)₆ (Fig. I-10b) can be obtained, at 64 ppm, 79.6 ppm, and 97 ppm. Overlap of centerband and sideband peaks makes it difficult to obtain reliable integral intensities of individual peaks in the

35

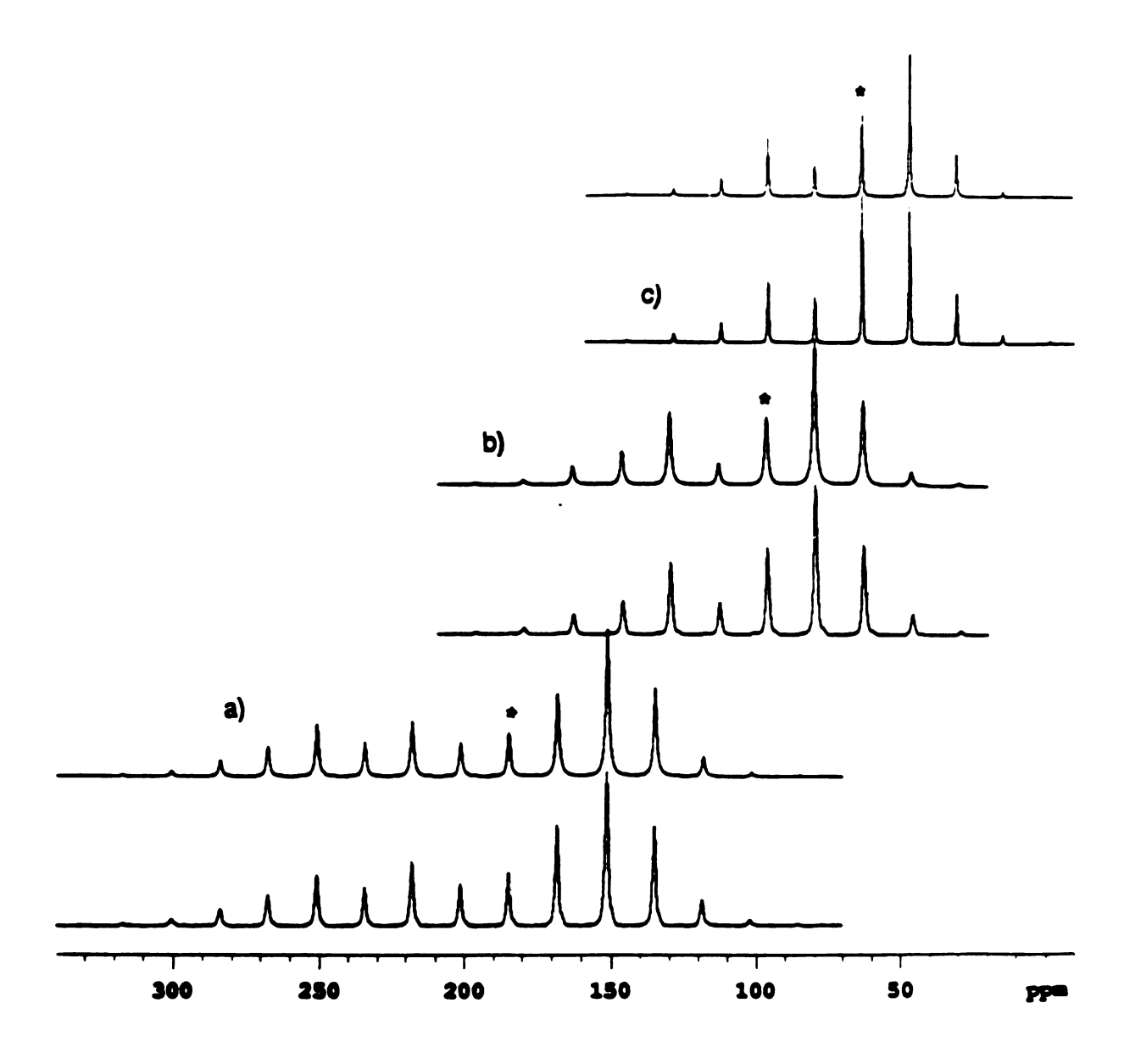


Figure I-8. The experimental (lower) and simulated (upper) spectra of $M_5F(PO_4)_3$. a) $Ba_5F(PO_4)_3$ at 6.23kHz; b) $Sr_5F(PO_4)_3$ at 6.26kHz; c) $Ca_5F(PO_4)_3$ at 6.12kHz. * indicates the centerband (σ_i). Simulation were based on the chemical shift tensor components in Table 3, and neglect dipolar coupling.

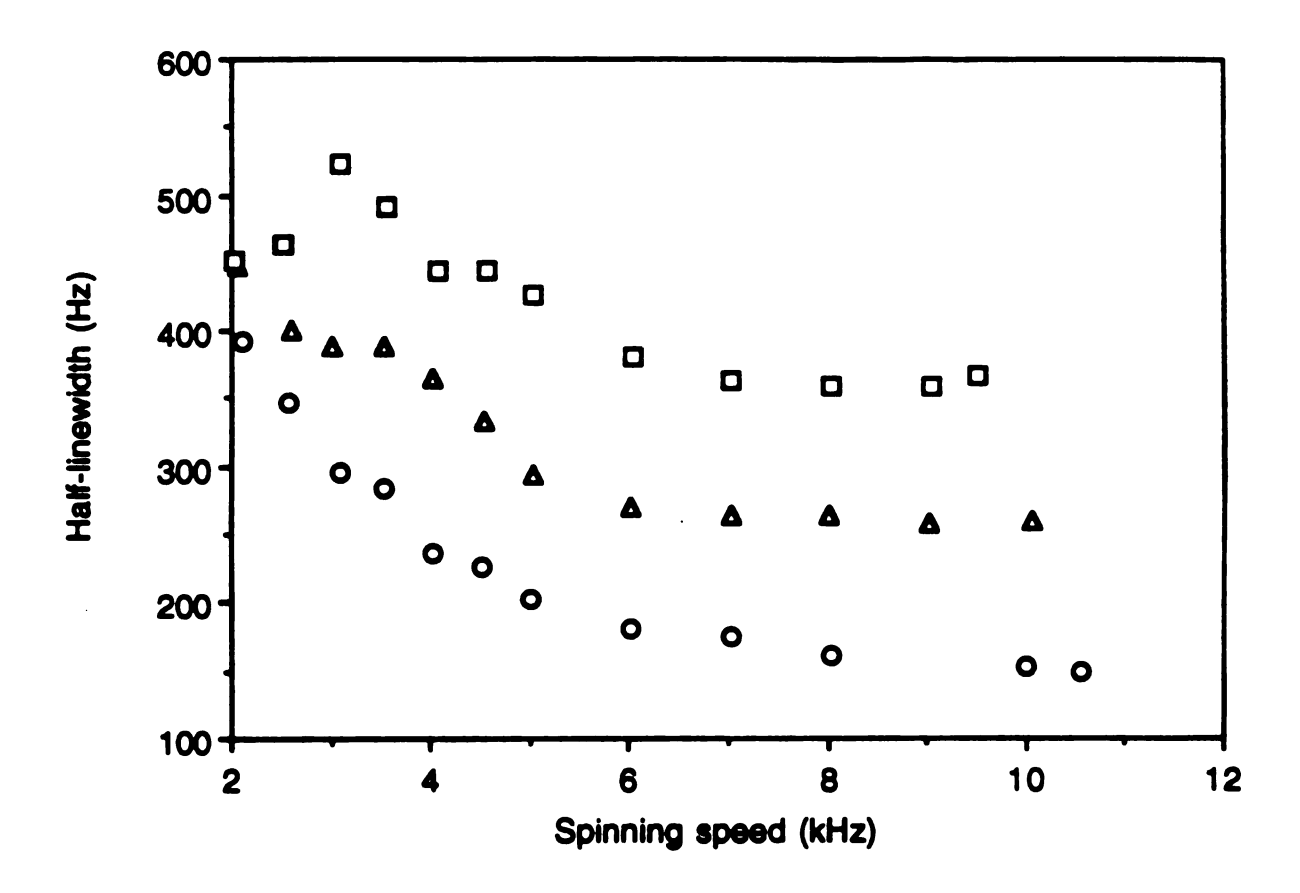


Figure I-9. ¹⁹F MAS-NMR center band HHLW vs. spinning speed for $M_5F(PO_4)_3$ (M = Ca, Sr, Ba). $Ca_5F(PO_4)_3$ (open circle), $Sr_5F(PO_4)_3$ (open triangle), and $Ba_5F(PO_4)_3$ (open square).

spectrum. From Fig. I-10b, only the integrated intensity of the centerband and sidebands of the 79.6 ppm peak can be measured since the other centerbands and sidebands overlap. The ratio of the integrated intensity of the centerband and sidebands of the 79.6 ppm peak to the total integral intensity in Fig. I-10b is 29 %.

The deconvoluted spectra of the 64 ppm peak and also the peak near 51 ppm due to the -1 sideband of the 79.6 ppm peak of Fig. I-10b are shown in Fig. I-11. Three peaks can be deconvoluted from the asymmetric 64 ppm peak. The gaussian fractions of peaks I and II are 0.88, and that of peak III is 0.68. The half-height linewidths of deconvoluted peaks I, II, and III are 454, 536, and 758 Hz respectively. The percentages of the integral intensity of deconvoluted peaks I, II and III are 45.4, 37.3 and 17.4 %

Fig. I-12 shows the ¹⁹F MAS-NMR spectrum of $Ca_{8.97}Sr_{1.03}F_2(PO_4)_6$ obtained using the SPARTAN pulse sequence at 10.87 kHz.²⁰ The transmitter offset of this experiment was set to invert the 64 ppm peak, leaving the other peaks unperturbed. Since the pulses in the DANTE train are repeated every rotor period, the sidebands of the 64 ppm peak are also inverted. The mixing times are 0.1, 1, 3, 6, 9, 12, 15, 18, 21, 24, and 30 seconds. As the mixing time increases, the intensities of adjacent peaks decrease while those of the centerband (and sidebands, not shown) of the 64 ppm peak recover quickly compared to the spin-lattice relaxation time of $Ca_{8.97}Sr_{1.03}F_2(PO_4)_6$ (T₁ = 101 second).

Fig. I-13 show the ¹⁹F MAS-NMR spectra of $Ca_5Sr_5F_2(PO_4)_6$ spinning at 8.25 kHz and 10.30 kHz. The centerbands are resolved by spinning at 10.30 kHz. The values of the isotropic chemical shifts in $Ca_5Sr_5F_2(PO_4)_6$ are 69.7ppm, 86.8 ppm, and 104.5 ppm, which are about 6 ppm downfield compared to those in $Ca_{8.97}Sr_{1.03}F_2(PO_4)_6$. The measurement of the integral intensity of peaks is

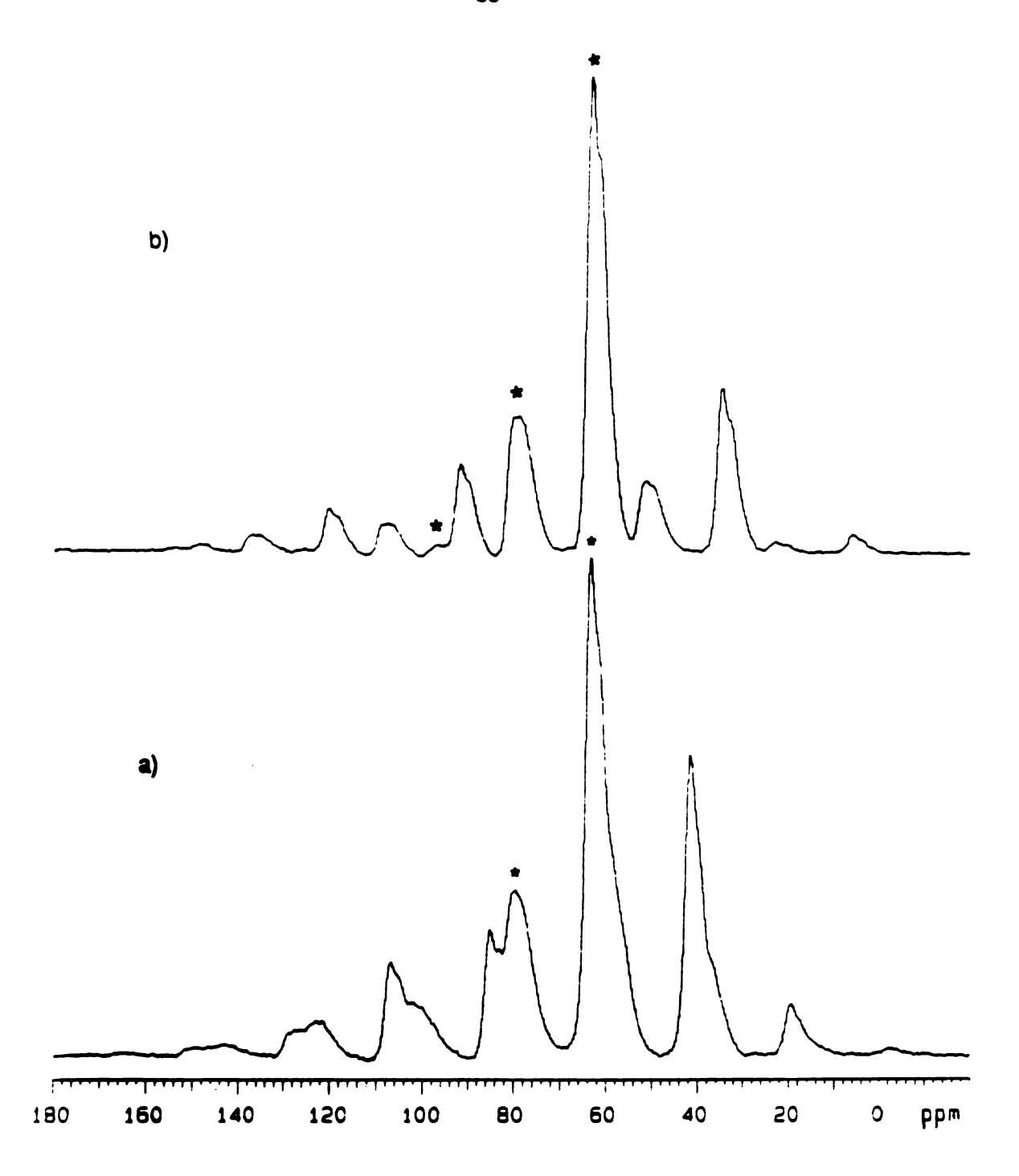


Figure I-10 19 F MAS-NMR of Ca_{8.97}Sr_{1.03}F₂(PO₄)₆ spinning at 8.23 kHz (a) and at 10.80 kHz (b). * indicates the centerband.

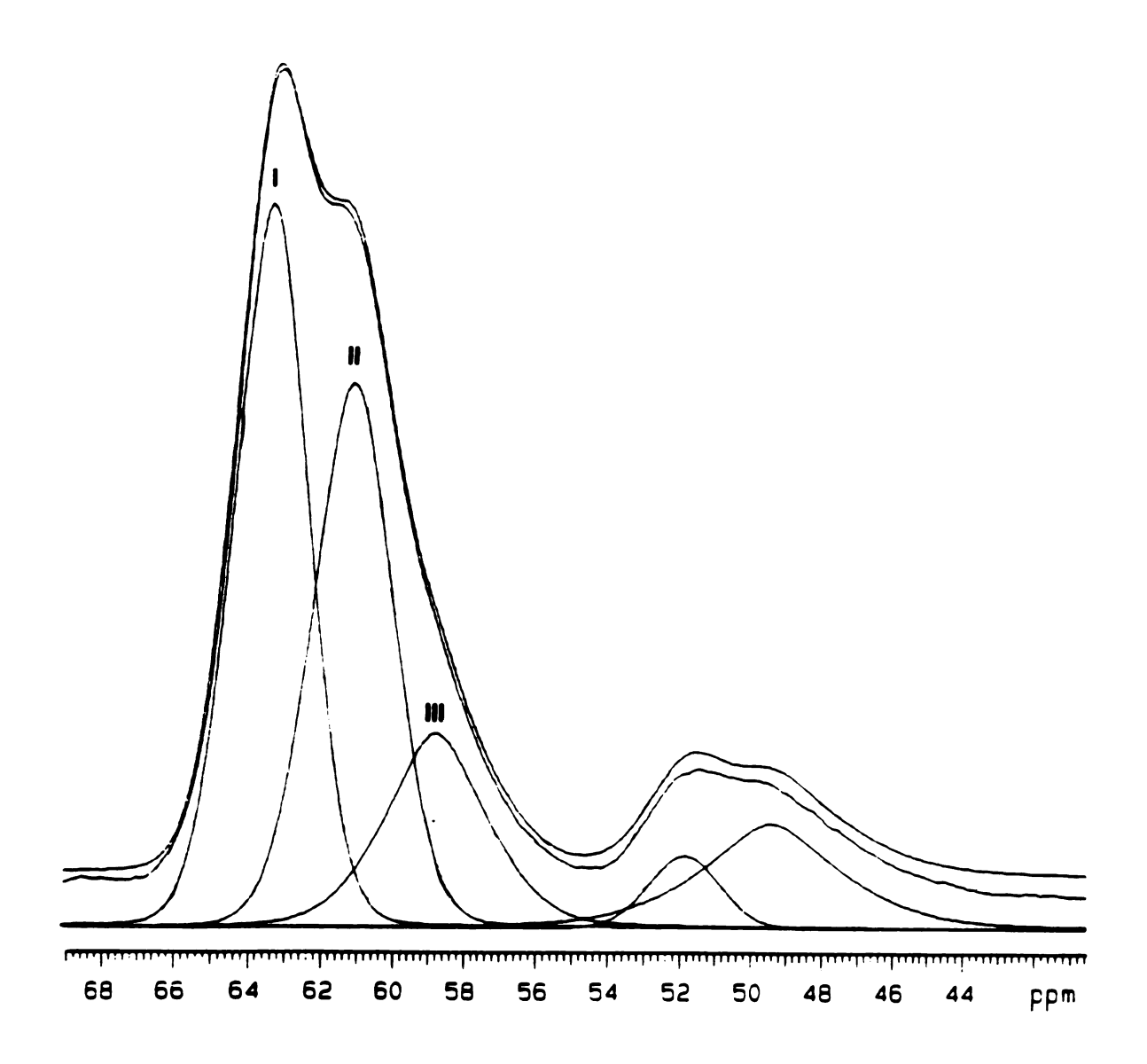


Figure I-11. Deconvolution spectrum of 64 ppm peak in Fig. I-11b

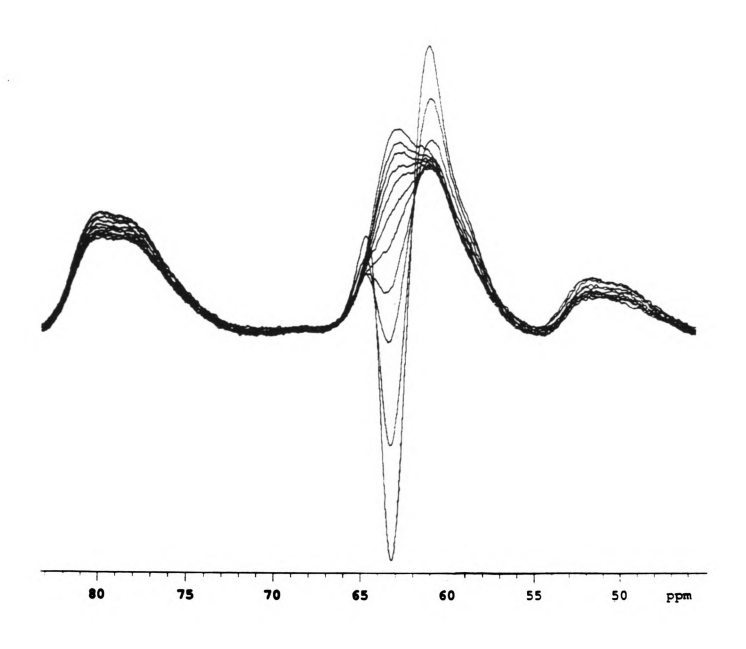


Figure I-12. 19 F MAS-NMR spin diffusion experiment of Ca_{8.97}Sr_{1.03}F₂(PO₄)₆ using SPARTAN pulse sequence spinning at 10.87 kHz. Mixing times are 0.1, 1, 3, 6, 9, 12, 15, 18, 21, 24, and 30 seconds. (See text)

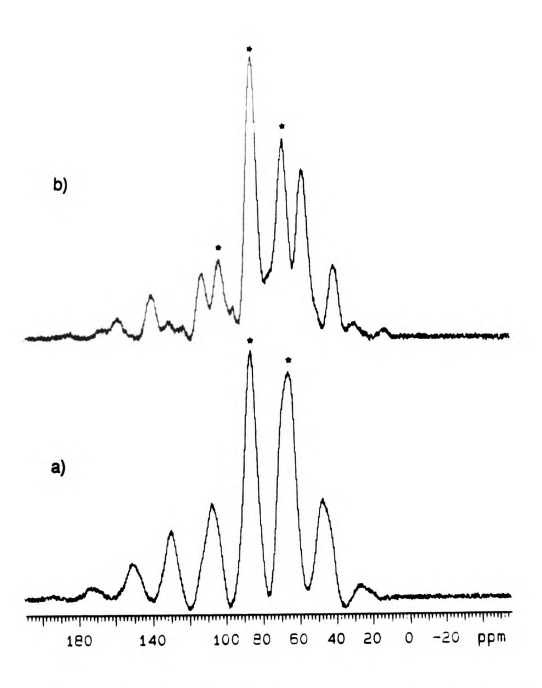


Figure I-13. 19 F MAS-NMR of Ca $_5$ Sr $_5$ F $_2$ (PO $_4$) $_6$ spinning at 8.25 kHz (a) and at 10.30 kHz (b). * indicates centerband.

hindered by the overlap of the centerbands and sidebands.

7. Discussion

A. Measurement of the ¹⁹F Chemical Shift Anisotropies of M₅F(PO₄)₃ Using Different Methods

The values for M₅F(PO₄)₃ are obtained by using two different methods, the moments method and the Herzfeld and Berger graphical method. In the moments method, the accurate measurement of the second and third moments of MAS-NMR spectra is difficult in general because of the low signal:noise ratio of the weak higher order sidebands that contribute significantly to the moments.²⁵ The homo- and heteronuclear dipolar interactions also contribute to the experimental second moment, making it difficult to separate their contribution to the second moment from that of the CSA alone. We will discuss how the dipolar interaction influences the measurement of the CSA using the moments analysis method. MAS-NMR simulations using ANTIOPE (Fig. I-14a) show that the including homonuclear dipolar interactions result in a higher intensity of the centerband relative to that of the sidebands. The contribution of the homo- and heteronuclear dipolar interactions and of the CSA to the second moment is not simply additive.¹⁴ The values of the CSA obtained from the simulated ¹⁹F MAS-NMR spectra calculated using the CSA alone (VNMR 3.2) and using the CSA along with dipolar interactions (ANTIOPE) differ by approximately 2 ppm at the spinning speed of 6.12 kHz. Since the low signal:noise ratio of the weak higher order sidebands gives rise to measurement errors in the experimental and since considering the dipolar interaction can slightly change the values of the CSA, we use the moments measured from the intensities of the sidebands of the experimental spectra to

obtain the values of the CSA in Table 1.

When we use the Herzfeld and Berger graphical method, the chemical shift tensors are obtained from the coordinates of the overlapping contours of the values of I±i/Io ratios. Intensities of all peaks (a centerband and sidebands) in a MAS spectrum are used to obtain a CSA with the moments method, whereas those of a limited number of peaks are used to obtain a CSA with the Herzfeld and Berger graphical method ($l_{\pm i}/l_0$ ratios for up to \pm 5 sidebands). Thus, the measurement error of the CSA obtained from the Herzfeld and Berger graphical method should be less severe than that from the moments method owing to the neglect of weak higher order sidebands. The $l_{\pm i}/l_0$ ratios of the samples with a larger CSA and small dipolar interactions have a smaller relative contribution from the dipolar interactions. The dipolar interaction decreases on going from Ca₅F(PO₄)₃ to Ba₅F(PO₄)₃ as a result of the expansion of the lattice, ⁹⁻¹¹ whereas the CSA values increase going from Ca₅F(PO₄)₃ to Ba₅F(PO₄)₃. Therefore, it is not surprising that the contours of Iti/Io for Ba5F(PO4)3 overlap at one point or over a small region at all spinning speeds. Likewise, the contours of $l_{\pm i}/l_0$ for Ca₅F(PO₄)₃ and Sr₅F(PO₄)₃ fail to overlap below about 9kHz due to the greater size ratio between the homonuclear dipolar interaction and the CSA. As the spinning speed increases, the higher order sideband intensity contribution from the dipolar interaction appear to decrease quickly. Thus, most of the intensity of the higher order sidebands at high spinning speeds is due to the CSA. Figures I-5 and 6 show that the value of μ of the +1 sideband is insensitive to a change of the spinning speed. The values of μ of the other sidebands move to the value of μ of the +1 sideband with an increasing in the spinning speed.

The integrated intensity of each peak in the experimental spectrum does not

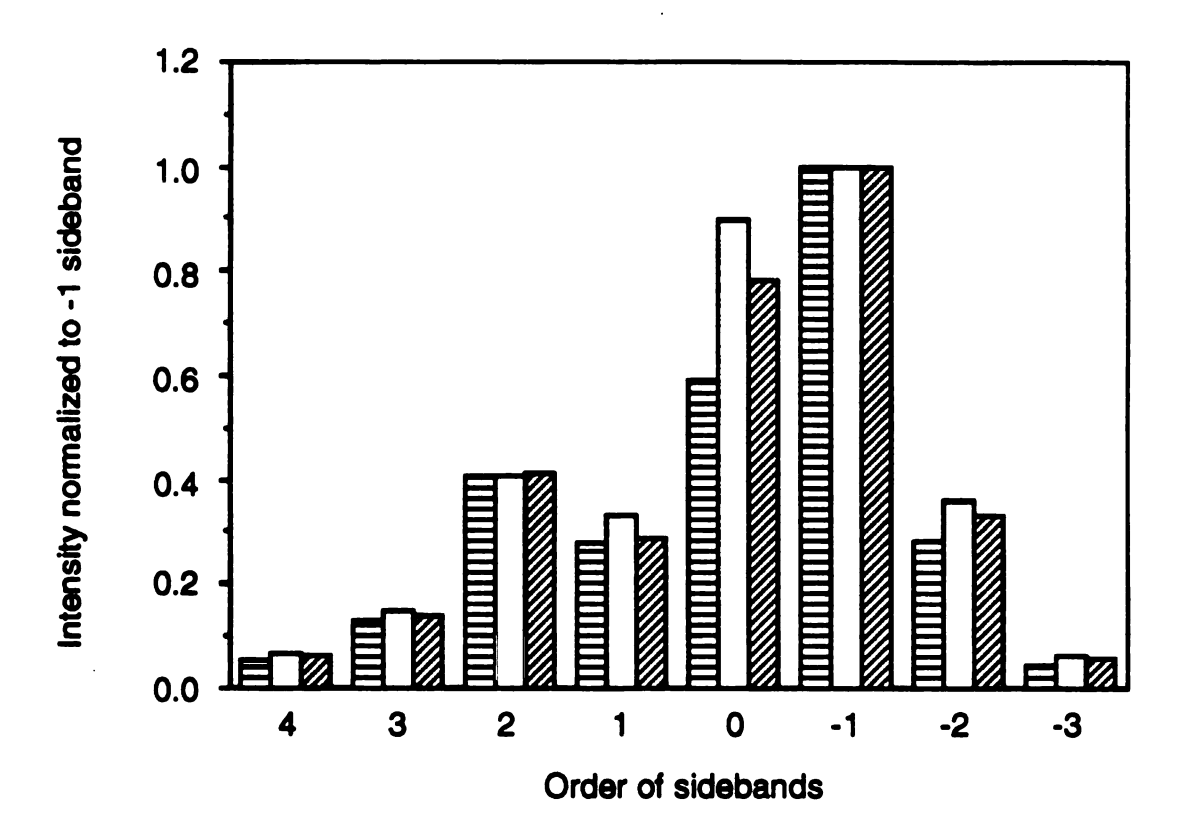
correspond to the peak height because of differences in the half-height linewidth of the peaks. For example, the peak height of the centerband in $Ca_5F(PO_4)_3$ is larger than that of the -1 sideband; however, the integrated intensity of the centerband in $Ca_5F(PO_4)_3$ is less than that of the -1 sideband since the half-height linewidth of the centerband (164 Hz) is smaller than that of the -1 sideband (217Hz) (Fig. I-10). The ratio of the integrated intensity of the centerband to that of the -1 sideband is 1.00:1.13 in Fig. I-10. Thus, when CSA is obtained by using MAS-NMR, the integrated peak intensity must be used rather than a peak height to obtain a more accurate CSA value.

Since the linewidth of the sidebands in the experimental spectra vary for a given sample, it is convenient to represent these spectra as stick spectra for comparison with simulated spectra. Stick spectra (Figure I-14) normalized to the -1 sideband of $M_5F(PO_4)_3$ were obtained from simulation (ANTIOPE and VNMR 3.2) with the parameters of Table 3. The intensities of the centerband and sideband of the simulated stick spectra taking into account only chemical shift anisotropy (VNMR simulation) are different from those of the experimental spectrum in Fig. I-14a. The simulated spectrum obtained using ANTIOPE (CSA and dipolar interaction among uniformly-spaced five fluorine spins) more closely resemble the experimental spectrum in Fig. I-14a. Fig. I-14 shows that the intensity differences between the centerband and sidebands of the simulated and experimental stick spectra become smaller and smaller less going on from $Ca_5F(PO_4)_3$ to $Ba_5F(PO_4)_3$.

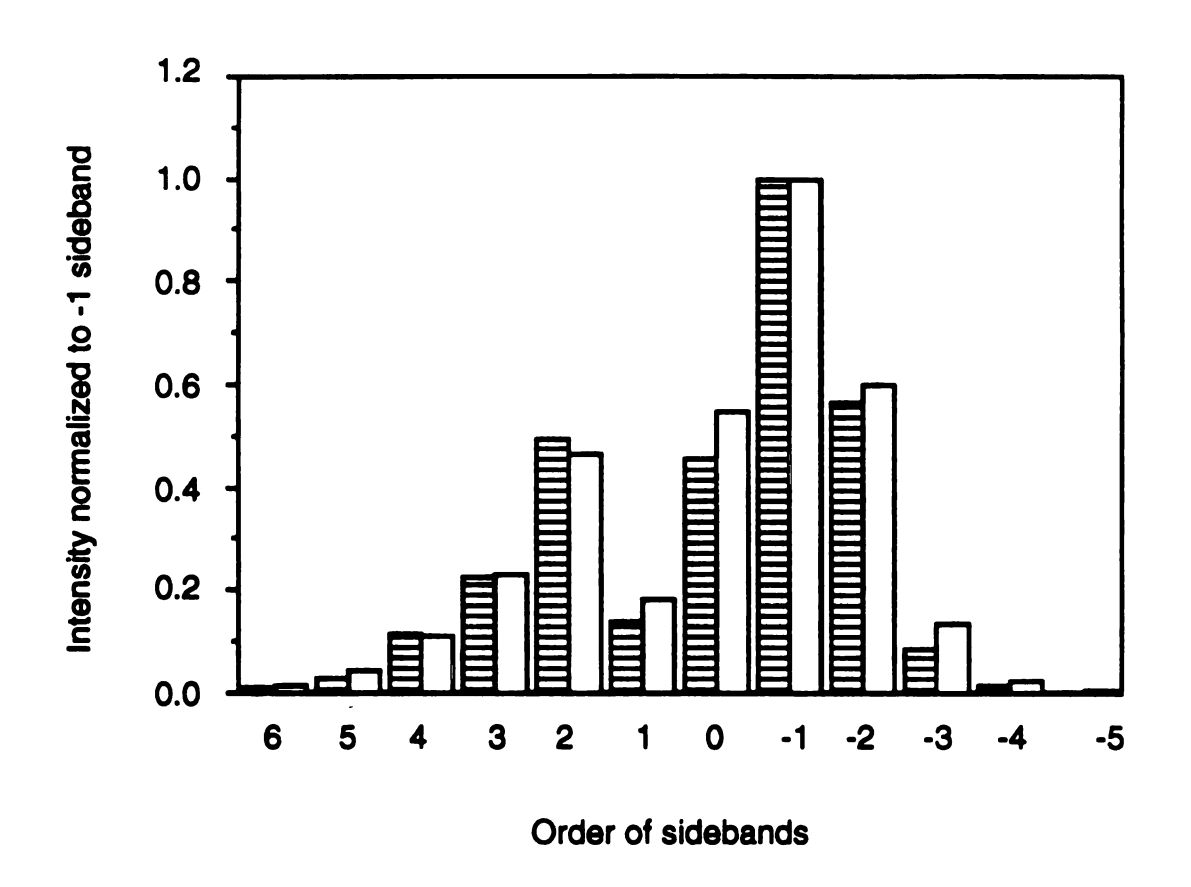
B. Separation of Metal-Fluoride Sigma- and Pi-Bonding Contributions to the ¹⁹F Shielding Tensor

The chemical shielding of a nucleus can be separated according to Ramsey's

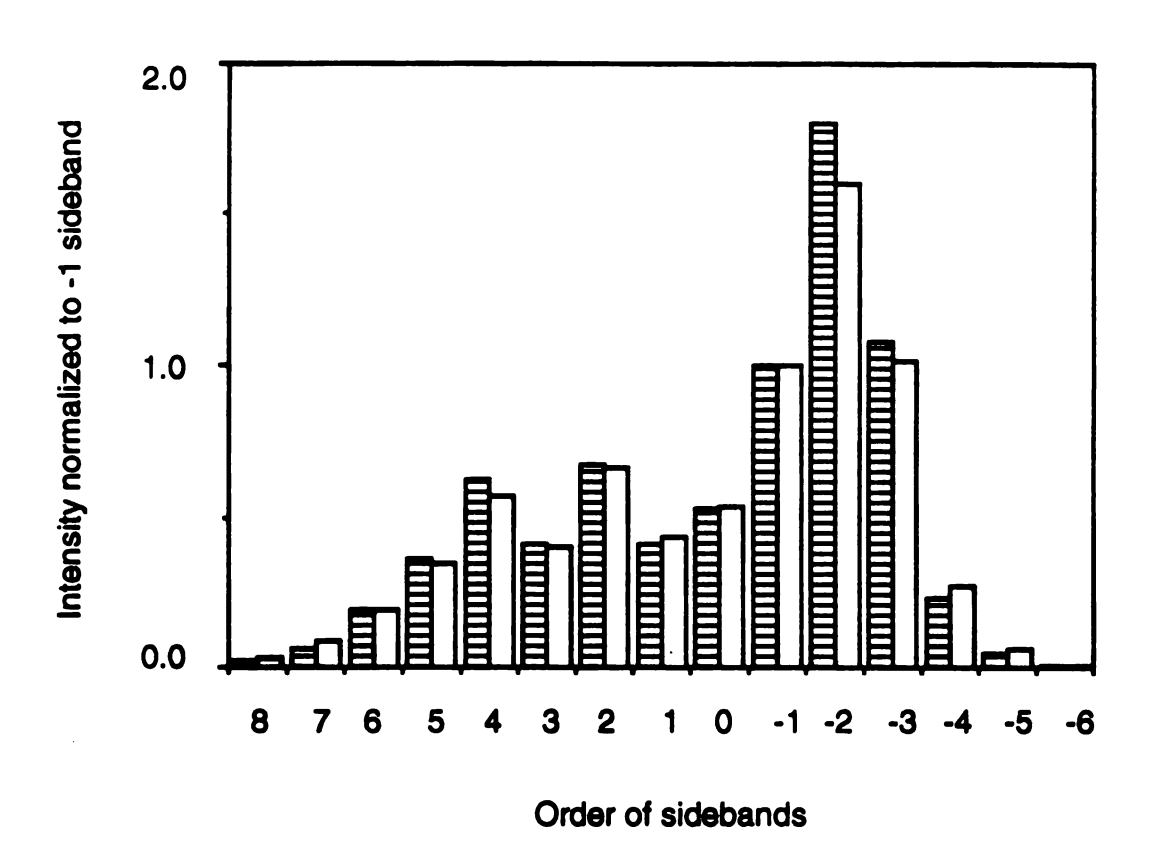
Figure I-14. Comparison of simulated and experimental ^{19}F MAS-NMR stick spectra of $M_5F(PO_4)_3$ at the same spinning speed. The asymmetry parameter η is forced to be zero and the average CSA values of $M_5F(PO_4)_3$ obtained from the moments method are used, and all peaks are normalized to the -1 sideband.



- ☐ The intensity (from deconvolution) of the centerband and sidebands of the experimental spectrum.
- The intensity of the centerband and sidebands due to the CSA only (VNMR 3.2 simulation).
- The intensity of the centerband and sidebands due to the CSA and dipolar interactions among 5 fluorine spins (ANTIOPE simulation).
- a) Simulated and experimental ¹⁹F stick spectra of Ca₅F(PO₄)₃ spinning at 6.12 kHz



- ☐ The intensity (from deconvolution) of the centerband and sidebands of the experimental spectrum.
- The intensity of the centerband and sidebands due to the CSA only (VNMR 3.2 simulation).
- b) Simulated and experimental ¹⁹F stick spectra of Sr₅F(PO₄)₃ spinning at 8.20 kHz



- The intensity (from deconvolution) of the centerband and sidebands of the experimental spectrum.
- The intensity of the centerband and sidebands due to the CSA only (VNMR 3.2 simulation).
- c) Simulated and experimental ¹⁹F stick spectra of Ba₅F(PO₄)₃ spinning at 8.19kHz

formulation^{26,27} into a diamagnetic term and a paramagnetic term. Lamb showed that the diamagnetic contribution to shielding is proportional to the sum of inverse distances between the i-th electrons and the nucleus.²⁸ The calculated difference in the diamagnetic term for free fluoride ions in different ionic fluorides is small since the distances of the i-th electrons to the nucleus for a free F- ion are similar to those for different ionic fluorides.²⁷ Therefore, differences in the paramagnetic term are largely responsible for the fluorine chemical shift changes observed in various ionic fluorides. The chemical shielding tensors of the paramagnetic term, measured with respect to free fluoride ion are used to separate metal-fluoride sigma- and pi-bonding contributions to the ¹⁹F shielding. The paramagnetic contribution depends upon the electronic ground and excited states. The paramagnetic contribution of electrons in s orbitals can be ignored, since the angular momentum of s orbitals is zero. An asymmetric distribution of p and d electrons near the nucleus, and low-lying excited states of these electrons. can result in a large paramagnetic term. 26,27 A superposition of the ground and excited states of sigma-bonding orbitals arises when an external magnetic field is applied. The angle between a single sigma-bond and the external magnetic field determines the mixing of the states. No perturbation of the symmetry of the electron cloud occurs when the external magnetic field is along the sigma-bond. The shielding constant arising from the paramagnetic term in linear compounds depends on the angle between the external magnetic field and the direction of the sigma-bond in the following way. 26,29

$$\sigma(\theta) = \mathbf{a}_{\sigma} \sin^2 \theta \tag{I-32}$$

where $\sigma(\theta)$ is the paramagnetic shielding constant at angle θ and a_{σ} represents the contribution of the σ -bond to the paramagnetic shielding. Since the pi orbital

is perpendicular to the bond direction, the shielding constant due to the pi-bond is represented by

$$\sigma(\theta) = a_{\pi} \cos^2 \theta \tag{I-33}$$

where a_{π} represents the contribution of the pi-bond to the paramagnetic shielding, and θ is the angle between the bond and the external magnetic field. The paramagnetic shielding term arising from both a sigma-bond and a pi-bond is the sum of equations (I-32) and (I-33)

$$\sigma(\theta) = a_{\sigma} \sin^2 \theta + a_{\pi} \cos^2 \theta = (2/3)a_{\sigma} + (1/3)a_{\pi} + (1/3)(a_{\pi} - a_{\sigma})(3\cos^2 \theta - 1).$$
 (I-34)

The isotropic portion of the shielding $\sigma_i(\theta = 54.7^\circ)$ is represented by $(2/3)a_\sigma + (1/3)a_\pi$. The total paramagnetic shielding σ is assumed to be the sum of the contributions from the individual bonds;

$$\sigma (\theta) = \sum \sigma_i(\theta_i) \tag{I-35}$$

Gagarinski el.²⁹ separated the paramagnetic shielding components (a_{σ} and a_{π}) of $Ca_5F(PO_4)_3$ by using equations I-34 and I-35, and experimental values for the CSA and the isotropic chemical shift. When σ_{33} is parallel to the external magnetic field, the angle between the external magnetic field and the three Ca - F bonds is perpendicular. From the equations I-34 and I-35, σ_{33} ($\theta = 90^{\circ}$) and σ_i ($\theta = 54.7^{\circ}$) can be represented by the following equations

$$\sigma_{33} = 3 \left[\frac{2}{3} a_{\sigma} + \frac{1}{3} a_{\pi} + \frac{1}{3} (a_{\pi} - a_{\sigma}) (3 \cos^2 90^{\circ} - 1) \right] = 3a_{\sigma}$$
 (I-36);
 $\sigma_{i} = 2a_{\sigma} + a_{\pi}$. (I-37)

Table 4 shows the a_{σ} and a_{π} values calculated with respect to free F⁻ ion at zero ppm (since the latter has no paramagnetic contribution to its shielding), whose shift has been estimated theoretically in Ref. 29. We have assumed that the Sr⁺⁺ ions in Sr₅F(PO₄)₃ form a plane containing the F₋ ion, since this is known

Table 4.¹⁹F paramagnetic shielding parameters a_{σ} and a_{π} for $M_5F(PO_4)_3$ calculated from the chemical shielding tensors (absolute chemical shift scale) in Table 3.

	a_{σ} (ppm)	a_{π} (ppm)
Ca ₅ F(PO ₄) ₃	81.7 ± 0.1	24.6 ± 0.3
Sr ₅ F(PO ₄) ₃	97.6 ± 0.6	26.0 ± 1.2
Ba ₅ F(PO ₄) ₃	138.4 ± 0.4	32.1 ± 0.8

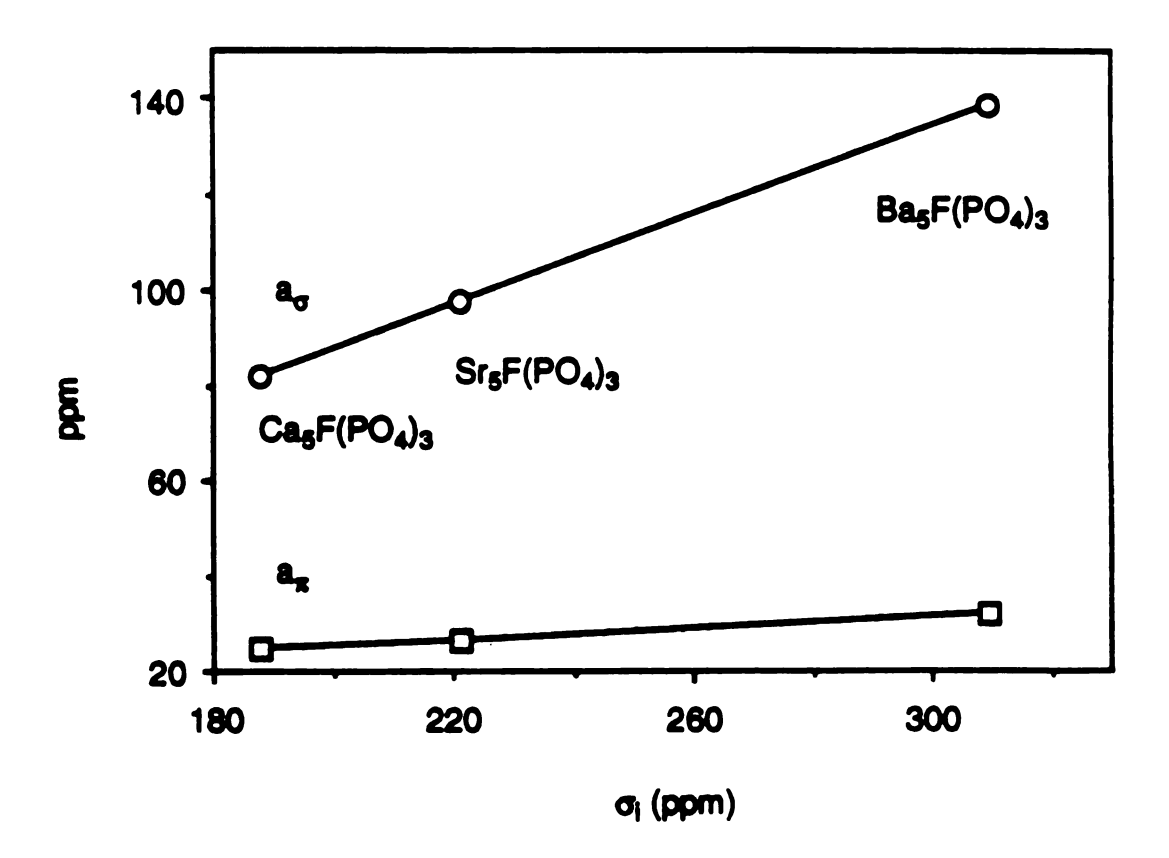


Figure I-15. a_{σ} and a_{π} for $M_5F(PO_4)_3$ vs. ¹⁹F isotropic chemical shift with respect to free F⁻ ion. The solid lines simply connect the data points; open circles and open squares denote a_{σ} and a_{π} respectively.

to be the case for Ca and Ba fluorapatite.^{9,11} The increase in a_{σ} and a_{π} from $Ca_5F(PO_4)_3$ to $Ba_5F(PO_4)_3$ indicates more contributions to the paramagnetic shielding, but not "increased bonding" necessary. The a_{σ} and a_{π} values for $Ca_5F(PO_4)_3$, $Sr_5F(PO_4)_3$, and $Ba_5F(PO_4)_3$ are plotted vs. the isotropic chemical shift with respect to free F^- ion in Fig. I-15. Fig. I-15 shows that the slope of a_{σ} vs. the isotropic chemical shift is larger than that of a_{π} vs. the isotropic chemical shift. This observation implies that the observed increase in the paramagnetic shielding term as one goes from Ca to Sr to Ba in $M_5F(PO_4)_3$ (M = Ca, Sr, Ba) is due to primarily to an increase in the sigma-bonding parameter a_{σ} .

C. Study of Site-Preference of Sr²⁺ Ions in Ca/Sr Fluorapatite Solid Solutions

Using ¹⁹F MAS-NMR

The difference in the chemical bonds between a fluoride ion and either calcium or strontium gives rise to the different ¹⁹F chemical shifts of fluoride ions. The fluoride ions of Ca_{8.97}Sr_{1.03}F₂(PO₄)₆ have the four different chemical environments shown in Fig. I-16. Since the structures of A and D represent the local fluoride ion environment in Ca₅F(PO₄)₃ and Sr₅F(PO₄)₃,^{9,10} respectively, we assign the isotropic chemical shifts of A and D in Fig. 3 to 64 and 97 ppm respectively. The isotropic chemical shifts of B and C in Fig. I-16 are predicted using Eqs. I-34 and I-35, and are equal to the sum of the isotropic portions of the shielding of the appropriate number of Ca – F and Sr – F bonds. The configurations B and C in Fig. I-16 have two Ca – F bonds and one Sr – F bond, and one Ca – F bonds and two Sr – F bond respectively, resulting in predicted isotropic chemical shifts of B and C in Fig. I-16 of 75.1 ppm and 86.1 ppm respectively. The isotropic chemical shift of either one is different from the isotropic chemical shift of the peak at 79.6 ppm in Fig. I-10b. There are no centerbands between the centerband at 64 ppm

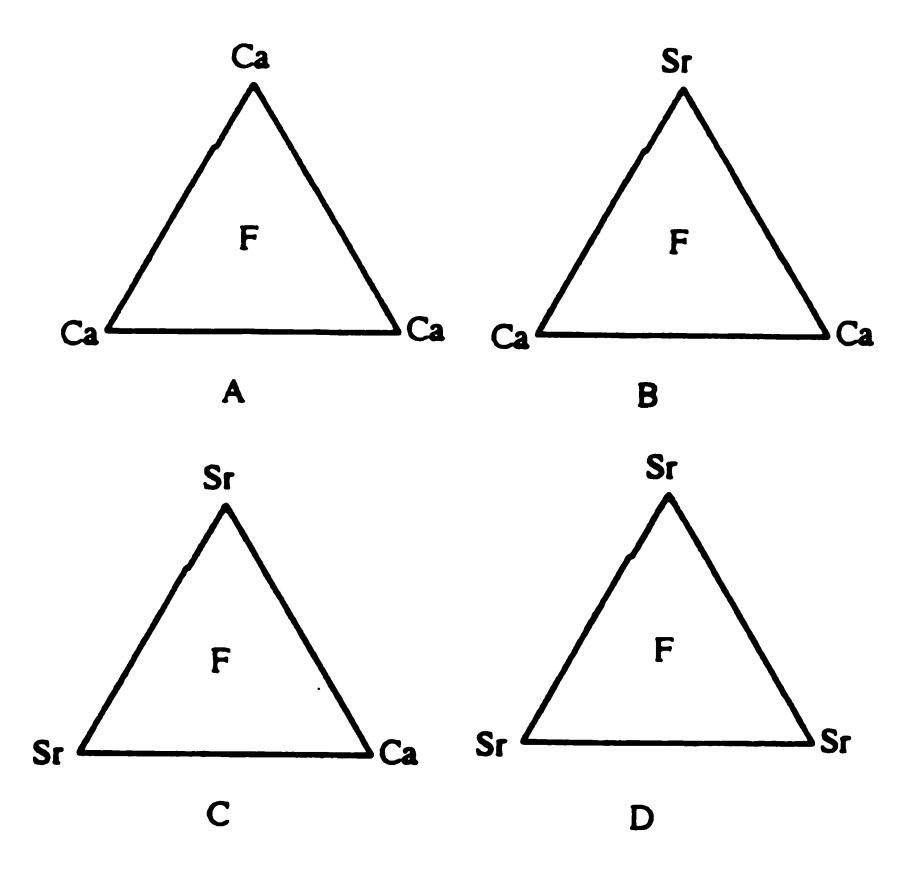


Figure I-16. Substitution of Sr²⁺ in the three nearest neighbor Ca(2) sites of Ca/Sr fluorapatite solid solutions.

and the centerband at 79.6 ppm, and the isotropic chemical shift at 79.6 ppm is the second isotropic chemical shift in the downfield direction in Fig. I-10b. Therefore, we assign the isotropic chemical shift of the configuration B (Sr₁Ca₂F) in Fig. I-16 to the 79.6 ppm peak in Fig. I-11b. The fact that the experimental shift of the configuration B is 4.5 ppm downfield of predicted value is reasonable, since the Sr₃F configuration in the Ca₅Sr₅F₂(PO₄)₆ solids solution is also downfield (by 7ppm) of the shift in Sr₅F(PO₄)₃, presumably due to lattice distortion effect. The isotropic chemical shift due to C in Fig. I-16 may be between 79.6 ppm and 97 ppm, and may be concealed by overlap with the downfield sideband of the 64 ppm peak in Fig. I-10b.

The degree of possible preference of Sr^{2+} ions for a Ca(2) site for Ca/Sr fluorapatite solid solutions can be studied by using both the resolved peaks obtained from ¹⁹F MAS-NMR and from peak deconvolution of overlapping peaks. There are two different types of calcium ions in $Ca_{10}F_2(PO_4)_6$. Since there are 4 Ca(1) ions and 6 Ca(2) ions in two unit cells, we rewrite the formula of $Ca_{8.97}Sr_{1.03}F_2(PO_4)_6$ as $Ca(2)_{6x}Sr(2)_{6y}Ca(1)_{4x'}Sr(1)_{4y'}F_2(PO_4)_6$ (6x + 4x' = 8.97 and 6y + 4y' = 1.03, and x + y = x' + y' = 1). Since the fluorine ions are bonded to Ca(2) and Sr(2) ions, the chemical shift of the fluorine depends on the numbers of Ca(2) and Sr(2) ions to which it is bonded. The integrated areas of the peaks at each chemical shift in Fig. I-16 are represented by the following equations

A =
$$x^3$$
,
B = $3x^2y$, (I-38)
C = $3xy^2$,
D = y^3

where $(A + B + C + D) = (x + y)^3 = 1.0$.

If the strontium ions randomly substitute for the calcium ions in $Ca_{8.97}Sr_{1.03}F_2(PO_4)_6$, the calculated integrated intensity of B from Eq. (I-40) would be 24 %. The experimental value is 29 %, which implies values for x and y of 0.873 and 0.127 respectively. Thus, the experimental integrated intensity of the B peak indicates a 23 % [(0.127 – 0.103)/0.103] site preference of a Sr^{2+} ion for the Ca(2) site in $Ca_{8.97}Sr_{1.03}F_2(PO_4)_6$. Table 5 shows the calculated probabilities of the various configurations for both random substitution and a 23% preference of the Sr^{2+} ions for the Ca(2) site using Eq. (I-38).

The ¹⁹F MAS-NMR peaks in Fig. I-11b are asymmetric and broad, presumably due to perturbations from strontium ions which are substituted in Ca(1) site, or from strontium ions in the next-nearest Ca(2) sites. We now consider what types of strontium ions (strontium ions in Ca(1) or Ca(2) sites) mainly perturb the fluorine peak at 64 ppm. From the crystal structure of calcium fluorapatite, when a single Sr2+ ion substitutes in a Ca(1) site, it potentially perturbs 6 fluorine ions in an equivalent fashion, but a Sr2+ ion substituting for a Ca(2) site perturbs 2 fluorine ions. Thus, the Sr²⁺ ions in Ca(1) sites perturbs a fluorine ions more than that in Ca(2) sites. The perturbation of the chemical shift of the 64 ppm peak should depend on the number of the strontium ions at the next-nearest Ca(2) sites. The schematic arrangements of the metal cations neighboring a fluorine atom resonating near 64 ppm are shown in Fig. I-17. Since the probability of substitution of more than 2 Sr²⁺ ions in Ca(2) sites in Ca_{8.97}Sr_{1.03}F₂(PO₄)₆ is low, configuration III in Eq. (I-39) represents essentially the sum of the probabilities of having $\geq 2 \operatorname{Sr}^{2+}$ ions in Ca(2) sites. The integrated intensities of peaks arising from the individual configurations in Fig. I-17 are then given by the following equations

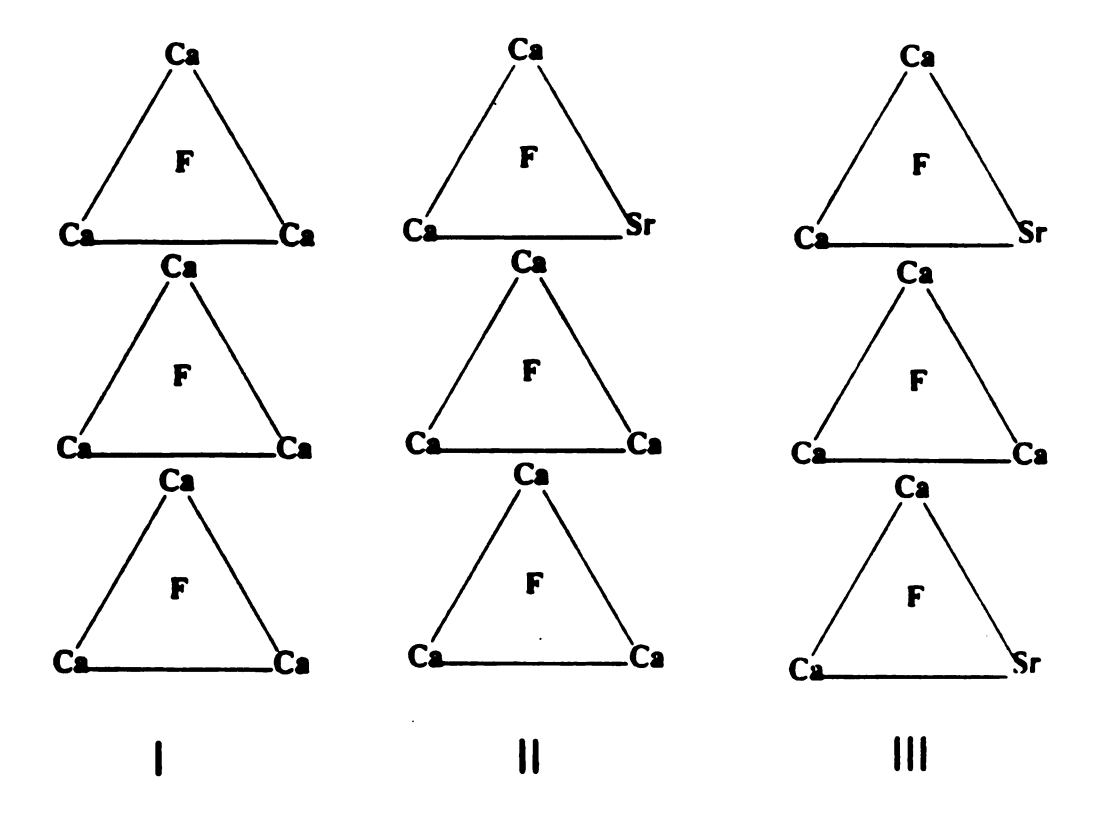


Figure I-17. Possible configurations for single (I) and double (I) Sr⁺⁺ substitution in the six next-nearest neighbor Ca(2) sites of Ca/Sr solid solutions of fluorapatite. The middle equilateral triangle in each configuration represents the observed Ca₃F group resonating around 64 ppm, and the triangles above and below it (along the c-axis), although parallel, are drawn tilted for clarity. One Sr²⁺ ion in the configuration II is either in a top triangle (as shown) or in a bottom triangle. Two Sr²⁺ ions are either in a top triangle or a bottom triangle, or in both triangles (as shown).

Table 5. Calculated probabilities of configurations A-D in $Ca_{8.97}Sr_{1.03}F_2(PO_4)_6$ (Figure I-16) for both random substitution and a 23% preference of Sr^{2++} ions for the Ca(2) sites, and comparison with measured integrated intensity of peak B.

Configuration	Probability, Random substitution	Probability, 23% Preference Ca(2) Site	Integrated MAS-NMR Peak Intensity
A.	72.1%	66.5%	_
B.	24.9%	29.0%	29%
C.	2.9%	4.2%	_
D.	0.1%	0.2%	_
Total	100.0%	99.9%	100%

Table 6. Calculated probabilities of configurations I-III in $Ca_{8.97}Sr_{1.03}F_2(PO_4)_6$ (Figure I-17) for both random substitution and a 23% preference of Sr^{2++} ions for the Ca(2) sites, and comparison with the experimental deconvolution data obtained from the peak near 64 ppm.

Configuration	Probability, Random substitution	Probability, 23% Preference Ca(2) Site	Intensities of Deconvoluted Peak at 64 ppm
1.	52.1%	45.6%	45.4%
II.	35.9%	38.3%	37.3%
III.	12.0%	16.1%	17.4%
Total	100.0%	100.0%	100.1%

$$I = x^6$$

$$II = 6x^5y$$

$$III = 1 - I - II.$$

The comparison of the deconvoluted integrated intensities of the peaks near 64 ppm and the integrated intensities calculated for both random substitutions of Sr^{2+} ions and for a 23 % preference of strontium ions for th Ca(2) site is shown in Table 6. The predictions for a 23% site preference (x=0.877 and y=0.123) are closer to the deconvolution data than those assuming random substitution.

The half-height linewidths of the deconvoluted peaks are broader than those of calcium and strontium fluorapatite (130 Hz at 10.56 kHz, 365 Hz at 10.20 kHz respectively). Since the perturbation effect of strontium ions substituted in the Ca(1) sites on the peak near 64 ppm is small compared to that of strontium ions substituted in the next-nearest Ca(2) sites on the same peak, we believe that the main effect of strontium ions substituting in the Ca(1) site is a slight increase in the half-linewidths of deconvoluted peaks.

To prove that the fluorine spins of the peaks at 64 and 79.6 ppm (see Fig. I-10) are actually in the same phase and not in phase-segregated regions, a spin diffusion experiment was carried out. Spin diffusion is the transfer of Zeeman magnetization between two adjacent spins by means of a spin *flip-flop*. Spin diffusion requires both the existence of a dipole-dipole coupling between the nuclear spins and the conservation of Zeeman energy. Spectral spin diffusion between the peaks having different isotropic chemical shifts under magic-angle-spinning can occur if the Zeeman energy level overlap during a rotor period, the so-called "level-crossing". The existence of level-crossing between two peaks with different isotropic shifts can be demonstrated by calculating the instantaneous

frequencies of the pair of spins in a given crystallite during each part of a rotor cycle.²²

A MAS Hamiltonian can be transformed from the chemical shift principal axis system (PAS) of each crystallite to a reference frame fixed on the rotor.^{32,33} The MAS Hamiltonian for the chemical shift principal axis system becomes periodic (cosine wave), and the offset of the cosine wave depends on the asymmetry parameter and the crystallite orientation. Not only is the amplitude of the cosine wave proportional to the CSA but it also depends on the asymmetry parameter and crystallite orientation.^{32,33}

Fig. I-12 shows the existence of spin diffusion between the peak at 64 ppm and the peak at 79 ppm. The CSA and asymmetry parameter of the peak at 64 ppm are known. Thus, we have to know the CSA and asymmetry parameter of the peak at 79 ppm in order to predict the level-crossing of the two peaks theoretically. We assume that the configuration II of Fig. I-16 is an equilateral triangle and that the fluoride ion in the configuration II is in the middle of the equilateral triangle. The largest chemical shielding tensor σ_{33} is obtained when the external magnetic field is perpendicular to the equilateral triangle in the configuration II. Since the shielding principal values σ_{11} , σ_{22} , σ_{33} are orthogonal, σ_{11} and σ_{22} are on the plane of the equilateral triangle. The smallest chemical shielding component σ_{11} is obtained when the external magnetic field is parallel to a Sr – F bond. From Eq. I-34 and 35, the chemical shielding tensor components σ_{11} , σ_{22} , σ_{33} of configuration II in Fig. I-16 can be represented by

$$\sigma_{11} = \sigma(0^{\circ}) \text{ (Sr)} + \sigma(120^{\circ}) \text{ (Ca)} + \sigma(120^{\circ}) \text{ (Ca)}$$

$$= 3/2 \text{ a}_{\sigma} \text{ (Ca)} + 1/2 \text{ a}_{\pi} \text{ (Ca)} + \text{a}_{\pi} \text{ (Sr)}$$

$$\sigma_{22} = \sigma(90^{\circ}) \text{ (Sr)} + \sigma(30^{\circ}) \text{ (Ca)} + \sigma(30^{\circ}) \text{ (Ca)}$$

$$= 1/2 a_{\sigma} (Ca) + 3/2 a_{\pi} (Ca) + a_{\sigma} (Sr)$$

$$\sigma_{33} = \sigma(90^{\circ}) (Ca) + \sigma(90^{\circ}) (Ca) + \sigma(90^{\circ}) (Sr)$$

$$= 2 a_{\sigma} (Ca) + a_{\sigma} (Sr).$$
(I-42)

The values of the shielding tensor components σ_{11} , σ_{22} , σ_{33} for the peak at 79 ppm (configuration II in Fig. I-16) obtained using the a_{σ} and a_{π} values in Table 4 are equal to 160.9 ppm, 175.4 ppm and 261.0 ppm respectively. The CSA and asymmetry parameter of the 79.6 ppm peak calculated using Eqs. I-8 and I-9 are 92.9 ppm and 0.23, and the CSA and asymmetry parameter of the 64 ppm peak (calcium fluorapatite) are 84 ppm and 0.12 The calculated energy modulations of the 64 ppm and 79.6 ppm peaks during one rotor cycle spinning for two different crystallite orientations are shown in Fig. I-18. Fig. I-18a shows the existence of an overlap of the energy levels between the peaks corresponding to configurations I and II in Fig. I-16 during one rotor cycle, whereas the different crystallite orientations of Fig. I-18b do not. From our calculations (not shown here), most crystallite orientations of configurations I and II have an energy overlap during one rotor cycle. Therefore, a powder sample of (Ca_{8.97}Sr_{1.03}F₂(PO₄)₆) will have most crystallites experiencing level-crossing under MAS, resulting in the observed spin diffusion between the 79.6 ppm and 64 ppm peaks. This spin diffusion takes place through the ¹⁹F homonuclear dipolar interaction. This spin diffusion between the 79.6 ppm and 64 ppm peaks in Fig. I-12 indicates that the corresponding fluoride ions are close to each other and have equivalent chemical shifts during the rotor cycle.

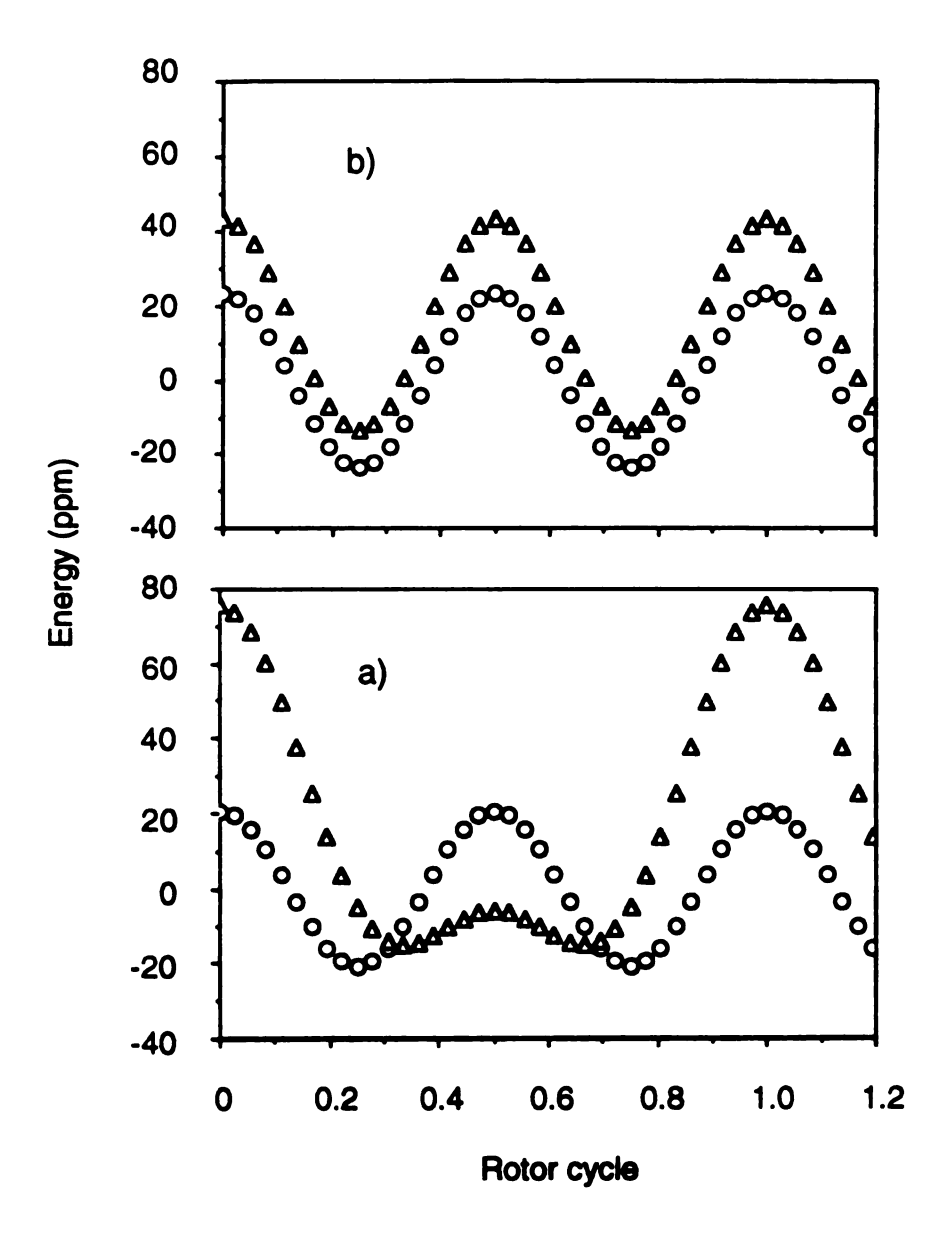


Figure I-18. Variation in the instantaneous chemical shifts during a rotor cycle of the 64 ppm and 79 ppm peaks of the $Ca_{8.97}Sr_{1.03}F_2(PO_4)_6$ solid solution under MAS for at the different crystallite orientations, $\alpha = 0^\circ$ and $\beta = 60^\circ$ (a), and $\alpha = 0^\circ$ and $\beta = 90^\circ$ (b): 64 ppm peak (open triangles) and 79 ppm peak (open circles). α and β are Euler angles with respect to the principal axis system of tensors in the rotor frame.

8. Conclusions

We have obtained the values of the CSA for $M_5F(PO_4)_3$ (M = Ca, Sr, and Ba) using the different methods. Even though the measured asymmetry parameter η of $Ca_5F(PO_4)_3$ obtained by using the moments method and the Herzfeld and Berger graphical method is not equal to zero, the value of the CSA of $Ca_5F(PO_4)_3$ obtained from ^{19}F MAS-NMR spectra by the two methods is close to that obtained from a ^{19}F single crystal NMR study. 12 The accuracy of measuring the CSA of $M_5F(PO_4)_3$ from the moments remains the same for different spinning speeds. The simulations using ANTIOPE show that the change of the CSA of $Ca_5F(PO_4)_3$ due to the dipolar interaction is small. The change in the intensity of the centerband and sidebands when the dipolar interaction is considered causes a failure of the Herzfeld-Berger contour plots of $Ca_5F(PO_4)_3$ and $Ca_5F(PO_4)_3$ to overlap at spinning speed below 9kHz. However, since the CSA values obtained from the contour plots using high spinning speed data are close to the CSA values measured from the moments method, the two methods are complementary under these conditions.

There are two reasons that the intensities of the simulated spectra of $M_5F(PO_4)_3$ (M = Ca, Sr, and Ba) do not correspond to those of the experimental spectra. One reason is that dipolar interaction is neglected in the VNMR 3.2 simulations. The other reason is that the different half-height linewidths of the peaks can give rise to a difference between real and simulated spectra. The stick spectra obtained from the integrated intensities of peaks are therefore more useful for comparing the simulated and experimental spectra.

The separation of the a_{σ} and a_{π} parameters for from the chemical shift tensors gives information about the contribution of the sigma- and pi-bonding components

of the chemical bonding between alkaline-earth metal ions and fluoride ions to the 19 F shielding in apatite samples. The values of a_{σ} and a_{π} obtained from 19 F shielding tensors for apatite samples make it possible to predict the CSA and asymmetry parameter η of configurations in the solid solutions of Ca/Sr fluorapatite and the orientation of the shielding tensor in the molecular frame. This somewhat novel approach to predicting the full shielding tensor in the molecular frame of solid solution has proven valuable in studies of chemical-shift-selective MQ-NMR, 34 and may be useful in studying other solid solutions.

The shifts of the peaks in the ¹⁹F MAS-NMR spectrum of the solid solution Ca_{8.97}Sr_{1.03}F₂(PO₄)₆ were interpreted in terms of proximity of the fluorine spins to strontium ions. The fact that the peaks of this spectrum arose from fluorine spins in the same phase was established by demonstrating the existence of spin diffusion between them with the SPARTAN pulse sequence. The preference of Sr²⁺ ions for the Ca(2) sites in Ca_{8.97}Sr_{1.03}F₂(PO₄)₆ was also studied. The observed 23 % preference of Sr²⁺ ions for Ca(2) sites, using two different methods is in agreement with an X-ray powder diffraction study of Ca/Sr hydroxyapatites, which determined an approximately a 20 % site preference for Ca(2) site.³⁵ A more recent EXAFS study of Ca/Sr hydroxyapatite claimed a larger preference for the Ca(2) site, and must be considered suspect.

9. References

- M. Mehring, A. Pine, W-K. Rhim, and J. S. Waugh, J. Chem. Phys. 54, 3239 (1971).
- R. W. Vaughan, D. D. Elleman, W-K. Rhim, and L. M. Stacey, *J. Chem. Phys.* 57, 5383 (1972).
- 3. R. J. Sears, J. Chem. Phys. 59, 5213 (1973).
- 4. R. J. Sears, J. Chem. Phys. 61, 4368 (1974).
- 5. J. Mason, J. C. S. Dalton, 1426 (1975).
- 6. J. P. Yesinowski and M. J. Mobley, J. Am. Chem. Soc. 105, 6191 (1983).
- 7. A. T. Kreinbrink., C. D. Sazavsky, J. W. Pyrz, D. G. A. Nelson, and R. S. Honkonen, *J. Magn. Reson.* **88**, 267 (1990).
- 8. K. A. Smith and D. P. Burum, J. Magn. Reson. 84, 85 (1989)
- 9. K. Sudarsanan, P. E. Mackie, and R. A. Young, *Res. Bull.* 7, 1331 (1972)
- 10. K. Sudarsanan and R. A. Young, *Acta Cryst.* **B28**, 3668 (1972)
- 11. M. Mathew, I. Mayer, B. Dickens, and L. W. Schroeder, J. Solid State Chem. 28,79 (1979).
- 12. J. L. Carolan, Chem. Phys. Lett. 12, 389 (1971).
- 13. A.M. Vakhrameev, S. P. Gabuda, and R. G. Knubovet, *J. Struct. Chem.* (USSR),19, 256 (1978).
- 14. M. M. Maricq and J. S. Waugh, J. Chem. Phys. 70(7), 3300 (1979).
- 15. J. Herzfeld and A. E. Berger, J. Chem. Phys. 73(12), 6021 (1980).
- R. Tycko, G. Dabbagh, S. R. Kurtz, and J. P. Goral, *Phys. Rev. B.* 45, 13452 (1991).
- 17. E. R. Andrew, A. Bradbury, and R. G. Eades, *Nature (London)*, **183** 1802 (1959).

- 18. I. J. Lowe, Phys. Rev. Lett. 2, 285 (1959).
- 19. E. R. Andrew, Prog. Nucl. Magn. Reson. Spectrosc. 8, 1 (1972)
- 20. L. B. Moran, J. K. Berkowitz, and J. P. Yesinowski, *Phys. Rev. B* **45**, 5347 (1992).
- G. Bodenhausen, R. Freeman, and G. A. Morrison, *J. Magn. Reson.* 23, 171 (1976); G. A. Morrison and R. Freeman, *J. Magn. Reson.* 29, 433 (1978).
- 22. A. Kubo and Charles A. McDowell, *J. Chem. Soc. Faraday. Trans.* **84**, 3713 (1988).
- 23. F. S. de Bouregas and J. S. Waugh, *J. Magn. Reson.* **96**, 280 (1992).
- 24. E. Brunner, D. Freude, B. C. Gerstein, and H. Pfeifer, J. Magn. Reson. 90, 90(1990).
- 25. N. J. Clayden, C. M. Dobson, L. Lian, and D. J. Smith, *J. Magn. Reson.* **69**, 476 (1986).
- 26. N. F. Ramsey, *Phys. Rev.* **78**, 699 (1950)
- 27. N. F. Ramsey, *Phys. Rev.* **86**, 243 (1951)
- 28. W. E. Lamb, *Phys. Rev.*, **60**, 817 (1941).
- 29. Y. V. Gagarinskii and S. P. Gabuda, translated from Zhurnal Strukturnoi Khimii, 11(5), 955 (1970).
- 30. N. Bloembergen, *Physica* **15**, 386 (1949).
- 31. A. Abragam, The Principles of Nuclear Magnetism (Oxford University Press, London, 1961), Chaps. V. and IX.
- 32. E.T. Olejniczak, S.Vega, and R. G. Griffin, J. Chem. Phys. 81, 4804 (1984).
- 33. D.P. Raleigh, E.T. Olejniczak, and R. G. Griffin, *J. Chem. Phys.* **89**, 1333 (1988).
- 34. L. B. Moran and J. P. Yesinowski, to be published.

35. H. J. M. Heijigers, F. C. M. Driessen, and R. M. H. Verbeeck, *Calcif Tissue Int.* **29**, 127 (1979).

PART 2

¹H and ¹⁹F Multiple-Quantum NMR Dynamics of Quasi-One-Dimensional Spin Distributions in Apatites

1. Introduction

Multiple-quantum NMR is a general term for experiments that observe nuclear magnetic transitions forbidden by the standard selection rule $\Delta m = \pm 1$. Although multiple quantum transitions can be observed by using high power continuous-wave (CW) spectrometers,¹⁻¹⁴ difficulties of interpretation and inconvenient instrumental requirements have limited the use of CW-observation of multiple-quantum transitions. The advent of time-domain Fourier transform techniques¹⁵ made it possible to detect the forbidden transitions. In the mid 1970s, Hashi¹⁶ and Ernst¹⁷ independently adapted a two-dimensional Fourier transform NMR technique to indirectly observe multiple quantum transitions.

Since that time, the multiple quantum NMR technique has been mostly applied to the liquid state, where the size of the spin systems is relatively small. ¹⁸⁻²⁸ An 8-pulse sequence that creates an average-Hamiltonian operator for double quantum NMR transitions of dipolar-coupled spin pairs, ²⁹ combined with the use of a time-reversal pulse sequence, ³⁰ increases the S:N ratio of multiple-quantum intensities and has made the study of larger spin systems such as found in solids feasible. ¹H MQ-NMR has been applied to the study of proton distributions in solids, ^{31,32-36} imaging in solids, ^{32,37} and adsorption of organic molecules in zeolites^{38,39}. ¹H MQ-NMR has been also used to study nematic liquid crystals. ^{28,40-43} ¹⁹F MQ-NMR has been used to investigate fluorine distributions in polycrystalline⁴⁴ and photosensitive salts. ⁴⁵

The time-development of multiple-quantum coherences in the "infinite" dipolar-coupled spin systems typical of many solids presents both a lure and a challenge. The lure is the possibility of obtaining structural information about groups of correlated spins that would be otherwise unobtainable with conventional NMR spec-

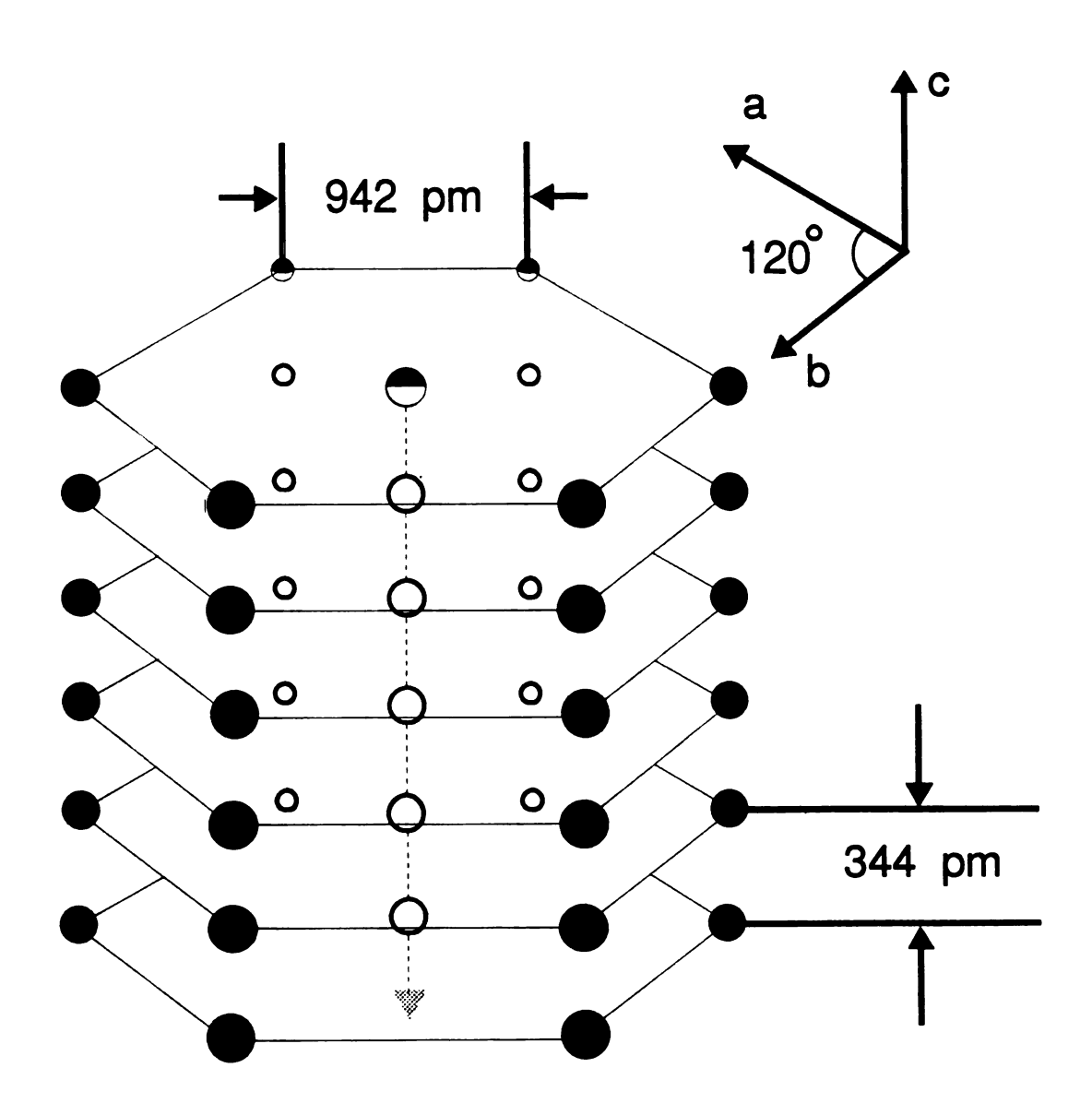
troscopic techniques. The challenge resides in the development of theoretical models describing multiple-quantum dynamics that are both computationally practical and experimentally realistic. The explicit calculation of the density-operator for spin systems, widely used to describe modern NMR experiments, 46-48 cannot describe many actual spin systems due to computational limitations (up to nine spins is the current limit). 49-51 The actual spin systems present in strongly dipolar-coupled solids consist of about 1020 spins whose calculation time using the density matrix is prohibitive. Therefore, simplifying approaches have been developed that make only statistical assumptions about the time-development of the density operator, and neglect the detailed spin-dynamics arising from the specific disposition of spins in space. 52,53 The earliest of these, the statistical model.⁵⁴ counts the combinatorial possibilities of having coherences of order n ("n-quantum coherences") in a spin system of "effective size" N. For an "infinite" spin system, the effective size N increases monotonically with increasing preparation time allowed for creation of multiple-quantum coherences. The statistical model predicts an approximately Gaussian distribution of intensities for the various orders of multiple-quantum coherence. Although it tends to underestimate the intensity of high order coherences, it does provide a measure of the effective size of the spin system at a given preparation time. 31,52,53,55,56 Since intermolecular dipolar couplings of nematic liquid crystals are averaged to zero whereas intramolecular dipolar couplings are not, "spin counting" by means of MQ-NMR experiments of the known number of spins in molecules of nematic liquid crystals demonstrates the usefulness of the statistical model. 43,55 The directed walk through Liouville space ("hopping") model⁵⁷ predicts the intensities of various orders of higher order coherences, at different preparation times, by counting the

combinatorial possibilities of allowed "transitions" or "hops" in Liouville space, and assuming that any oscillatory behavior will be hidden by destructive interference and resultant decay. Although the hopping model can successfully account for features of the experimental data.⁵⁷ Lacelle⁵³ has pointed out aspects of the averaging of multiplicative processes that, if properly taken into account, may lead to significant differences from the predictions of the hopping model. Only very recently has there been an attempt to develop a simplifying model, as opposed to explicit density operator calculations. 50,51 that specifically considers the spatial structure of the spin system (including its dimensionality). This "incremental shell" model of Levy and Gleason³⁶ describes multiple quantum dynamics during the preparation period as a stepwise process: a given coherence can either expand by incorporating one additional spin at the periphery of the spin cluster involved in the coherence, or decrease in size by one spin. The rate of this process is governed by the dipolar coupling between these neighboring spins and by structure-dependent parameters. A set of differential equations for "average" product operators of the density operator can then be solved numerically to yield the effective size N vs. preparation time. Clear distinctions between the dynamics of two- and three-dimensional spin systems are both predicted and observed experimentally.³⁶ A number of three-dimensional solids have been recently observed to exhibit a universal growth behavior (when the time axis is scaled by the strength of the square root of the second moments)³⁶ that can be fit to theoretical predictions of an "incremental shell model; " the effective size increases as the cube (or third power) of the preparation time. In case of a presumed surface film of protons, the experimental results could be fit to the model with an approximately quadratic dependence of the effective size upon preparation time, as predicted for a two-dimensional spin distribution.³⁶ An infinite one-dimensional distribution of uniformly-spaced spins would be expected to provide the simplest experimental test of the various models. We report here results for a close approximation to such a spin system: the ¹H nuclei of hydroxyapatite, Ca₅(OH)(PO₄)₃. Since the multiple-quantum coherences are created by homonuclear dipolar couplings, we need only consider the hydroxyl protons (or fluoride ions) in the structure of hydroxyapatite (or fluorapatite). Figure II-1 shows the basic idealized geometry of the ¹H spin system of hydroxyapatite: infinite linear chains of protons having a uniform spacing of 344 pm, with each chain surrounded by six other chains at a distance of 942 pm.^{58,59} The largest intra-chain dipolar coupling is some 20 times greater than the largest inter-chain dipolar coupling, and should dominate the multiple-quantum dynamics. The weak heteronuclear dipolar couplings to the ³¹P nuclei (<2 kHz) can safely be ignored.⁴⁴

In order to use apatites as a model for studying one-dimensional MQ dynamics, one must have knowledge about the occurrence of interruptions in the 1-D chain, due to either vacancies or substitutions (collectively referred to here as "defects"). Such defects are commonly present at significant levels in both synthetic as well as naturally-occuring apatites. The ability to obtain such information about defects in apatites from MQ NMR experiments would thus provide a useful method for investigating such systems, in addition to better defining the degree of ideality of one-dimensional spin systems in powders and single crystals.

In this study we present experimental results on proton MQ NMR dynamics in a stoichiometric hydroxyapatite sample (HAP-M), a hydroxyapatite sample containing defects (HAP-N), and a series of fluorohydroxyapatite solid solutions, $Ca_5(OH)_{(1-x)}F_x(PO_4)_3$, with the fluoride ion (replacing a hydroxyl group) forming

Figure II-1. Schematic idealized arrangement of linear columns of protons (black circles) in calcium hydroxyapatite ($Ca_5OH(PO_4)_3$). The central column is surrounded by six neighboring columns. The distance between columns is 942 pm and the distance between intra-chain protons is 344pm. The position of protons in four of the six neighboring columns is actually approximately 260pm below the black circles in the monoclinic form, which exists only for very stoichiometric samples. In the more commonly-occurring hexagonal form, the protons in three of the six neighboring columns are located about 260pm below the black circles due to statistical disorder. The geometry of the fluorine atoms in fluorapatite ($Ca_5F(PO_4)_3$) is similar to the arrangement of protons in hydroxyapatite, with a distance between columns of 937pm and an identical intra-chain distance.



a defect in the 1-D chain of spins. We model these results for a hydroxyapatite sample with a slight hydroxyl deficiency in terms of a 1-D cluster model described in the Discussion section. The 1-D cluster model considers randomly-distributed defects in apatites as producing a distribution of 1-D clusters of varying lengths, and uses the MQ response of a stoichiometric hydroxyapatite sample as a "calibration". In addition, we report ¹⁹F MQ NMR data on a single crystal of mineral fluorapatite at several orientations in the magnetic field, thereby scaling the dipolar interactions within the chains by a known amount. This approach, when applied to a sample containing few defects, should eventually allow one to scale the relative contributions of one-dimensional and higher-dimensional MQ growth, and thus permit better isolation of the effects of differing dimensionality.

2. Multiple-Quantum NMR Dynamics

A. Density Operator Description of Multiple-Quantum NMR Dynamics

The description of NMR experiments can be started by first considering simple two level systems. An isolated spin-1/2 particle in an external magnetic field has the two eigenstates $|\frac{1}{2}\rangle$ and $|-\frac{1}{2}\rangle$, which represent the two allowed orientations of its angular momentum.^{47,60} The state vector, a superposition of these basis states, is given by a linear combination of these two states

$$|\psi(t)\rangle = c_{1/2}(t)|\frac{1}{2}\rangle + c_{-1/2}(t)|-\frac{1}{2}\rangle$$
 (II-1)

where $c_{1/2}(t)$ and $c_{-1/2}(t)$ are the (in general) time-dependent complex coefficients. The state of the system can be described by the values of $c_{1/2}(t)$ and $c_{-1/2}(t)$, which are solved by using the time-dependent Schroedinger equation

$$\frac{d}{dt}|\psi(t)\rangle = -i\mathcal{H}|\psi(t)\rangle. \tag{II-2}$$

When the only Hamiltonian is the Zeeman Hamiltonian, the time-dependent coef-

ficients are given by

$$c_{1/2}(t) = a \cdot exp(i\alpha)exp(-i\omega_0 t)$$
 (II-3a)

$$c_{-1/2}(t) = b \cdot exp(i\beta) exp(i\omega_0 t)$$
 (II-3b)

where $a^2+b^2=1$, and α and β are real numbers representing phases.⁴⁷ The expectation value of any observable can be calculated from $|\psi(t)\rangle$. Expectation values of the three components of magnetic moment are represented by

$$\mu_x(t) = \langle \psi(t) | \gamma \hbar I_x | \psi(t) \rangle$$
 (II-4a)

$$\mu_{\mathbf{y}}(t) = \langle \psi(t) | \gamma \hbar I_{\mathbf{y}} | \psi(t) \rangle$$
 (II-4b)

$$\mu_z(t) = \langle \psi(t) | \gamma \hbar I_z | \psi(t) \rangle$$
 (II-4c)

which are solved by using the raising and lowering operators defined by

$$I_{\pm} = \sqrt{I(I+1) - m(m\pm 1)} | m\pm 1 \rangle.$$
 (II-5)

The result is

$$\mu_x(t) = \gamma \hbar ab \cos(\alpha - \beta + \omega_0 t)$$
 (II-6a)

$$\mu_y(t) = \gamma \hbar a b \sin{(\alpha - \beta + \omega_0 t)}$$
 (II-6b)

$$\mu_z(t) = \gamma \hbar (a^2 - b^2)/2. \tag{II-6c}$$

The expectation values of the magnetic moments of transverse components for an individual spin precess about the external magnetic field with angular frequency ω_0 and phase $\alpha-\beta$. However, the expectation value of the magnetic moment of the z component is constant, and, (at equilibrium) is proportional to a population difference of the two spin levels, which in turn is proportional to the energy difference in the "high temperature approximation" (Boltzmann distribution). Since the behavior of a single spin or group of spins cannot in general describe a macroscopic system, we introduce an ensemble of independent two-level subsystems. Figure II-2 shows the mixed and pure states of this ensemble. The transverse components of the subsystems have the same frequency, but need not have the same

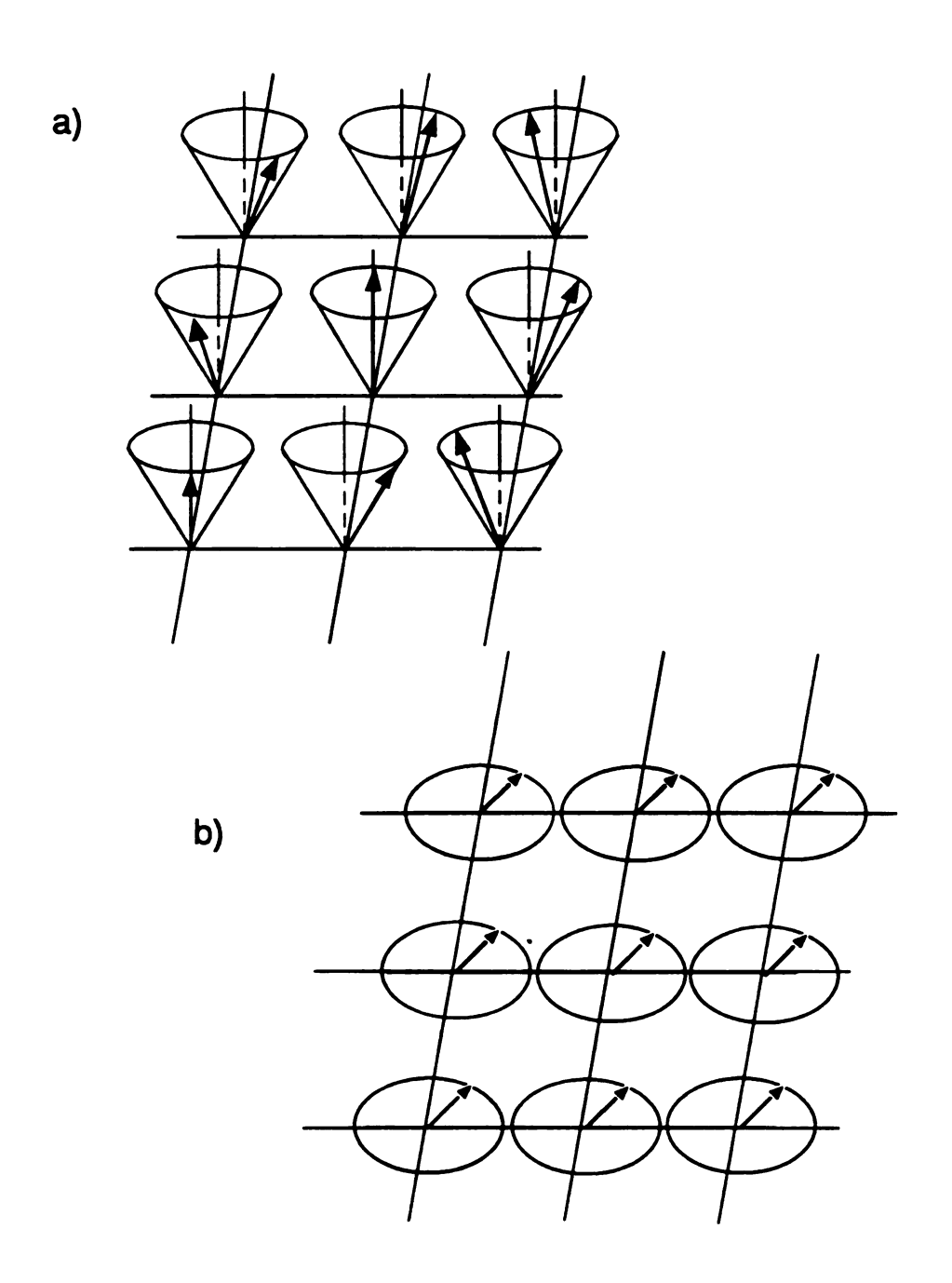


Figure II-2. Random phases (a) and correlated phases (b) in an ensemble of two level systems. Taken from Ref. 61.

phase for a the mixed state (Fig. II-2a). The average transverse components of the subsystems over all values of the phase is equal to zero, and only the longitudinal component remains (see equation II-6). In a pure state (Fig. II-2b), the behavior of the macroscopic system is identical to that of each microscopic subsystem, due to each subsystem having the same frequency and phase (phase coherence).^{47,61} The term "coherence" is defined as the presence of some degree of phase coherence between the basis states of the isolated subsystems throughout the ensemble.⁶¹

An ensemble of spins can be described by the density operator, which is represented by

$$\rho = \sum p_i |\psi_i\rangle \langle \psi_i| = \overline{|\psi\rangle \langle \psi|}. \tag{II-7}$$

where p_i is the probability of each state ψ_i occurring in the superposition.⁶² The equilibrium density operator can be represented by the $|M_r\rangle\langle M_s|$ basis whose matrix formulation of Eq. II-2 is given by

$$\rho = \left[\frac{\overline{c_{1/2}^* c_{1/2}}}{c_{1/2}^* c_{-1/2}^*} \quad \frac{\overline{c_{1/2} c_{-1/2}^*}}{c_{-1/2}^* c_{-1/2}^*} \right]. \tag{II-8}$$

With the probabilities from the Boltzmann factor

$$p(M = \pm \frac{1}{2}) = exp(-M\hbar\omega_0/kT)/Z, \tag{II-9}$$

the equilibrium density operator is given by

$$\rho_{eq} = exp(-\hbar\omega_0 I_z/kT)/Z \tag{II-10}$$

after averaging over the phase differences. From the high temperature approximation, the partition function Z is equal to 2I + 1. For the equilibrium density operator of a spin 1/2 system, Eq. II-3 can be rewritten as

$$[\rho_{ij}] = \begin{bmatrix} exp(-\hbar\omega_0/2kT)/2 & 0\\ 0 & exp(-\hbar\omega_0/2kT)/2 \end{bmatrix}.$$
 (II-11)

The random phase among spins of different subsystems in the ensemble averages the off-diagonal elements to zero, but an application of an appropriate rf pulse to the ensemble results in non-zero off-diagonal elements in the matrix. The existence of the non-zero off-diagonal elements from a single pulse is described as single-quantum coherence. The order n of a coherence between states $|r\rangle$ and $|s\rangle$ is defined as

$$n = \Delta M = |M_r - M_s|, \tag{II-12}$$

where M_r represent the total (summed) M_z values of all the spins in the state $|r\rangle$. The dimension of the density matrix increases as size of the coupled spin system increases. The presence of phase coherences in large spin systems produced by a proper pulse sequence results in non-zero off-diagonal elements that represent the multiple quantum coherences between states.

B. Time Development of the Density Operator in the Rotating Frame

The density operator determines the state of a system at any time. The development of the density operator ρ is governed by the Liouville-von Neumann equation

$$\frac{d\rho}{dt} = i[\rho, \mathcal{H}]. \tag{II-13}$$

When the Hamiltonian ${\cal H}$ is time-independent, the formal solution of Eq. II-13 is represented by

$$\rho(t) = \exp[-(i/\hbar)\mathcal{H}t]\rho(0)\exp[(i/\hbar)\mathcal{H}t]. \tag{II-14}$$

When ρ and $\mathcal H$ commute, no evolution of the density operator occurs

$$\rho(t) = \rho(0) \exp[-(\mathrm{i}/\hbar)\mathcal{H}t] \exp[(\mathrm{i}/\hbar)\mathcal{H}t] = \rho(0). \tag{II-15}$$

If \mathcal{H} depends explicitly on time, we may satisfy both the Schroedinger equation and the Liouville-von Neumann equation by replacing the propagator that makes the evolution of one state to other state by a unitary transformation in Eq. II-13 with

$$U(t) = Texp\left[-i\int_{0}^{t} \mathcal{H}(t') dt'\right]$$
 (II-16)

where T is the Dyson "time-ordering operator". Coherent averaging theory 63,64 is

used to solve Eq. 15. $\rho(t)$ is always related to $\rho(0)$ by a unitary transformation in Liouville space so that the length of the vector representing the density operator remains constant as the system evolves. Since the expectation value of any operator can be calculated from ρ ,⁴⁷

$$\langle A(t) \rangle = \sum_{ij} \rho_{ij} A_{ij} = Tr[\rho(t)A]$$
 (II-17)

the prediction and control of the time development of ρ are always central problems for time domain NMR in general and multiple-quantum NMR in particular.

It is often convenient to go to the rotating frame when a system is acted on by alternating magnetic fields. The transformation to a frame rotating at or near the Larmor frequency in order to remove the fast precession due to the Zeeman interaction makes the solution of the Liouville-von Neumann equation easier. Defining an operator R as

$$R = \exp(-i\mathcal{H}_{ext}t) \tag{II-18}$$

where H_{ext} is the external Hamiltonian. We write the transformed density operator as

$$\rho^{\mathbf{R}} = \mathbf{R}^{-1}\rho\mathbf{R}; \tag{II-19}$$

and the transformed Hamiltonian as

$$\mathcal{H}^{R} = R^{-1}\mathcal{H}R - iR^{-1}\frac{dR}{dt}$$
 (II-20)

The transformed Liouville-von Neumann equation can be rewritten as

$$\frac{d\rho^{R}}{dt} = i\left[\rho^{R}, \mathcal{H}^{R}\right] \tag{II-21}$$

Since the Liouville-von Neumann equation is of the same form after the transformation, we will omit the superscript on ρ and \mathcal{H} with the understanding that the laboratory frame has been replaced by a suitable rotating frame in which external Zeeman interactions are absent.

C. Pulse Sequence for Multiple-Quantum NMR

Since multiple-quantum transitions are usually not directly observable with an NMR coil, they must be detected indirectly by two-dimensional spectroscopic methods. The general scheme of a two-dimensional multiple-quantum NMR experiment is shown in Figure II-3. The pulse sequence creates a non-equilibrium condition of multiple quantum coherence during a preparation period τ , allows the coherence to respond during an evolution period t_1 and then transfers the coherence to z magnetization during a mixing time τ' . The coherence is then detected after a detection pulse during the detection period, which creates observable I_z magnetization (corresponding to a single-quantum coherence).

The preparation period propagator

$$U(\tau) = \exp(-iHt) \tag{II-22}$$

arises from a combination of pulses and proper delays. Under this propagator, the density operator becomes

$$\rho(\tau) = \mathbf{U}(\tau)\rho(0)\mathbf{U}^{-1}(\tau) \tag{II-23}$$

by the end of the preparation period. The system is allowed to develop, freely or otherwise, for an evolution period of length t_1 . During this time, the different modes of coherence oscillate at the eigenfrequencies determined by the effective Hamiltonian H_1 (defining in Figure II-3). No signal is recorded during this interval. After time development is halted at some time t_1 , the coherences are transferred to detectable single-quantum modes during the mixing and detection periods and the density operator becomes

$$\rho\left(\tau, t_1 \tau'\right) = V\left(\tau'\right) \exp(-iH_1 t_1) \rho(\tau) \exp(iH_1 t_1) V^{-1}\left(\tau'\right)$$
(II-24)

where $V\left(\tau'\right)=\exp\left(-iH'\tau'\right)$ is the mixing period propagator. Transverse components of the total spin angular momentum I_x and I_y are obtained immediately

	Preparation	Evolution	Mixing	Detection
Propagator	U	exp(-H ₁ t ₁)	V	exp(-H ₂ t ₂)
Time variable	τ	t ₁	τ'	t ₂

Figure II-3. General form of the pulse sequence of MQ NMR experiments. See text.

after the mixing period

$$S_{\alpha}\left(\tau,t_{1},\tau'\right)=Tr\left[
ho\left(\tau,t_{1},\tau'\right)I_{\alpha}\right] \qquad \alpha=x,\ y.$$
 (II-25)

In NMR experiments, a complex signal $S = S_x + iS_y$ is detected with the combination of the transverse components in quadrature. From the high temperature approximation, a reduced density matrix describing the initial equilibrium condition of the spin system is represented by

$$\rho \sim I_z.$$

Even though the initial condition I_z is not measurable directly, it is related to I_x and I_y by a simple 90° pulse. Thus we take I_z as the observable operator. Defining the coherence amplitude

$$Z_{rssr} = \langle M_r | U \rho(0) U^{-1} | M_s \rangle \langle M_s | V^{-1} I_z V | M_r \rangle$$
 (II-27)

we then express the trace as

$$S_z\left(\tau, t_1, \tau'\right) = \sum_{r,s} Z_{rssr} \exp\left(-i\omega_{rs}^{(1)} t_1\right)$$
 (II-28)

where the oscillation frequency $\omega_{rs}^{(1)} = \omega_r - \omega_s$ occur at the energy level differences during the evolution period Hamiltonian. The full response during the evolution period is recorded point-by-point by repetition of the experiment over a series of regularly incremented values of t_1 . The signal detected during t_2 shows the modulation of the single-quantum signal with respect to the t_1 domain. Fourier transformation of the interferogram of the t_1 time-domain provides the multiple-quantum spectrum.

In general the amplitude and the phase of each frequency component at $t_2 = 0$ depend on the combined effects of preparation and mixing through the complex factor Z. When U is equal to or is only different from V^{-1} by a phase factor ϕ ,

$$V^{-1} = \exp(-i\phi I_z) U \exp(i\phi I_z)$$
 (II-29)

the signal in Eq. 27 becomes

$$S_{z}(\tau, t_{1}) = \sum_{n} \sum_{r,s} \langle M_{r} | I_{z} | M_{s} \rangle^{2} \exp(in\phi) \exp\left(-i\omega_{rs}^{(1)} t_{I}\right)$$
 (II-30)

where all transitions within a given order n have the same phase, and all transitions of two adjacent orders differ in phase by $\pm \phi$. The signal is detected by using a simple $\pi/2$ pulse at $t_2=0$. The condition that the preparation and mixing Hamiltonians be equal in magnitude but opposite in sign, results in time reversal for the propagator. In solids, the time reversal sequences that refocus the evolution due to dipolar coupling increase the signal to noise ratio by achieving a constructive interference of the different transitions within an order.²⁹

Multiple-quantum coherences can be created in dipolar-coupled solids under the action of rf pulse sequences with an appropriate average Hamiltonian. Figure II-4 shows a pulse sequence for multiple-quantum NMR experiments. Eight 90° pulses of duration t_p with spacings $\Delta' = 2\Delta + t_p$ generate the average dipolar Hamiltonian

$$\mathcal{H}_D = \mathcal{H}_{yz} = -\frac{1}{2} \sum_{j \le k} D_{jk} (I_{j+} I_{k+} + I_{j-} I_{k-})$$
 (II-31)

where $I_{j\pm}=I_{jx}\pm iI_{jy}$, and D_{jk} is the homonuclear dipolar coupling. The average dipolar Hamiltonian, containing only the terms $I_{j+}I_{k+}$ and $I_{j-}I_{k-}$, excites only even order multiple-quantum coherences. Two methods, time proportional phase incrementation (TPPI)²⁹ and phase incrementation (PI)⁴⁰, can be used to separate the different multiple-quantum orders. In TPPI, the overall phase ϕ of the preparation pulses is incremented in proportion to t_1

$$\Delta \phi = \Delta \omega \Delta t_1 \tag{II-32}$$

where ϕ is the phase of the rf pulses and $\Delta\omega$ is a resonance offset frequency. Substituting Eq. 31 into Eq. 29, we can rewrite Eq. 29 as

$$S_{z}(\tau, t_{1}) = \sum_{r} \sum_{s,s} \langle M_{r} | I_{z} | M_{s} \rangle^{2} \exp(in\Delta\omega \Delta t_{I}) \exp\left(-i\omega_{rs}^{(I)} t_{I}\right). \tag{II-33}$$

Fourier Transformation of the signal with respect to t₁ results in the separation of

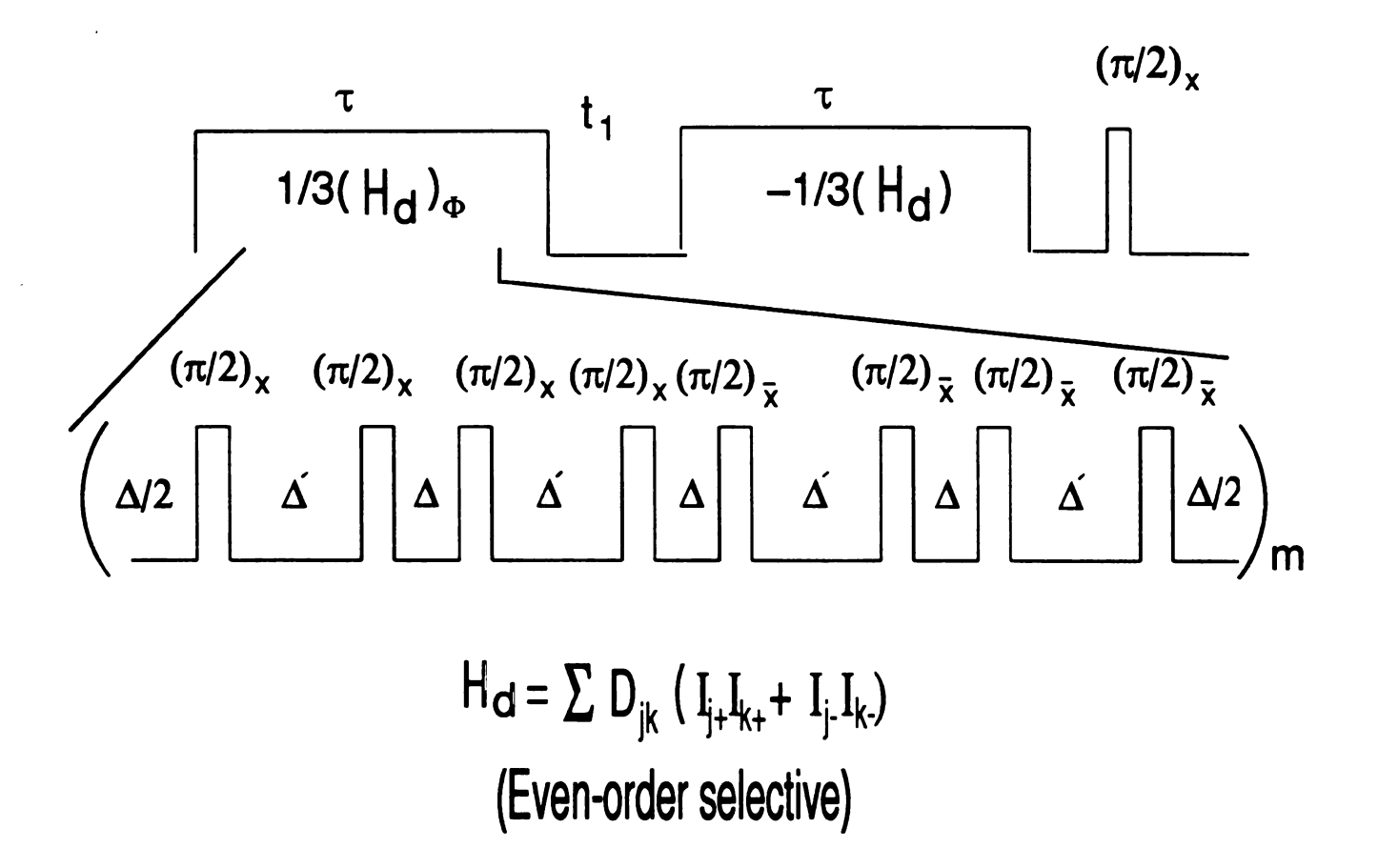


Figure II-4. Pulse sequence for multiple-quantum NMR in solids.^{29,40} The time reversal sequence is used in the mixing period. The transverse magnetization is allowed to decay during the delay before detection, and spin locking (not shown) is used after the detection pulse (final 90° pulse) to increase the S:N ratio. For PI-MQ-NMR, the value of t_1 is not stepped, but fixed at a short value, and the phase ϕ are incremented.

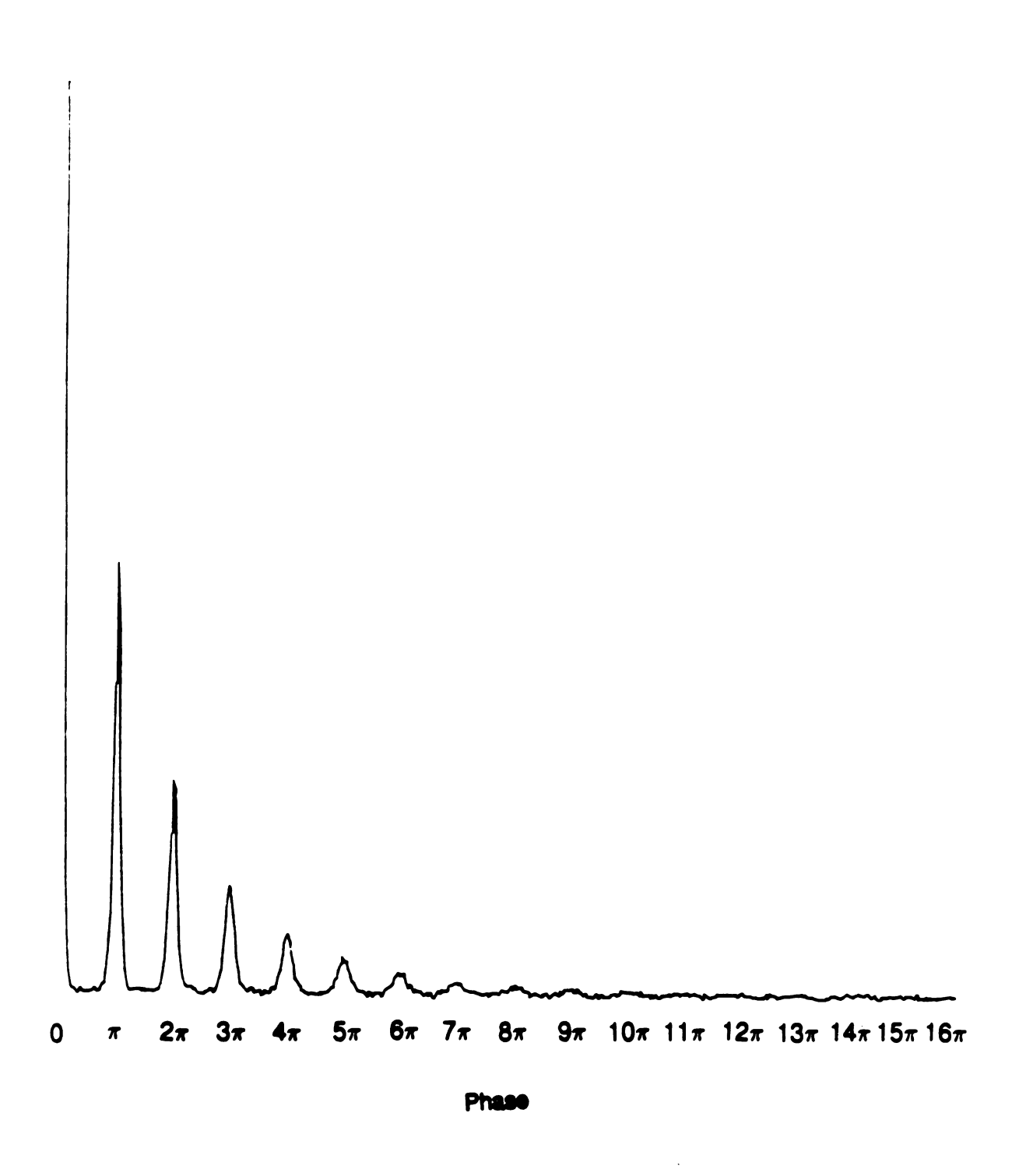


Figure II-5. Time-domain MQ interferogram of hexamethylbenzene using TPPI and the pulse sequence shown in Fig. II-4.

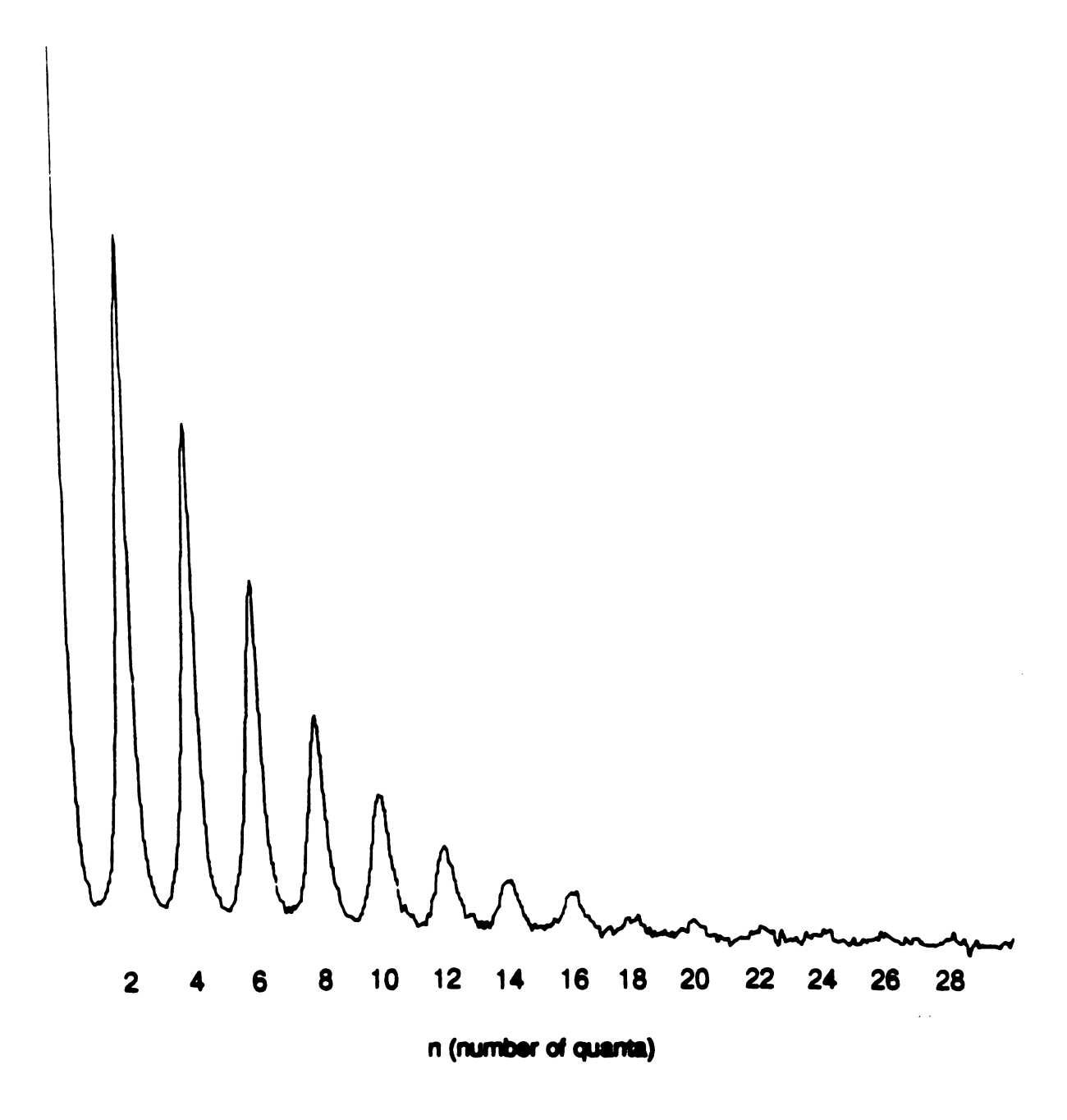
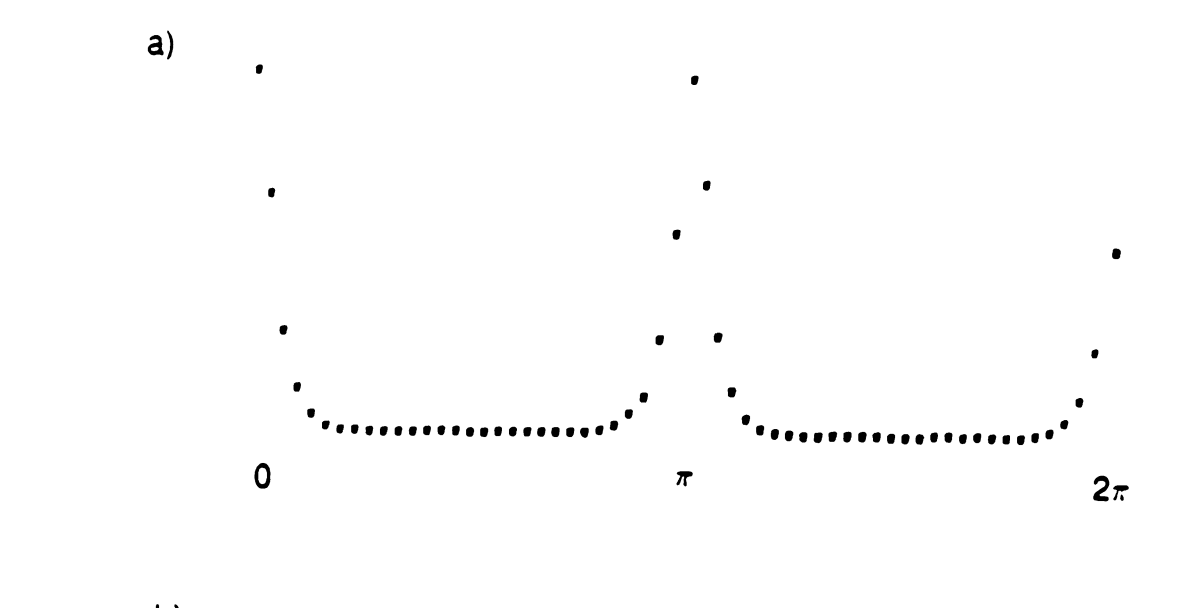


Figure II-6. Frequency-domain ¹H MQ spectrum of hexamethylbenzene using the TPPI and the pulse sequence shown in Fig. II-6. The experimental parameters used are 90° pulse length = 3.8 μ s, preparation time = 504 μ s (basic cycle time =72 μ s), Δt_1 = 200 ns and $\Delta \Phi$ = 6°.

different MQ orders by multiples of the resonance offset frequency $\Delta\omega$. The spectral width of the MQ spectrum is the inverse of the t_1 increment. The number of orders detected, n_{max} , depends on the value of the phase increment $\Delta\phi$ according to the relationship $\Delta\phi=2\pi/n_{max}$. Figure II-5 shows the time-domain MQ signal of hexamethylbenzene generated by the TPPI method. Figure II-6 shows the frequency-domain MQ spectrum of hexamethylbezene obtained using the TPPI MQ experiment. During the evolution time, the increase of t_1 duration results in a decay of the signal, which causes the frequency-domain peaks of the MQ spectrum to broaden for higher orders.

The phase-incremented MQ experiment proceeds just as described above, but since the phases of the preparation pulse are incremented by $\Delta\phi$, with a fixed evolution period, the t_1 domain MQ signal does not decay and shows periodicity (shown Fig. II-7). Fourier transformation of the time-domain MQ signal with respect to ϕ generates the series of δ -function peaks corresponding to the MQ order n. Figure II-8 shows the frequency-domain MQ signal of hexamethylbezene obtained with the phase-incremented MQ experiment.

Most MQ NMR dynamics in solids are interpreted in terms of the effective sizes that are measured from the integrated intensity of MQ orders. The spectrum from the phase-incremented method has a higher signal-to-noise ratio than that from the TPPI method, which reduces the number of transients required. The integrated intensity obtained by simply measuring the peak height also makes the data analysis simpler. Since enough digital resolution can be obtained by replicating the time-domain MQ signal from the phase-incremented method, due to the periodicity of the time-domain of MQ signal, the number of time-domain points required in the phase-incremented method is much less than that of the



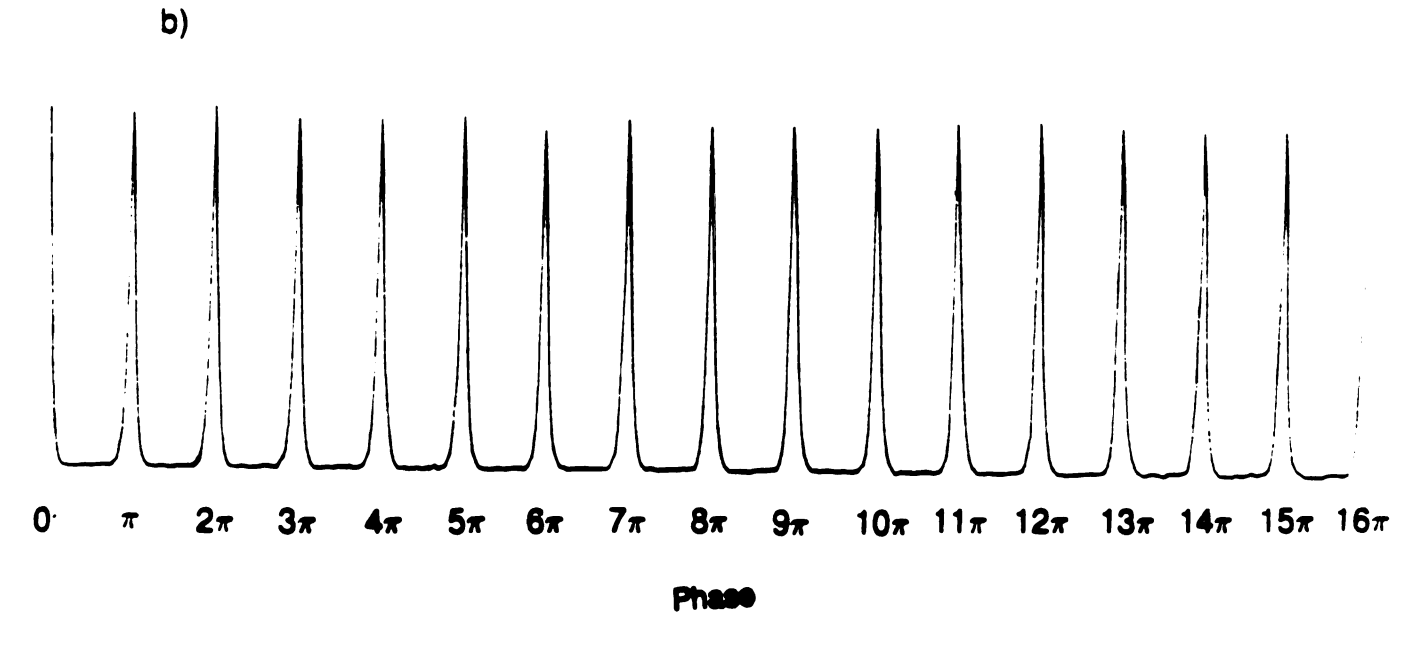


Figure II-7. Time-domain MQ interferogram of hexamethylbenzene using the phase-incremented method and the pulse sequence shown in Fig. II-6. The 60 complex points (2π) in (a) were experimentally obtained, and were replicated up to 480 complex points (16π) .

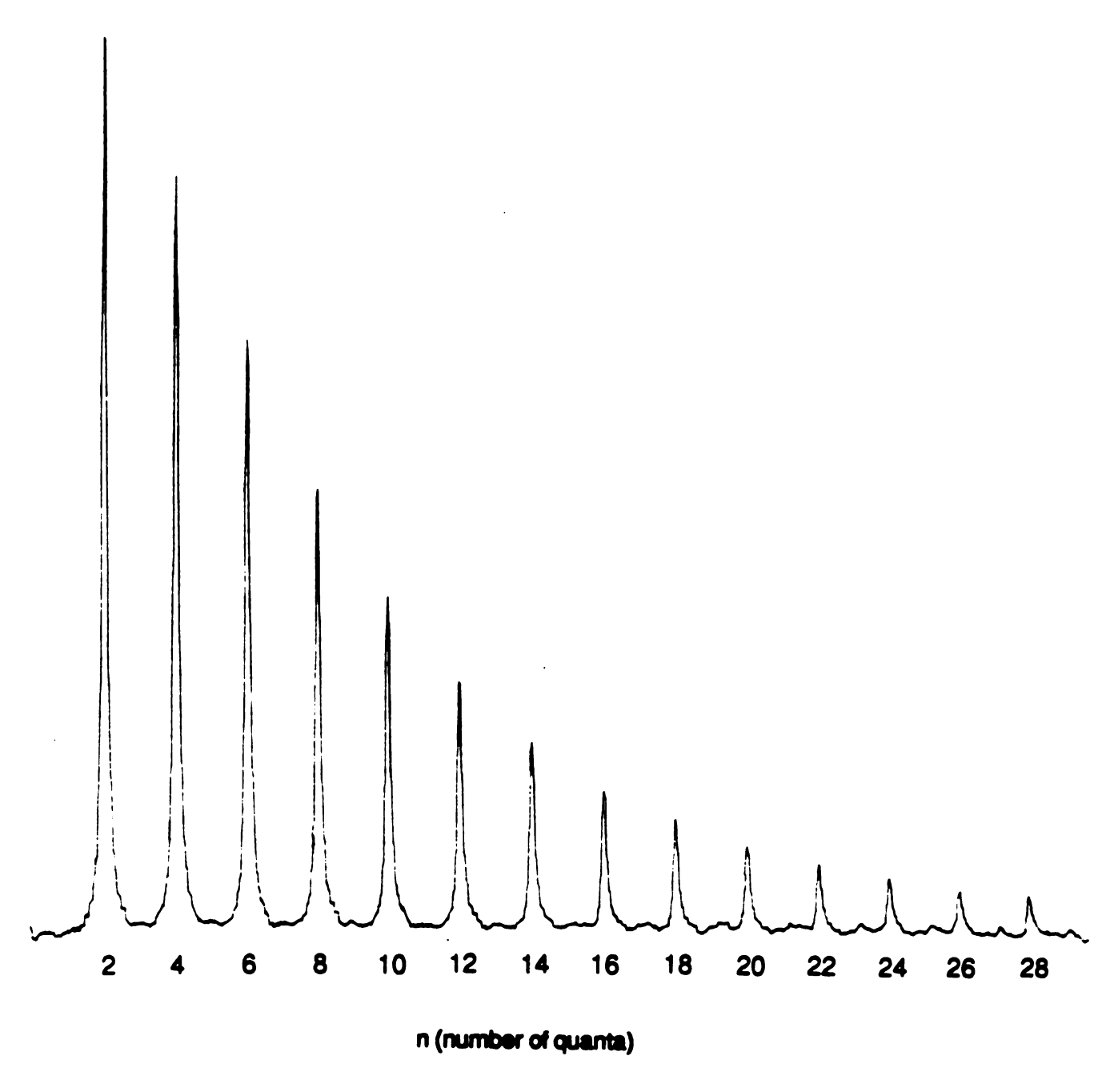


Figure II-8. Frequency-domain ¹H MQ spectrum of hexamethylbenzene using the phase-incremented method and the pulse sequence shown in Fig. II-6. All parameters are the same as in Fig. 8, except the fixed t₁ interval was set to 200 ns.

TPPI method. However, the δ -function peaks of the phase-incremented method do not yield the spectral information about the different frequencies occurring within each order.³² When only the information from the integrated intensity is needed, the phase-incremented method is preferable due to the lower time required to collect the data.

The pulse programs for the MQ pulse sequences used on the VXR 400 spectrometer were kindly provided by Dr. T. Barbara of Varian Associates. We have modified the MQ pulse sequences for our experiments, as shown in Appendix A.

D. Statistical Model of MQ Coherence Intensities

In MQ NMR experiments, the intensity of each order in the MQ spectrum depends on the number of correlated spins (effective size). The dimension of the density matrix is 2^N for an N spin-1/2 systems. The number of spins in a macroscopic sample is about 10²⁰. It is impossible to calculate the density matrix of such a macroscopic sample in solids. However, in the statistical model^{31,52,53,55,56}, we assume that the intensity of each order in a MQ spectrum is proportional to the number of possible MQ transitions, and that the transition probability of each order is the same. The effective size can be measured by counting the number of such MQ transitions.

In a strong Zeeman field, an N spin-1/2 system has 2^N stationary states, which can be classified according to the total magnetic quantum number M_z , given by

$$M_z = \sum_i m_{iz} \tag{II-34}$$

where m_{iz} is the eigenvalue ($m_{iz} = \pm 1/2$) of the *i*-th spin in the system. The energy eigenvalues of the Zeeman term are represented by (see Eq. I-3)

$$E_z = -\gamma \hbar H_0 M_z. \tag{II-35}$$

The energy levels can be sorted by the number of spins in the $|\alpha\rangle$ or $|+\frac{1}{2}\rangle$ state, n_{α} , and in the $|\beta\rangle$ or $|-\frac{1}{2}\rangle$, n_{β} state, since we can rewrite Eq. II-34 as

$$M_z = (n_\alpha - n_\beta)/2. \tag{II-36}$$

The degeneracy Ω of states having a particular energy level E_z is represented by

$$\Omega = N!/(n_{\alpha}!n_{\beta}!) \tag{II-37}$$

Substituting Eq. II-36 and, using the fact that $n_{\alpha}+n_{\beta}=N$, we can rewrite Eq. II-37 as

$$\Omega = N!/[(N/2 + M_z)!(N/2 - M_z)!]. \tag{II-38}$$

The energy levels of the Zeeman term and the total magnetic quantum number M_z are shown in Figure II-9. Degenerate in the Zeeman energy, the levels within a manifold are shifted and split by the internal interactions, making possible a large number of spectroscopic transitions or coherences. The dashed lines indicate the MQ transitions, in which several spins flip together subject to the general rule, $n = |\Delta M|$. The number of all possible transitions as a function of their order, n, can be calculated by combinatorial arguments. The number of n-quantum transitions is represented by

$$Z_n = \sum_{M_i - M_j = n} {N \choose N/2 + M_i} {N \choose N/2 + M_j} = {2N \choose N - n}$$
 (II-39)

where $\binom{a}{b} = a!/[(a-b)!b!]$. The number of zero quantum transitions between pairs of states in the same Zeeman manifold is given by

$$Z_0 = \sum_{M_i=N/2-1}^{-N/2+1} {N \choose N/2+M_i} \left[{N \choose N/2+M_j} - 1 \right] = \left[{2N \choose N} - 2^N \right].$$
 (II-39)

For nonzero orders, Eq. II-39 is well approximated by the Gaussian distribution using Stilring's approximation

$$I(n,N) = 4^N / \sqrt{N\pi} * \exp\left(-\frac{n^2}{N}\right) \quad (N \ge 6).$$
 (II-40)

E. Simplified Models of Multiple-Quantum Dynamics

The time-dependent behavior of multiple quantum coherences can be

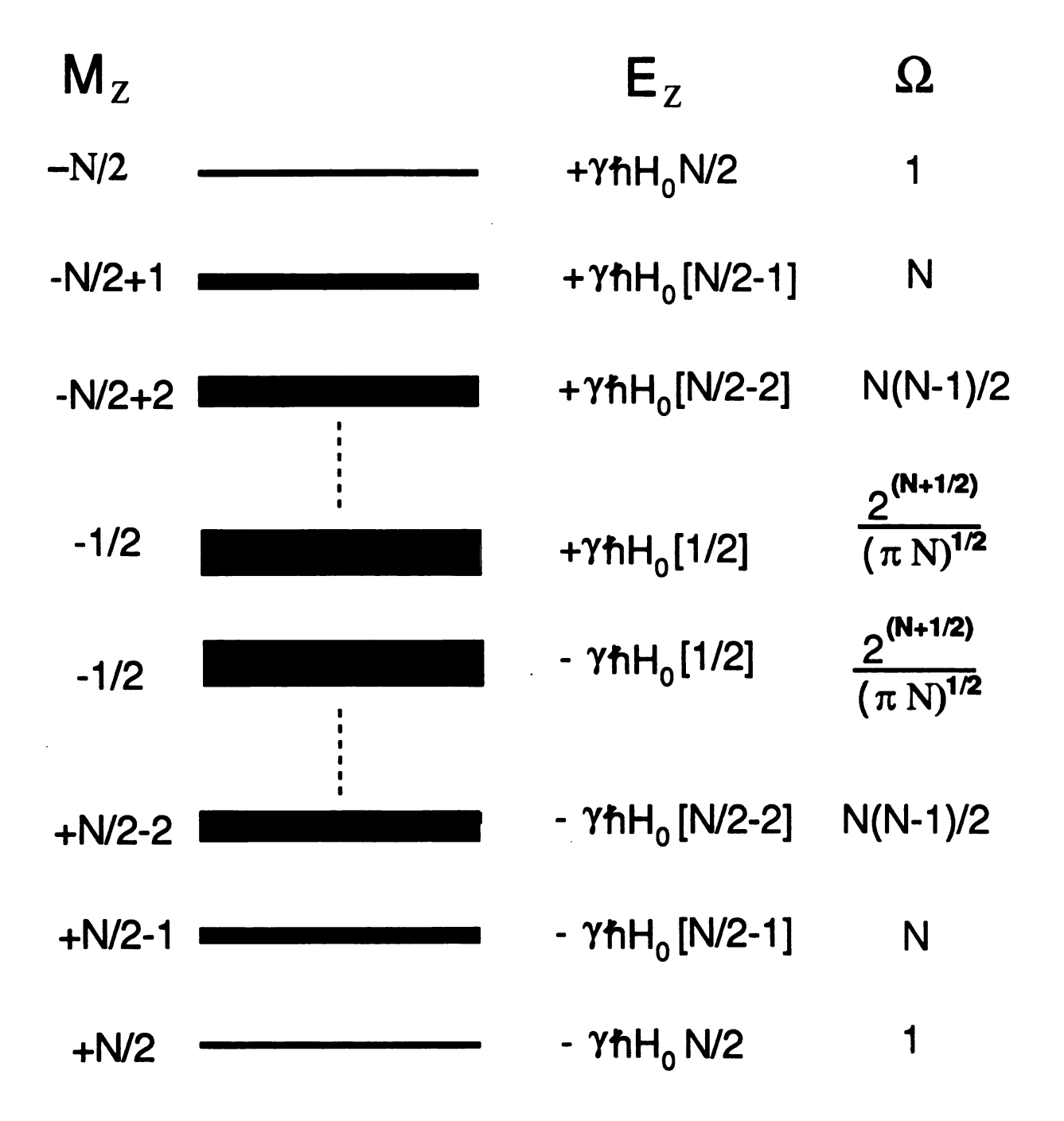


Figure II-9. Schematic energy level diagram for an N (odd) spin-1/2 system in a Zeeman field, and the degeneracy number for Ω of each state. Taken from Ref 53.

Increasing Preparation Time (m) →

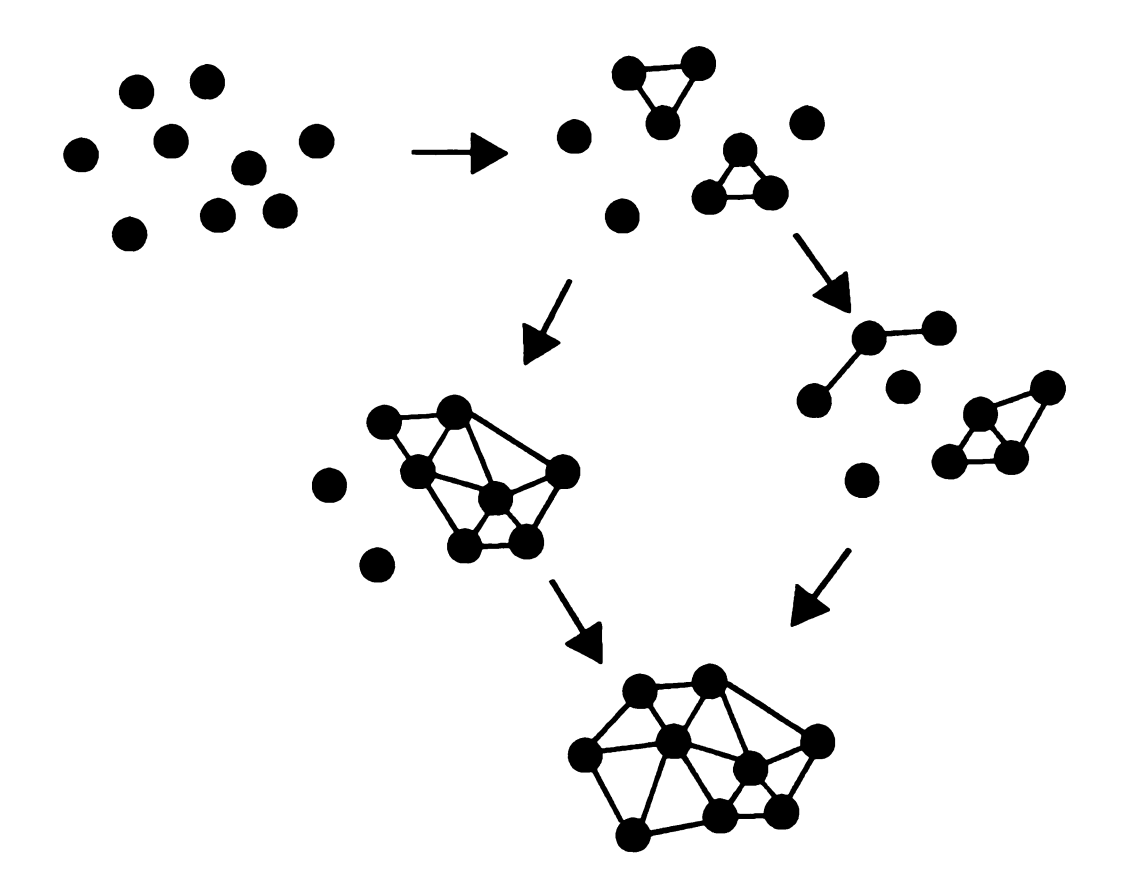


Figure II-10. Symbolic representation of the spreading of multiple spin correlations in a coupling network with increasing preparation time. The circle denote spins and the lines indicate the link of MQ coherences through dipolar couplings

calculated explicitly using the Liouville-von Neuman equation applied to the density matrix. Since the multiple-quantum coherences in solids are created through homonuclear dipolar coupling, we can rewrite Eq. II-14 as

$$\rho(t) = \exp[-(i/\hbar)\mathcal{H}_D t]\rho(0)\exp[(i/\hbar)\mathcal{H}_D t]$$
 (II-41)

where \mathcal{H}_D is defined in Eq.II-31. For short times, an explicit form of the solution of Eq. II-41 can be written as the power series

$$\rho(t) = \rho(0) + (i/\hbar)t[\rho(0), \mathcal{H}_D] + (i/\hbar)^2 (t^2/2!)[[\rho(0), \mathcal{H}_D], \mathcal{H}_D]$$

$$+ (i/\hbar)^3 (t^3/3!)[[[\rho(0), \mathcal{H}_D], \mathcal{H}_D], \mathcal{H}_D] + \cdots.$$
(II-42)

The contribution of high order terms in Eq. II-42 becomes more and more important with increasing time. Figure II-10 shows symbolically the development of multiple-spin correlations by way of the homonuclear dipolar coupling. The number of correlated spins increases with increasing preparation time.

The explicit calculation of the MQ dynamics using the Liouville-von Neuman equation is limited to small spin systems (≤ 9 spins) because it is computationally demanding. Reduction of the size of the operator space can increase the size of the spin systems that can be treated. Since classes of coherences are detected in an MQ experiment, as opposed to individual coherences, a simplified, albeit inexact, calculation of MQ dynamics is possible by use of an average operator. The following sections will discuss two simplified calculations of the MQ dynamics: a directed walk through Liouville space (hopping model)⁵⁷ and a incremental shell model³⁶ making using of the concept of an average operator.

a. Hopping Model

The density operator can be represented by a vector in Liouville space,

$$|\rho(t)\rangle = \sum_{K=0}^{N} \sum_{n=-K}^{K} \sum_{p} g_{Knp}(t) |Knp\rangle$$
 (II-43)

where $g_{Knp}(t)$ is the component of the Liouville states, K is the number of single-

spin operators involved in forming the product operator $|Knp\rangle$ of the Liouville state, n is the order of the coherence, p labels the different states having the same values of K and n. The symbol for Liouville states, $|\cdots\rangle$, is used to distinguish these from the symbol Hilbert states, $|\cdots\rangle$. The equation of motion in Liouville space is represented by a vector equation

$$\frac{d}{dt}|
ho(t)
angle = -i\hat{\hat{\mathcal{H}}}|
ho(t))$$
 (II-44)

where $\hat{\hat{\mathcal{H}}}$ is the superoperator [H,]. Eq. II-43 can be expressed in terms of the components g_{Knp}

$$\frac{d}{dt}g_{Knp}(t) = -i\sum_{K'}\sum_{n'}\sum_{n'}\Omega_{Knp;K'n'p'}g_{K'n'p'}(t)$$
(II-45)

where

$$g_{Knp}(t) = \frac{(Knp|\rho(t))}{(Knp|Knp)}$$
 (II-46)

and

$$\Omega_{Knp;K'n'p'} = \frac{\left(Knp\left|\hat{\mathcal{H}}\right|K'n'p'\right)}{(Knp|Knp)}$$
(II-47)

The different oscillatory behaviors of the various components of the density operator in Eq. II-44 are hidden by destructive interference and resultant decay, which decrease the number of degrees of freedom. Since Eq. II-45 is a kind of first order kinetic equation, Munowitz etc. assumed that the motion of the density operator can be solved by using the following equation

$$\frac{dg}{dt} = \mathbf{R}g \tag{II-48}$$

This equation represents a generalized hopping model, in which the elements of \mathbf{R} give the rate of change from one component of g(t) to another. \mathbf{R} is a matrix of real numbers. For this model, we need to define the space over which the coherences hop and to develop the rates and selection rules that govern the motion.

The size of the Liouville space can be reduced by grouping together modes

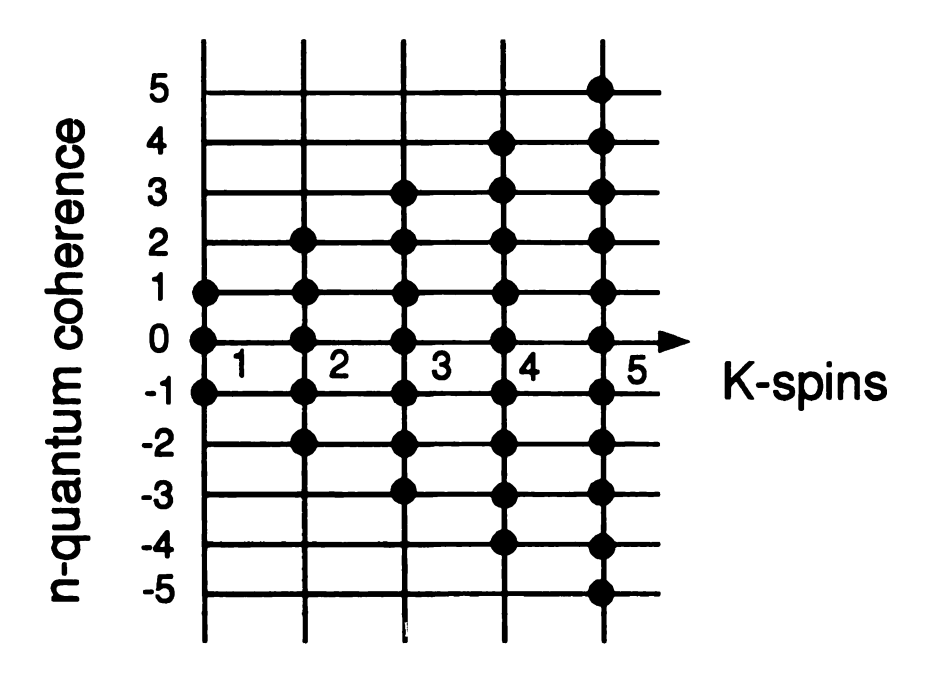


Figure II-11. Projection of Liouville space onto a two-dimensional plane. Each point corresponds to a family of K-spin/n-quantum operators. Taken from Ref. 57

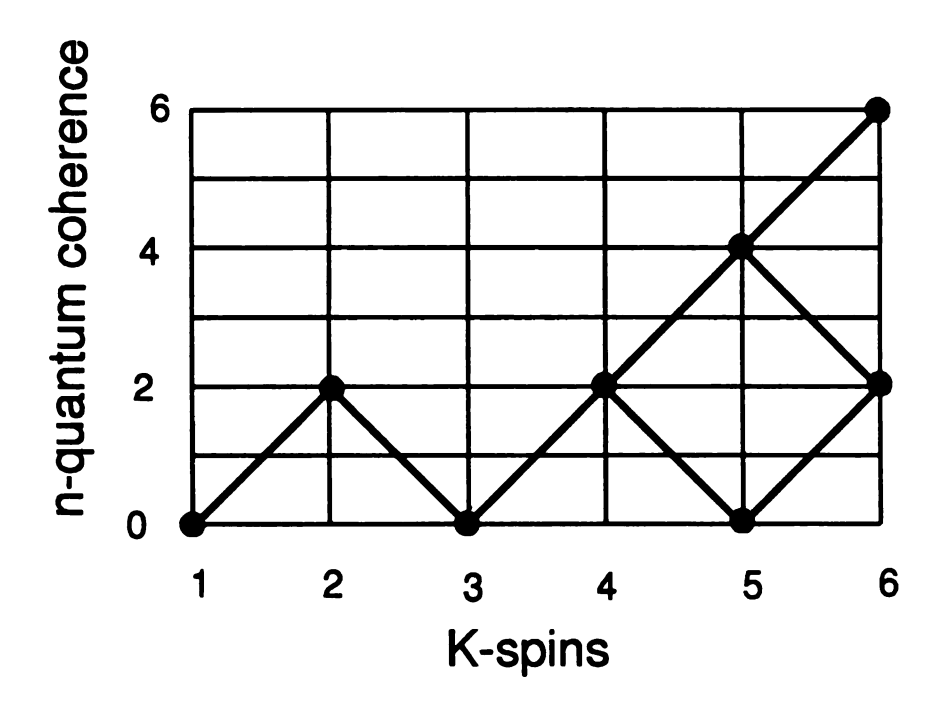


Figure II-12. Pathways of the growth of MQ coherences in Liouville space for a 6-spin system under the 1-spin/2-quantum Hamiltonian. Taken from Ref. 57.

of the quantum numbers K and n. In general, the components of the vector g are labeled as g_{Kn} . The projection of the Liouville space is shown in Fig. II-11. Each point on a two-dimensional grid corresponds to a family of coherences ($|Kn\rangle$) operator basis). K runs from 1 through N and |n| runs from 0 through K. With the assumption that the coherences are of equal magnitude, the number of operators g_{Kn} depends on K, n, and N.

The selection rules and hopping rates from one site to the other site through Liouville space must derive from the Hamiltonian. The MQ pulse sequences in Fig. II-6 used in our experiments create the 1-spin/2-quantum dipolar Hamiltonian which adds one (or subtracts) spins, and changes the order by 2 quanta at a time to a multiple-spin mode. Under this Hamiltonian, the selection rules in the Liouville space are

$$\Delta K = \pm 1, \quad \Delta n = \pm 2. \tag{II-49}$$

The detailed proof is in Appendix B. The pathways through the Liouville space may be constructed on the basis of the selection rules in terms of the specified starting point, that the reduced density operator $\rho(0)$ at thermal equilibrium is proportional to I_z (K=1, n=0). For example, Fig. II-12 shows the allowed changes of the Liouville states of a six-spin system under a 1-spin/2-quantum operator.

The time development of ρ can be solved by using the rate equation (Eq. II-48). With the assumption that all coherences have equal magnitudes, the hopping rates depend on the degeneracies of the coupled states and the strength of the dipolar interaction. Each element of the rate matrix is given by

$$\mathbf{R}_{Kn:K'n'} = \mathbf{W}_{Kn:K'n'}S_1 \tag{II-50}$$

where $W_{Kn;K'n'}$ is the generic hopping rate between g_{Kn} and $g_{K'n'}$, and S_1 is the lattice parameter, which reflects the strength of the dipolar couplings. The general

behavior represented by the statistical factors (the degeneracies of the Liouville state) as well as the individual details represented by the structural factor (dipolar couplings) are of interest in this model. As a first approximation, we will concentrate on the universal trends, leaving S_1 as an adjustable parameter to fit the behavior of arbitrary systems of N spins to specific experimental examples. The lattice parameter, which depends on the structure of the material, may be given by a lattice sum of the coupling constants

$$S_1 = \frac{1}{N} \sum_{i < j} |D_{ij}|. \tag{II-51}$$

as an approximation, we may simply take S_1 as proportional to the dipolar linewidth or the square root of the second moment.

The matrix elements (hopping rates) are constructed from the degeneracies of the Liouville states $|Kn\rangle$ and $|K'n'\rangle$. Let c_+ be the number of raising operators, c_- the number of lowering operators, and c_0 the number of zero-quantum operators so that

$$c_+ - c_- = n \tag{II-52}$$

and

$$c_{+} + c_{-} + c_{0} = K \tag{II-53}$$

For a given choice of c_+ and c_- , the number of ways to choose c_+ operators out of K spins is given by the combinatorial coefficient

$$\binom{K}{c_+} = \frac{K!}{C_+!(K-c_+)!}$$
 (II-54)

Similarly, the number of different ways of choosing c_- spins out of the remaining $\mathsf{K}-c_+$ is represented by

$$\binom{K-c_+}{c_-}.$$
 (II-55)

Therefore, the total number of ways to choose c_+ and c_- is the product of the binomial coefficients of Eqs. (II-48) and (II-49). The degeneracy of the Liouville

state is obtained by summing over all admissible values of c_+ , beginning with $c_+=n$, and multiplying the total combinatorial factor to account for the number of ways that K spins can be selected from N. The result is

$$\Lambda_{N,Kn} = \binom{N}{K} Q_{Kn} \tag{II-56}$$

where

$$Q_{Kn} = \sum_{c=|n|}^{c_{max}} {K \choose c} {K-c \choose c-|n|}.$$
 (II-57)

The degeneracy of the Liouville state is used to calculate the hopping rates. For 2-quantum/1-spin operator (H_{yx}) , the forward rate in which K increases is given by

$$W_{Kn;K+1,n\pm 2} = \frac{K(N-K)}{N-1} \cdot \frac{Q_{K-1,n} + Q_{K-1,n\pm 1}}{Q_{Kn}}$$
 (II-58)

and the reverse rate in which K decreases is given by

$$W_{K+1,n\pm2;Kn} = \frac{K(K+1)}{N-1} \cdot \frac{Q_{K-1,n}+Q_{K-1,n\pm1}}{Q_{K+1,n\pm2}}.$$
 (II-59)

Given the rate matrix (Eq. II-48) we can compute all the coherence amplitudes $g_{Kn}(t)$ by solving Eq. II-47. Then summing over all K gives the amplitudes of n-quantum coherences

$$g_n(t) = \sum_K g_{Kn}(t). \tag{II-60}$$

Figure II-13 shows the theoretical development of the n-quantum intensities for systems of both 6 and 20 spins evolving under H_{yx} . The matrix dimensions for 6 and 20 spin systems are 6 and 60 respectively. The effective sizes are obtained from the theoretical calculation by fitting the orders n to a Gaussian distribution (Eq. II-40) for each preparation time. The effective size of the 20 spin system increases with increasing preparation time, finally reaching an equilibrium at the longer preparation time (see Fig. II-14).

The hopping model makes it possible to understand the evolution of the MQ dynamics in systems too large or too complicated to be treated exactly. The

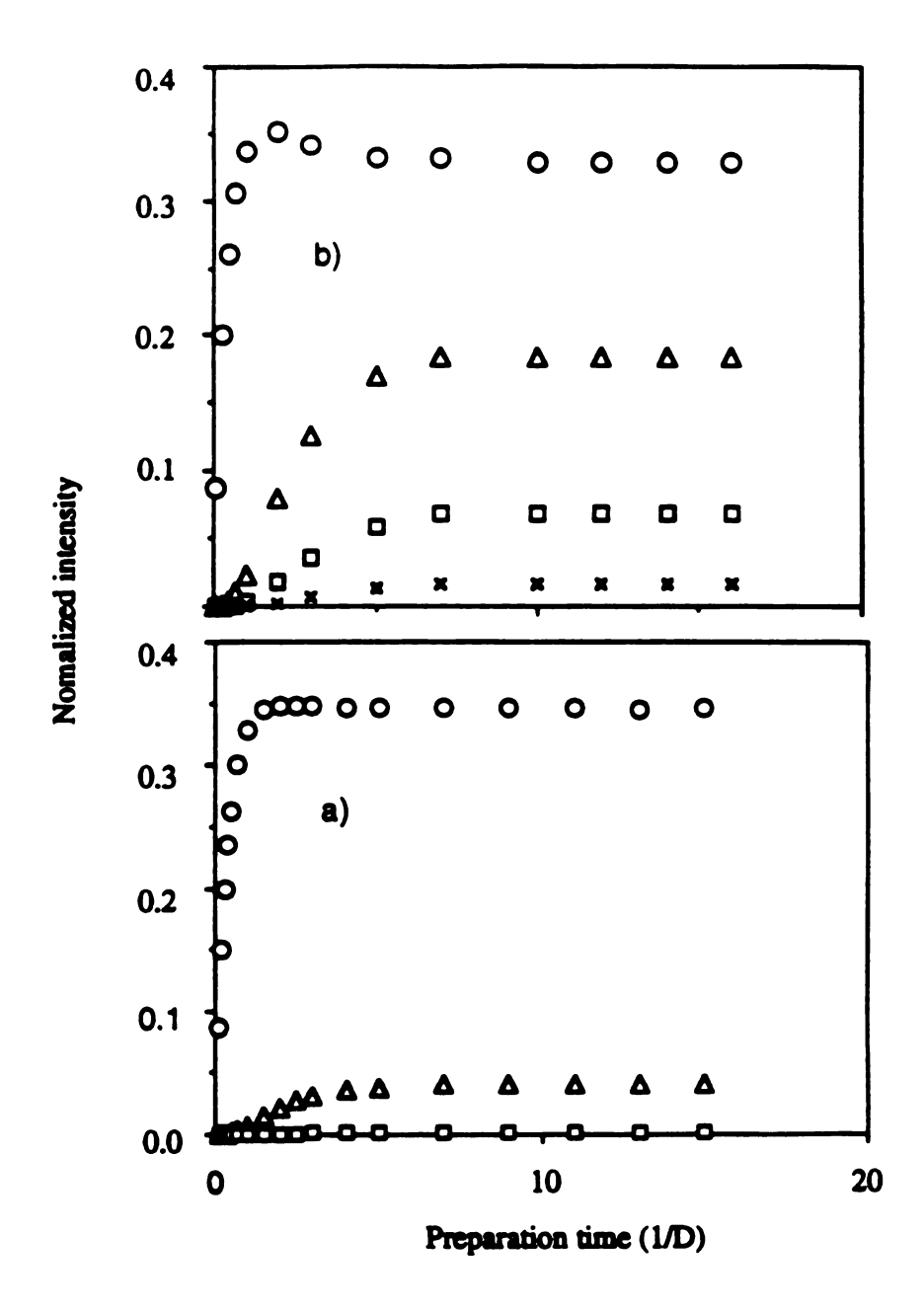


Figure II-13. Evolution of n-quantum coherences predicted by the hopping model in 6 (a) and 20 (b) spin systems. 2Q (open circle), 4Q (open triangle), 6Q (open square), and 8Q (cross).

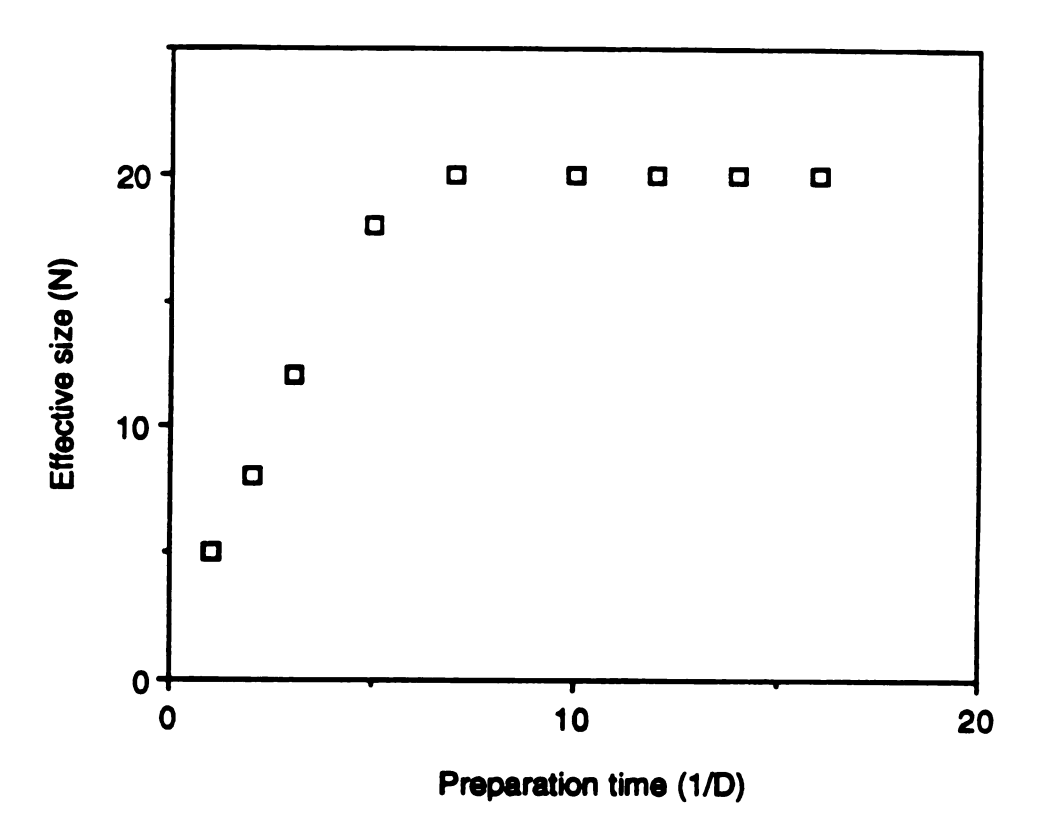


Figure II-14. Development of effective size with increasing preparation times for a 20 spin system predicted by the hopping model. The effective size for each preparation time is fitted by a Gaussian function.

replacement of the Liouville-von Neumann equation by a set of rate equations with an exponential solution is based on the severe damping that accompanies the superposition of a large number of different frequency components. The equation in the hopping model can be solved straightforwardly for groups of spins of various sizes. However, it cannot directly incorporate the effects of dimensionality on multiple quantum dynamics, and is limited to approximately 40 spins.

b. Incremental Shell Model

As mentioned above, the density operator needs to be simplified in order to understand the MQ dynamics in larger spin systems. In the incremental shell model,³⁶ it is assumed that the density operator can be approximated by a weighted sum of time independent angular momentum operators, $P_{m\alpha}$, where both m and α are vectors of dimension M

$$\rho(t) = \sum_{\mathbf{m}} \sum_{\alpha} c_{\mathbf{m}\alpha}(t) P_{\mathbf{m}\alpha}.$$
 (II-61)

Since the operator products $P_{\mathbf{m}\alpha}$ are time-independent, all information on the time-evolution of MQ coherences is contained in the coefficients $c_{\mathbf{m}\alpha}(t)$. The angular momentum operator products can be given by

$$P_{\mathbf{m}\alpha} = \prod_{k=1}^{M} I_{m_k \alpha_k} \tag{II-62}$$

where m_k is the index of all M spins of the vector m, and α_k is the angular momentum operator (+ = 1, - = -1, and z=0) for spin k.

We rewrite Eq. II-31 for calculations using the incremental shell model as

$$\mathcal{H}_{yx} = \frac{1}{4} \sum_{i} \sum_{j>i} D_{ij} Q_{ij}$$
 (II-63)

where D_{ij} is the dipolar coupling between the pair of nuclei i and j Q_{ij} is a condensed notation for raising and lowering operators $(I_{i+}I_{j+} + I_{i-}I_{j-})$. From Eqs. (II-61) and (II-62), the Liouville-von Neumann equation can be represented in the form of a summation of operator products

$$\sum_{\mathbf{m}} \sum_{\alpha} \frac{dc_{m\alpha}}{dt} P_{\mathbf{m}\alpha} = \frac{i}{4} \sum_{\mathbf{m}} \sum_{\alpha} c_{\mathbf{m}\alpha} \left(\sum_{i} \sum_{j=i} D_{ij} [P_{\mathbf{m}\alpha}, Q_{ij}] \right)$$
 (II-64)

where the factor i is the square root of -1 (since there is an i representing nucleus i). The MQ coherence growth is contained in the time-dependent coefficients $(c_{m\alpha})$. In large spin systems, since the large number of terms in the summation makes explicit calculation of Eq. II-58 impracticable, we need to simplify Eq. II-58 and find the selection rules resulting from the commutator $[P_{m\alpha}, Q_{ij}]$. In order to simplify the Eq. II-58, we follow Levy and Gleason³⁶ and assume that the individual operators $P_{m\alpha}$ can be replaced by an average operator P_M , and set D_{ij} to zero for all non-neighboring nuclear pairs. All combinations of individual product operators having the same number of individual spin operators in their product are represented by the one average operator. Figure II-16 shows an average 4 spin operator schematically formed from a combination of individual 4 spin operators of 9 spins in real space. We can rewrite Eq. II-61 with the average operator

$$\rho(t) = \sum_{\mathbf{m}} \sum_{\alpha} c_{\mathbf{m}\alpha}(t) P_{\mathbf{m}\alpha} \simeq \sum_{M} C_{M}(t) P_{M}$$
 (II-65)

where C_M is the summation of the coefficients $c_{\mathbf{m}\alpha}$ over all values of m and α . Then, Eq. II-64 can be rewritten as

$$\sum_{M} \frac{dC_{M}}{dt} P_{M} = \frac{i}{4} \sum_{M} C_{M} \left(\sum_{i} \sum_{j=i} D_{ij} [P_{M}, Q_{ij}] \right). \tag{II-66}$$

The commutators $[P_M,Q_{ij}]$ can be evaluated according to the selection rules for MQ evolution. Since the dipolar coupling is proportional to the inverse cube of the distance, only adjacent i, j pairs are used to calculate the commutator. The MQ coherence growth depends on the position of spins. First, when both spins i,j of the pair are outside of the existing multi-spin coherence, the coherences do not grow since the commutator is zero. Secondly, when one spin is inside of the existing coherence and the other is outside, P_M and Q_{ij} do not commute since

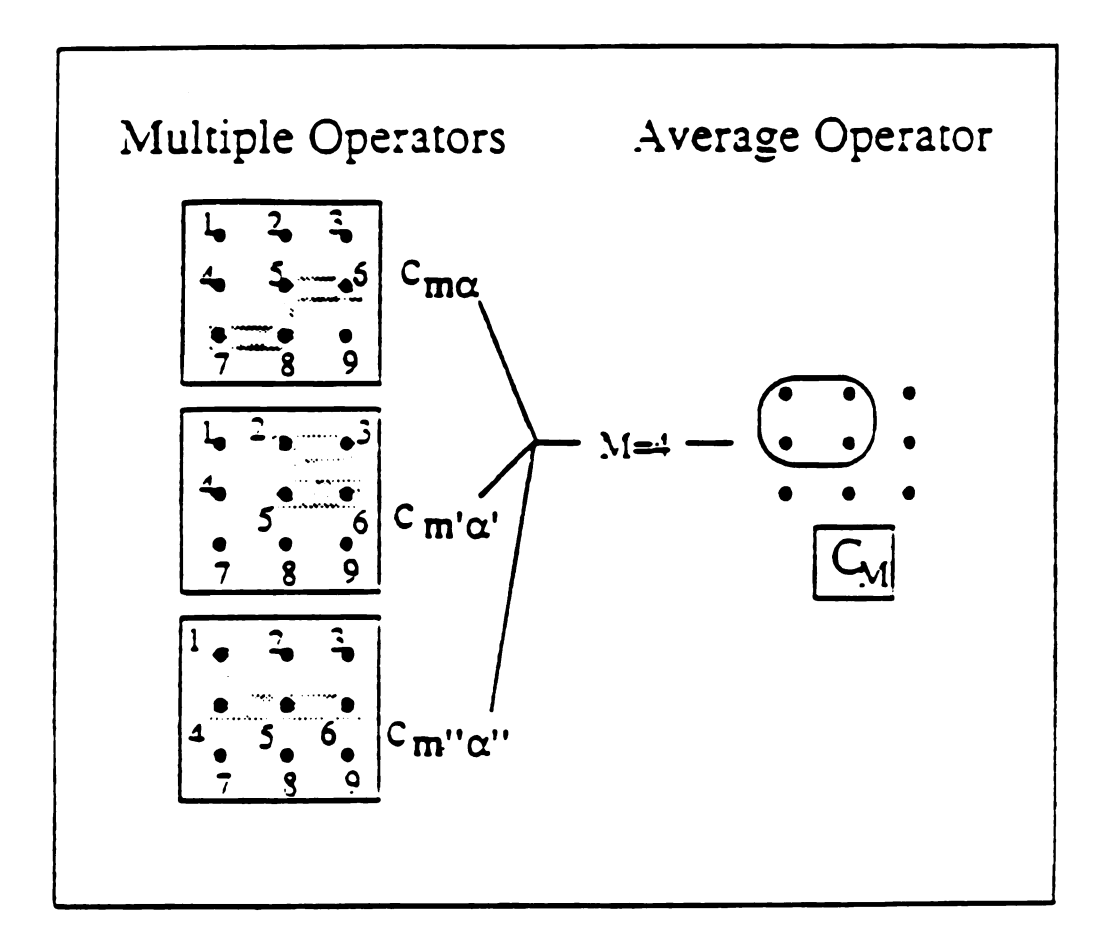


Figure II-15. Diagram representing the average M spin operator and its constituent operators for M = 4 in a 9 spin system. The individual components $c_{m\alpha}$ are simplified to an average coefficient for the M spin operator C_M . Taken from Ref. 36.

they will contain operators for the same spin. In this case, the commutator increases the number of spins in the product operator by one (forward growth). The third case involves a spin pair i,j inside the existing coherence. Non-zero commutators then decrease the number of spins in the product operators by one (reverse growth). The commutator averaging over all possible combinations of I_z , I_+ and I_- for spins i, j yields³⁶

$$[P_M, Q_{ij}] = 0 \quad i \notin M, j \notin M \tag{II-67a}$$

$$=2P_{M+1} \quad i \notin M, j \in M \text{ or } i \notin M, j \in M$$
 (II-67b)

$$=(2/3)P_{M-1}$$
 $i \in M, j \in M.$ (II-67c)

The selection rule for the growth of the average product operator is $\Delta M=\pm 1$, in agreement with that for the hopping model. Plugging Eq. II-67 into Eq. II-66, we can rewrite Eq. II-66 as

$$\sum_{M} \left(\frac{dC_{M}}{dt} \right) = \frac{-i}{4} \sum_{M} C_{M} \left[2 \sum_{i \in M} \sum_{j \ni M} D_{ij} (2P_{M+1}) + \sum_{i \in M} \sum_{j \in M} D_{ij} \left(\frac{2}{3} P_{M-1} \right) \right]$$

$$= \frac{-i}{4} \sum_{M} C_{M} \left(W_{M+1}^{f} P_{M+1} + W_{M-1}^{r} P_{M-1} \right)$$
(II-68)

where W_{M+1}^f and W_{M-1}^r are the forward and reverse rate coefficients. The orthogonal property of the term P_M more simplifies the Eq. II-68 to :

$$\frac{dC_M}{dt} = \frac{-i}{4} W_{M-1}^f C_{M-1} - \frac{i}{4} W_{M+1}^r C_{M+1}. \tag{II-69}$$

The forward rate coefficients, W_{M}^{f} , are defined as

$$W_M^f = 4 \sum_{i \in M} \sum_{j \notin M} D_{ij}. \tag{II-70}$$

Since the rate of increase of the effective size depends upon the number of spins outside of the existing spin coherence that are on the periphery of the cluster, we can rewrite Eq. II-70 as

$$W_{M}^{f} = 4D_{12}n_{n}n_{s} \tag{II-71}$$

where n_n is the number of spins outside the coherence adjacent to a single spin in the coherence and n_s is the effective number of nuclei at the edge of a coherence. As shown in Figure II-17, higher dimensional arrangements of spins have more spins outside a given cluster available to enter the coherence. Therefore, lines (1-D), squares (2-D), and cubes (3-D) have different forms for n_s represented by

$$n_s = 2 (II-72a)$$

$$n_s = 4(M)^{1/2}$$
 (II-72b)

$$n_s = 6(M)^{2/3}$$
. (II-72c)

The parameter n_n , of the order of 1-3, has been used to fit the experimental data, although we will treat it as fixed (=1) for our 1-D system.

The reverse rate coefficients W_M^r are obtained by the fact that the norm of all C_M terms is conserved during the evolution time:

$$\sum_{M} \frac{d(C_{M}^{*}C_{M})}{dt} = \sum_{M} \left(C_{M}^{*} \frac{dC_{M}}{dt} + C_{M} \frac{dC_{M}^{*}}{dt} \right). \tag{II-73}$$

Under the action of the dipolar Hamiltonian $\overline{\mathcal{H}}_{yx}$ through the Liouville-von Neumann equation, all coefficients C_M with odd M are real numbers and the others are imaginary numbers. Thus, the derivative of the norm of C_M can be represented as

$$C_{M}^{*} \frac{dC_{M}}{dt} + C_{M} \frac{dC_{M}^{*}}{dt} = \left(W_{M-1}^{f}|C_{M}||C_{M-1}| + W_{M+1}^{r}|C_{M}||C_{M+1}|\right) \times (-1)^{M-1}. \quad \text{(II-74)}$$

Since the derivative of the norm must be equal zero, the normalization condition of Eq. II-74 can be given by:

$$\sum_{M} \left(W_{M-1}^{f} W_{M}^{r} \right) |C_{M}| |C_{M-1}| = 0$$
 (II-75)

where W_{M-1}^f should be equal to W_M^r , since the time-dependent C_M terms are variable in the linear equation (Eq. II-75). Therefore, the reverse rate coefficient can be calculated from forward rate coefficient given by Eq II-71.

 C_1 is equal to 1 at t=0. The time-dependent C_M terms for higher values of M increase as the preparation time increases. Therefore, the center of mass of C_M moves to higher M values at longer preparation times. Levy and Gleason³⁶ chose to approximate the effective size N by this center of mass:

$$N = \frac{\sum\limits_{M} M(C_M^{\bullet} C_M)}{\sum\limits_{M} (C_M^{\bullet} C_M)} . \tag{II-76}$$

Although the effective size from Eq. II-76 may not correspond exactly to that obtained using the statistical model, it is useful for comparisons with experimental data. Simulations of MQ coherence growth in spin systems of different dimensionalities (1D, 2D and 3D) are shown in Figure II-18. These calculations were performed with n_s obtained from Eq. II-66, n_n =1 and D_{12} = 1.0 kHz. The curves shown are approximately linear, quadratic, and cubic for the one, two and three dimensional cases respectively, only slightly deviating from these forms at early times. This program was kindly provided by Dr. K. K. Gleason of the Massachusetts Institute of Technology.

3. Experimental

A. Multiple-Quantum NMR Studies

The ¹H and ¹⁹F multiple-quantum experiments were carried out on a Varian VXR-400S spectrometer equipped with a 100 watt amplifier (400 and 376 MHz) and a high power probe with a 5 mm o.d. solenoid coil for ¹H and 7 mm o.d. for ¹⁹F. The phase-incremented even-order selective multiple-quantum pulse sequence in Fig. II-5 that was used increases the S/N ratio and saves experimental time compared to the TPPI method, at the expense of information about the

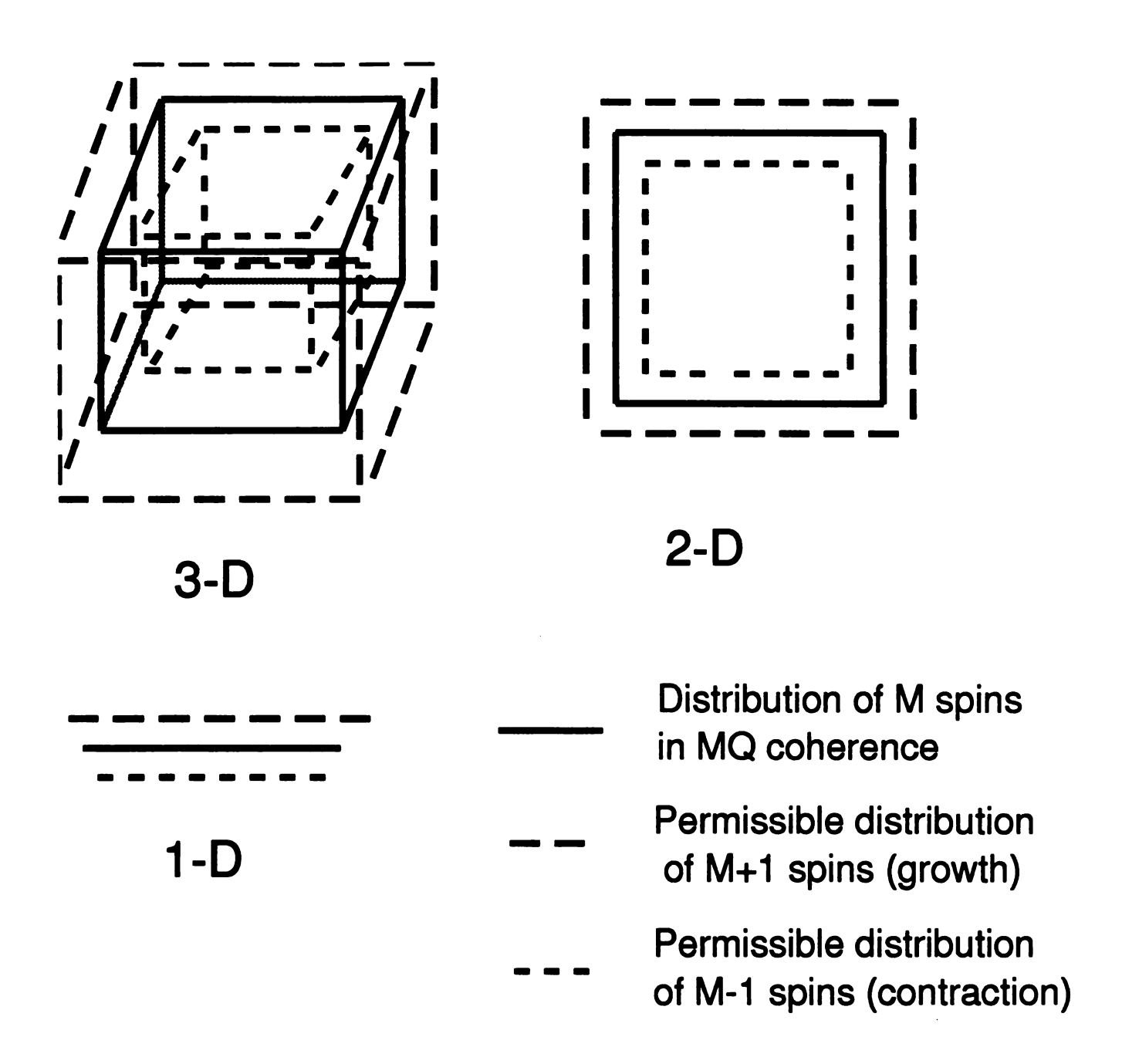


Figure II-16. Schematic diagram of the growth of MQ coherence in the systems of different dimensionalities.

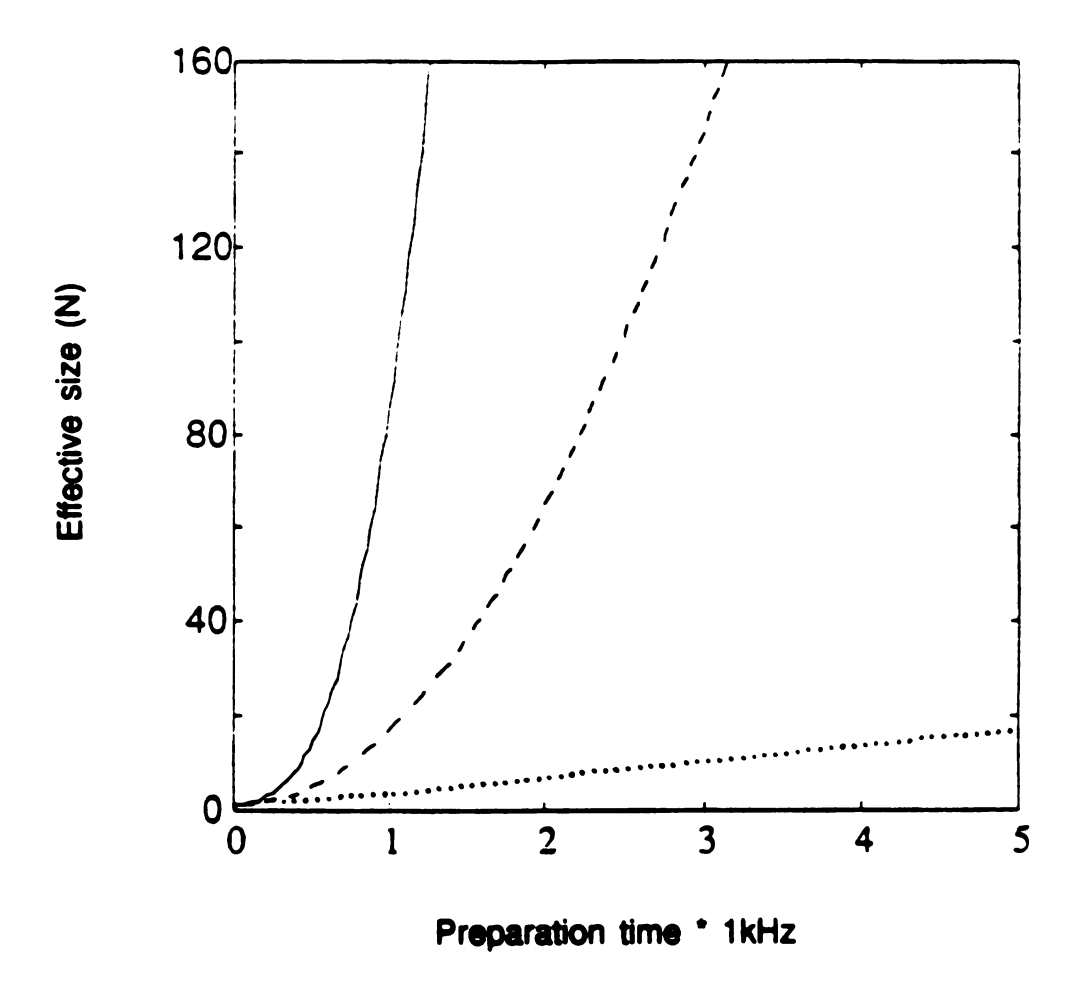


Figure II-17. Values of effective size N predicted by the incremental shell model for spin-1/2 nuclei evenly spaced on a line (1-D), square (2-D), and cubic (3-D) lattice. The dotted, dashed, and solid lines represent the 1-D, 2-D, and 3-D MQ coherence growth curves. Figure is courtesy of Dr. K. K. Gleason.

individual line-widths of each order.⁴⁰ The $\pi/2$ pulse lengths are 3.8 μ s for ¹H and 4.6 μ s for ¹⁹F, and the basic cycle times are 72 μ s and 78 μ s respectively. The t1 value was fixed at 2 μ s, and relaxation delays greater than five times T₁ were used. The highest coherence order, n_{max}, detected is governed by the digital phase shift increment $\Delta\Phi$: $\Delta\Phi = \pi/n_{max}$. A 2 ms delay after the mixing time is used to allow the transverse magnetization to decay. The data are detected with a $\pi/2$ pulse, followed by a 100 μ s spin locking pulse. A pseudo-1D spectrum with 64 complex points in the "t1-domain" (phase-incremented) was obtained by sampling a single complex point in the t2-domain 35 μ s after the last (spin-lock) pulse. Unwanted odd order multiple-quantum coherences are eliminated by a 180° phase shift of the detection pulse at every scan. Because of the periodic nature of the data, increased digital resolution was obtained by replicating the "FID". The number of correlated spins N (the effective size) was obtained by least-square fitting of the orders of coherence (excluding 0 quantum coherence) to a Gaussian function, according to the widely-employed statistical model. 31,52,53,55,56 The MQ intensity distribution should be symmetric, $I_n = I_{-n}$ theoretically from Eq. II-40. Since the intensities of the positive MQ orders and the negative MQ orders are slightly different experimentally, the sum of the positive and negative MQ orders $(I_n + I_{-n})$ was used in the fitting. The sum of all multiple-quantum intensitie $[\Sigma(I_0 + I_{-n})]$ $l_n + l_{-n}$)] at a given preparation time was normalized to unity.

Since the chemical shift anisotropy of single crystal fluorapatite (hereafter referred to as FAP) is known (84ppm),⁶⁵ the angles between the c axis of single crystal FAP (the σ_{\parallel} direction) and the external magnetic field were calculated from the observed chemical shifts. The PC-based computer program ANTIOPE⁶⁶ was used for explicit calculations of MQ dynamics of single crystal fluorapatite (FAP)

at different orientations. A basic cycle time of 30 μ s was used. Calculation of spin dynamics of up to 5 spin-1/2 nuclei is possible with the ANTIOPE program.

B. Sample Preparation and Characterization

Hexamethylbenzene, C₆(CH₃)₆, was obtained from Aldrich and used for the multiple-quantum experiments. The sample of partially monoclinic hydroxyapatite (hereafter referred to as HAP-M) was prepared, 67 analyzed and provided by Dr. Bruce Fowler of the National Institute of Standards and the National Institute of Dental Research. Using the intensity of weak X-ray powder diffraction peaks characteristic of monoclinic hydroxyapatite⁵⁹ relative to that of a strong peak arising from the hexagonal form⁵⁸, along with theoretical calculated intensities for the powdered monoclinic form, his analysis of HAP-M showed that roughly 70 % of the sample is in the monoclinic form. Its hydroxyl content is therefore assumed to be highly stoichiometric compared to most hydroxyapatite preparations, especially precipitated samples. Another sample of hydroxyapatite (hereafter referred to as HAP-N) was prepared by aqueous precipitation and characterized by many methods; 68,70 a hydroxyl content in HAP-N was determined to be 92% by quantitative ¹H MAS-NMR, and 81% by IR.⁶⁸ The solid solutions of fluorohydroxyapatite (FOHAP), $Ca_5(OH)_{1-x}F_x(PO_4)_3$, with the different fluorine mole fraction (x = 0.24) and 0.41) were synthesized by aqueous precipitation at a boiling temperature.⁷⁰ Their characterization has been previously reported. 69,71 A specimen of single crystal fluorapatite was kindly loaned by Dr. Bruce Fowler. The color of this sample is pale yellow, with no obvious inclusions, and the diameter and length are about 4mm and 7 mm respectively.

4. RESULTS

A. ¹H Multiple-Quantum NMR Study of Off-Resonance Effects

Hexamethylbenzene was used to check off-resonance effects in the MQ NMR experiments. The half-height linewidth of hexamethylbenzene in the static ¹H spectrum is about 11 kHz. The planar benzene rings of hexamethylbenzene in the triclinic unit cell form a nearly perfect hexagonal net.⁷² Since fast reorientation of each methyl group along its C₃ axis makes the three proton nuclei equivalent, the CSA of hexamethylbenzene is negligible. The sixfold hopping of the hexamethylbenzene about the C₆ axis of the benzene ring lessens the intramolecular dipolar coupling between ortho-, meta-, and para-methyl groups.⁷³ Thus, breadth of the peak arises mostly from the intermolecular dipolar coupling.

Figure II-18 shows multiple-quantum spectra of hexamethylbenzene with a preparation time of 504 μ s obtained with different transmitter carrier frequencies. The location of the transmitter was varied from the middle of the ¹H static lineshape to 4 kHz off-resonance in intervals of 1kHz. The 2 quantum peak on resonance (Fig. II-18a) is more intense than any other peak, but moving the transmitter from the center of the spectrum diminishes the relative intensity of the 2 quantum peak, eventually resulting in an inverted peak (Fig. II-18b to e). The intensities of the higher-order peaks, shown in Fig. II-18 with the same vertical scale, also decrease with increasing resonance offset.

Static ¹H spectra, normalized to the same peak height, of HAP-M, HAP-N, FOHAP x=0.24 and FOHAP x=0.41 are shown in Figure II-19. The spectrum of the low specific surface area (2.1m²/g) HAP-M sample in Figure II-19a does not show evidence of a peak from surface adsorbed water (around 5.6 ppm)⁶⁹ but instead only a 2 kHz broad peak, whose width is due to the CSA of the hydroxyl

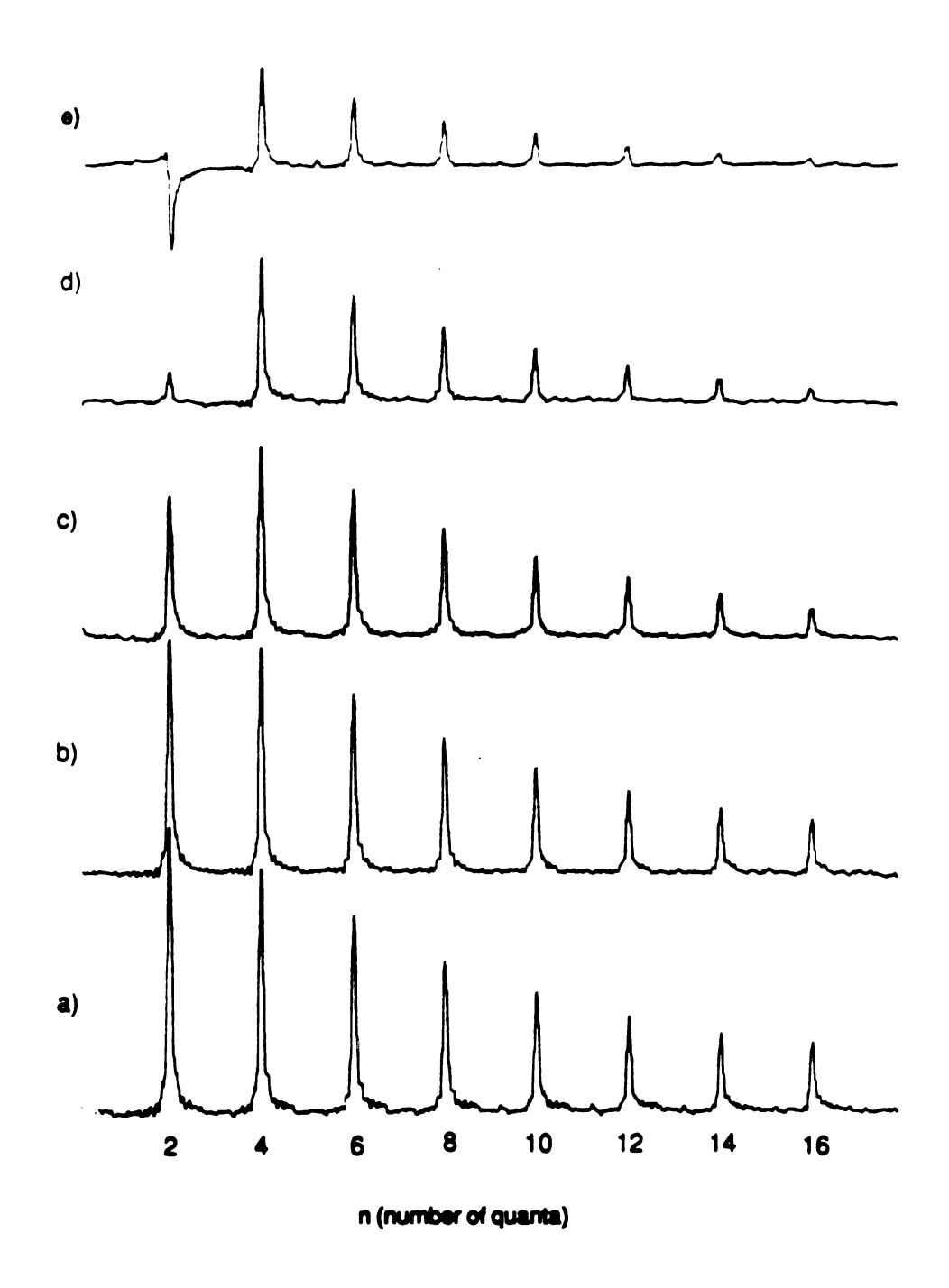


Figure II-18. ¹H PI-MQ-NMR spectra of hexamethylbenzene with different transmitter carrier frequencies. See text.

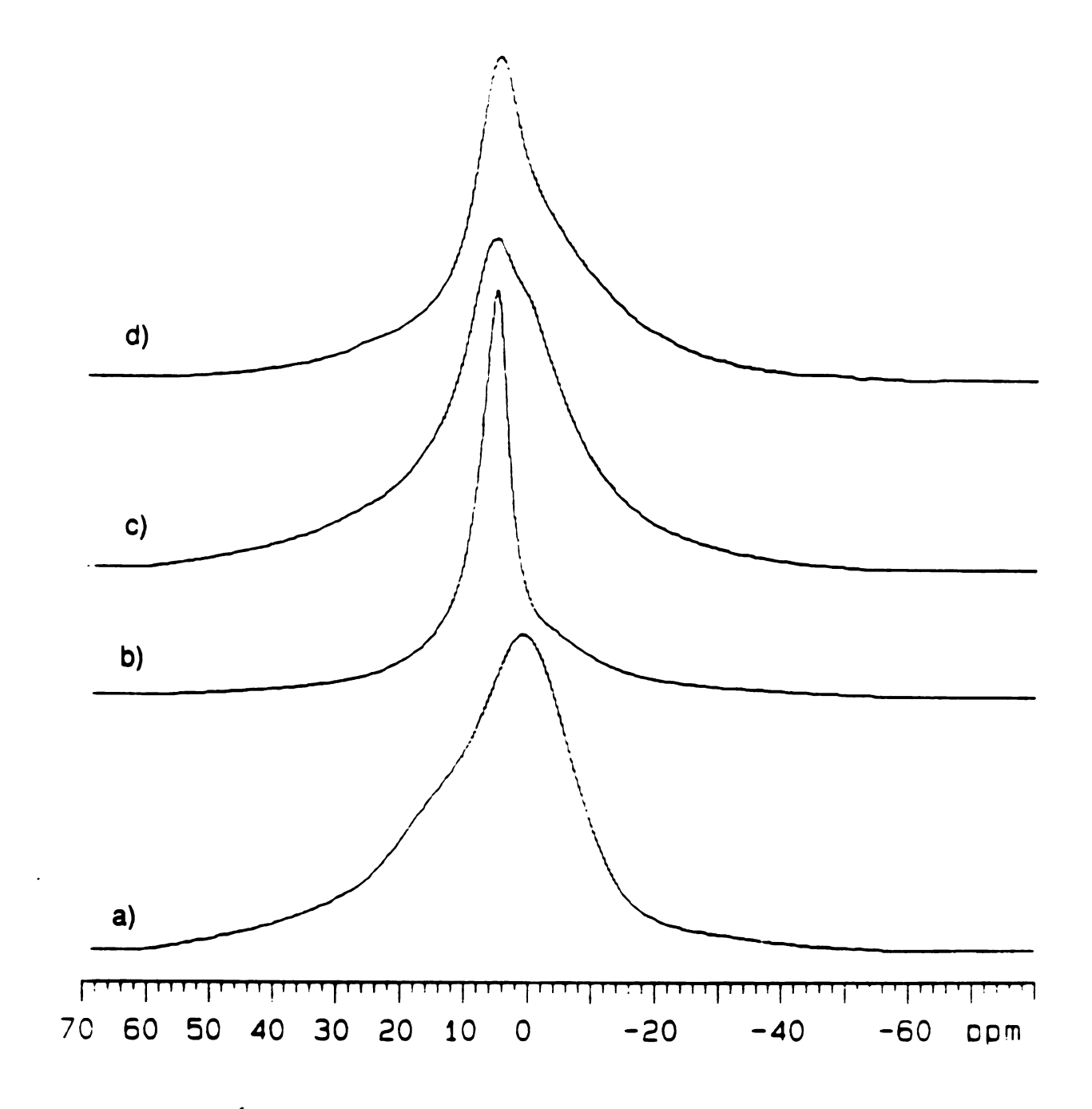


Figure II-19. ¹H 1-dimensional spectra of apatite samples. HAP-M (a), HAP-N (b), FOHAP x=0.24 (c), and FOHAP X=0.41 (d).

group, and homo- and heteronuclear dipolar couplings. The strong signal in HAP-N around 5.6 ppm (Fig. II-19b) has been assigned to mobile water at the surface. The peak of hydroxyl groups in HAP-N is concealed by that of surface adsorbed water (the specific surface area of HAP-N is $37m^2/g$). The weak intensity of the ¹H MAS-NMR spinning sidebands of the surface absorbed water groups indicates that homonuclear dipolar couplings among these protons are negligible. ⁶⁹

Figure II-20 shows the 1 H multiple-quantum spectrum of the highly stoichiometric HAP-M sample for a preparation time of 864 μ s, as well as the Gaussian fit corresponding to an effective size of 12.3. The higher orders of multiple-quantum coherences deviate from a Gaussian distribution, 31 being more intense than predicted.

Figure II-21 displays the intensities of the multiple-quantum peaks for HAP-M with a preparation time of 864 μs as a function of resonance offset. The isotropic chemical shift of hydroxyapatite is 0.2 ppm, but the position of highest intensity of HAP-M (2.8 ppm) is regarded as "on-resonance", and the transmitter offset is varied by up to ± 2 ppm (800 Hz at 9.4T). The change of the transmitter offset position has only a slight influence on the intensities of the 2 quantum and 4 quantum peaks, shown in Fig. II-21a with the same vertical scale. Since the effective size is measured from the ratios of intensities of multiple-quantum peaks, we can redraw Figure II-21a with intensities normalized to the 2-quantum peak. The resulting intensity profiles, shown in Figure II-21b are not changed much by varying the transmitter offset by ± 2 ppm for a preparation time of 864 μs . Figures II-22a and b have the same parameters as Fig. 21a and b except for the preparation time (1872 μs). The intensities (with the same vertical scale) of multiple-quantum coherences obtained on resonance are always stronger than

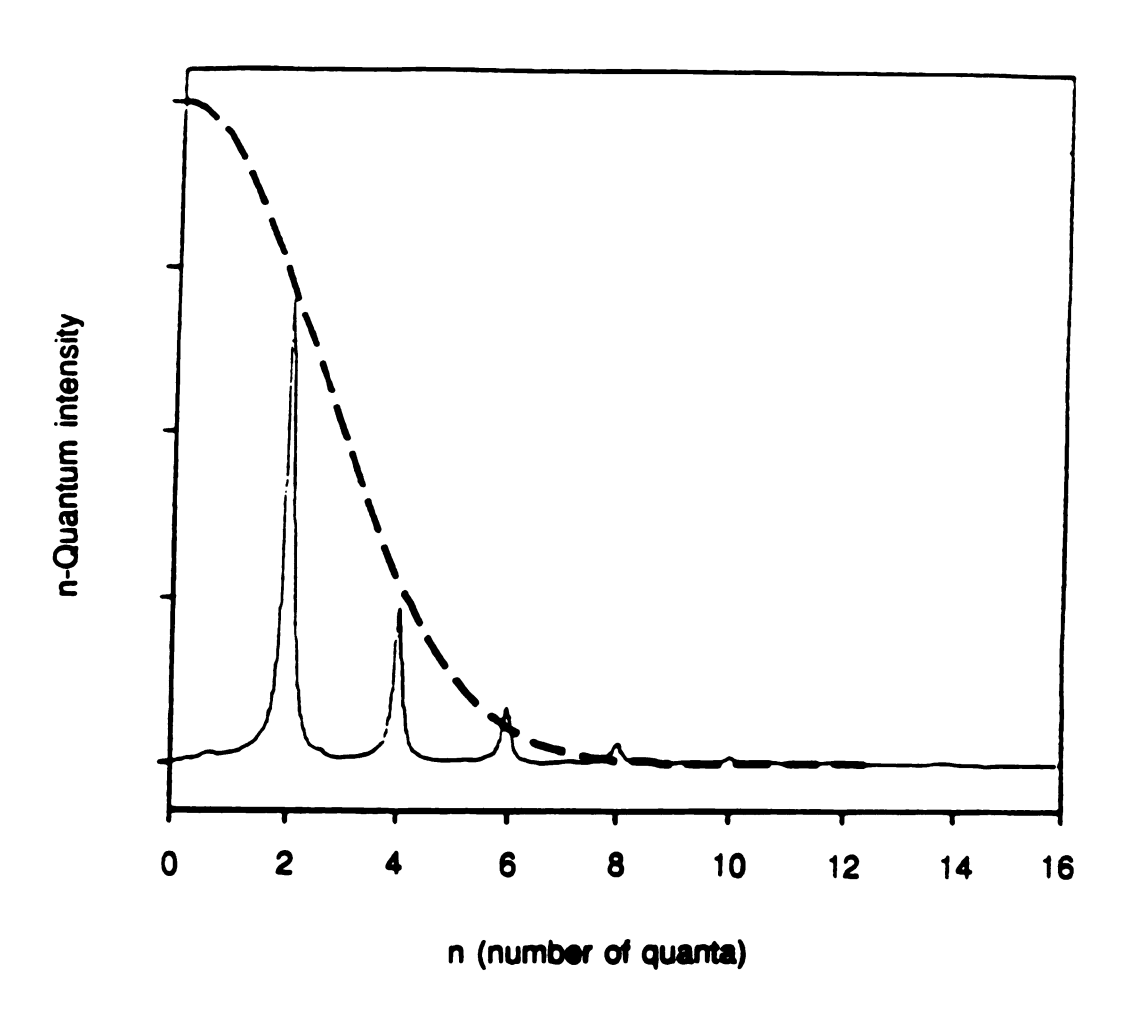


Figure II-20. ¹H MQ NMR spectrum of HAP-M using a preparation time of 864 μ s. The dashed line represents a Gaussian fit to the data with effective size N = 12.3.

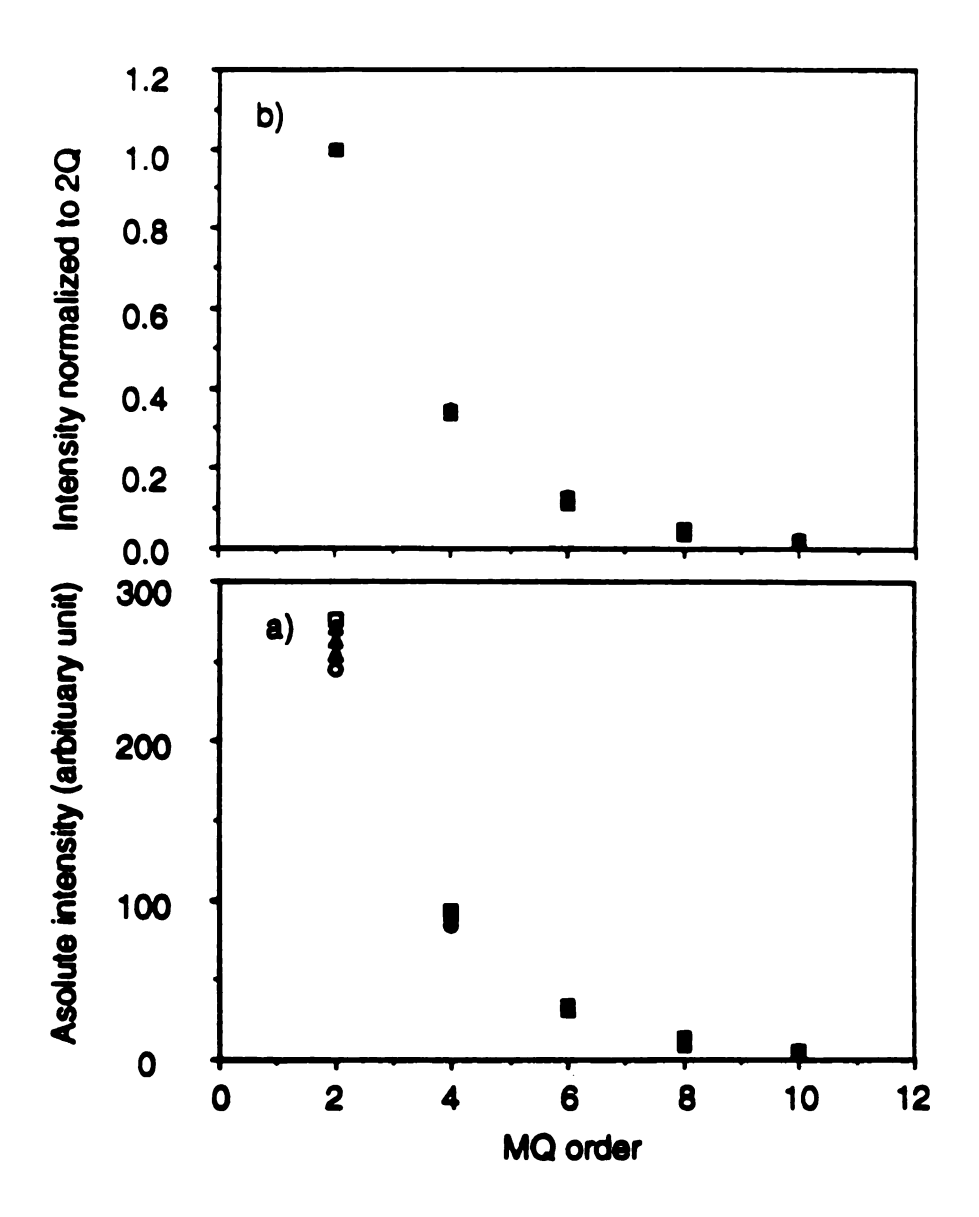


Figure II-21. Intensities of the 1H PI NMR MQ orders of HAP-M for various resonance offsets using a preparation time of 864 μ s. a) Intensities on the same vertical scale. b) Intensities normalized to the 2-Q intensity. On resonance (open square), 1 ppm off resonance (open triangle), 2 ppm off resonance (open circle), -1 ppm off resonance (black triangle), and -2 ppm off resonance (black circle).

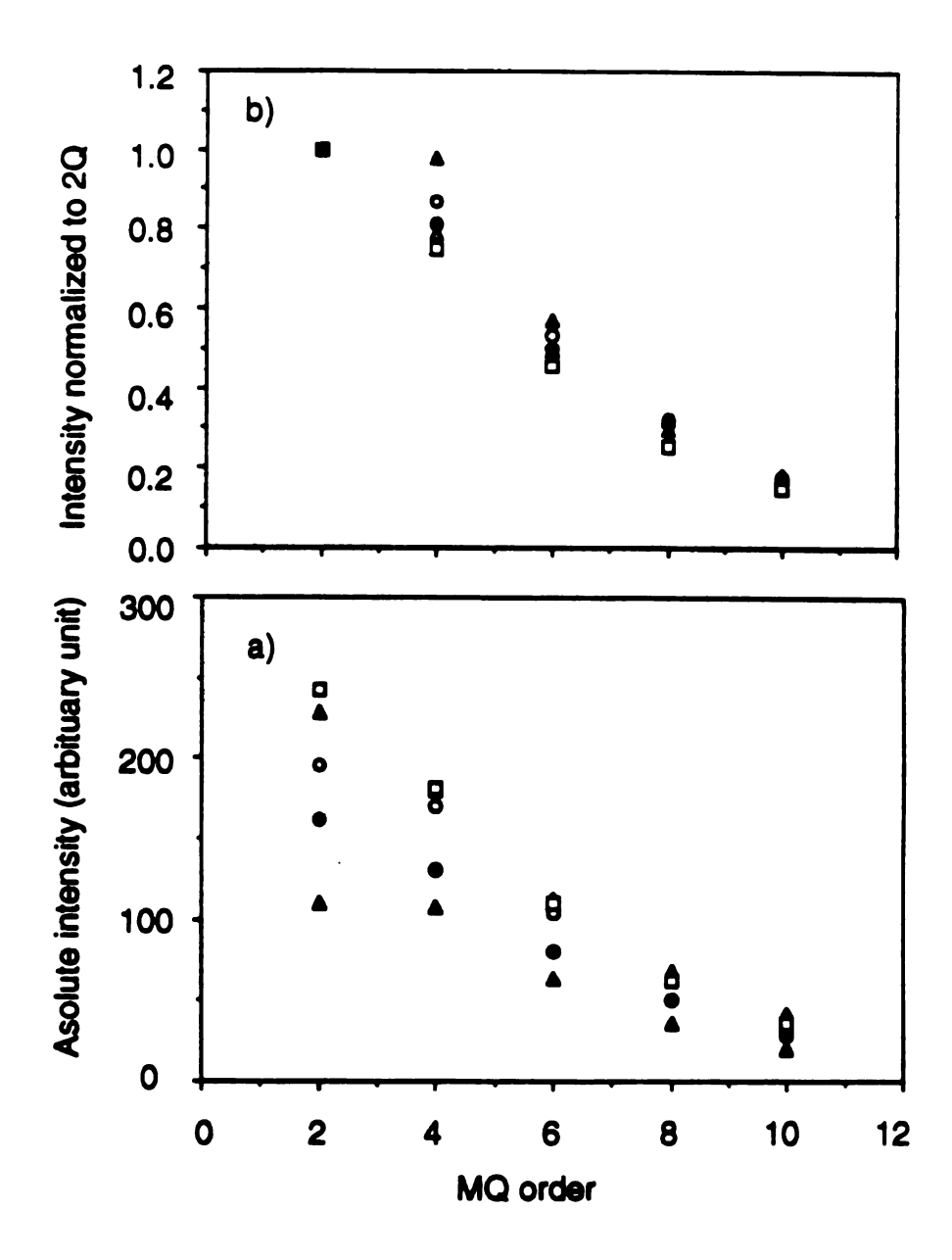


Figure II-22. Intensities of the 1H PI NMR MQ order of HAP-M for various resonance offsets using a preparation time of 1872 μ s. a) Intensities with the same vertical scale. b) Intensities normalized to 2-Q intensity. On resonance (open square), 1 ppm off resonance (open triangle), 2 ppm off resonance (open circle), -1 ppm off resonance (black triangle), and -2 ppm off resonance (black circle).

those obtained off resonance to the upfield side, but are stronger for the 2 and 4 quantum coherences, weaker for the 8 and 10 quantum coherences than those obtained off resonance to the downfield side. It is difficult to obtain an effective size fitted by using a Gaussian function from the intensity profile for an off-resonance transmitter offset at longer preparation times. Thus, the effective sizes obtained using Gaussian function with different resonance offsets are significantly different from those obtained on-resonance, due to the distortions of the MQ peaks. Such resonance offset effects complicate the interpretation of MQ dynamics.

B. ¹H Multiple-Quantum NMR of Hydroxyapatite and Fluorohydroxyapatite Samples

The normalized intensities of the various orders of MQ coherence as a function of preparation time τ for the various apatite samples are plotted in Figures II-23a, b, c, and d. Figure II-23a shows that the normalized intensity of the zero-quantum coherence of HAP-M decreases, and that of the 2-quantum coherence increases first and then decreases with increasing preparation time; the higher quantum orders steadily grow within this experimental range of preparation times. The normalized intensity of the zero-quantum coherence of HAP-N in Fig. II-23b shows a different behavior compared to that of HAP-M; it decreases slightly at earlier preparation times and levels off at longer preparation times. Although the normalized intensities of the high quantum orders of the HAP-N are less than those of HAP-M, they present the same behavior with respect to increasing preparation time as HAP-M. The normalized intensities of the zero-quantum coherence of FOHAP x=0.24 and x=0.41 shown in Figure II-23c and d show a slight variation, and are higher than those of HAP-M and HAP-N.

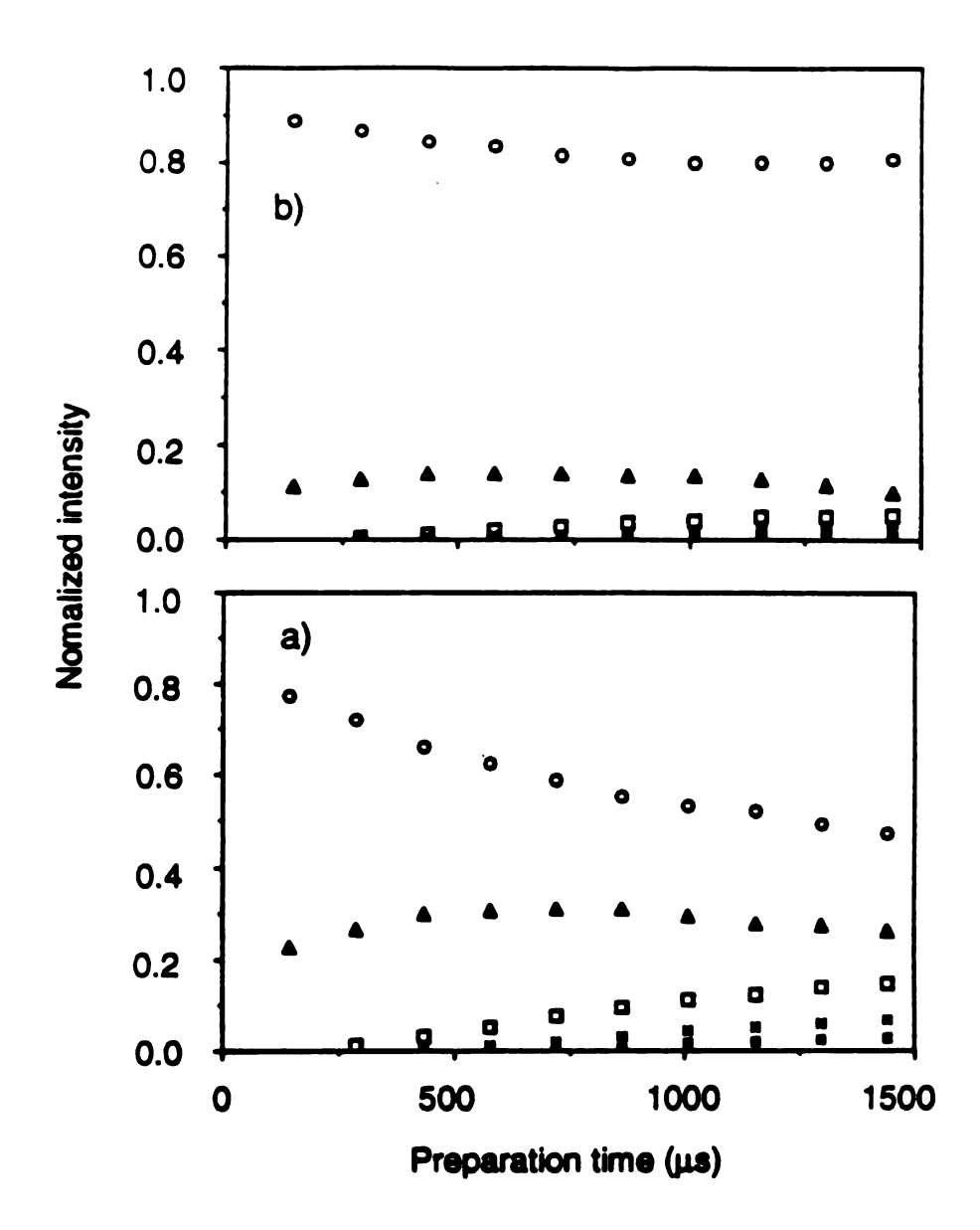
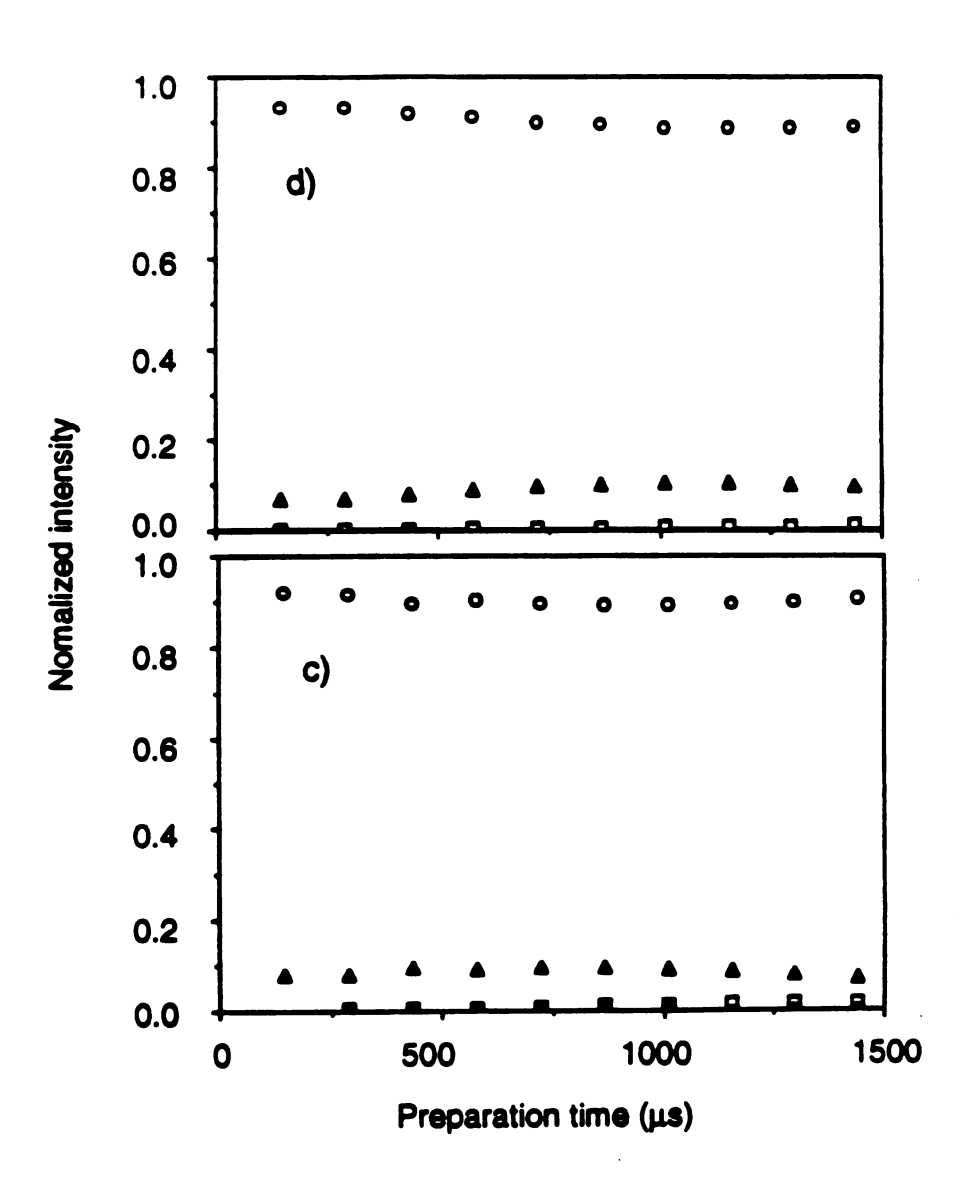


Figure II-23. The normalized intensities of even-order MQ coherences of apatite samples as a function of preparation time. a) HAP-M; b) HAP-N; c) FOHAP x=0.24; d) FOHAP x=0.41. 0Q (open circle), 2Q (open triangle), 4Q (open square) 6Q (open circle), and 8Q (black square).



The effective size obtained from fitting MQ intensities to a Gaussian is useful for studying MQ dynamics. Figure II-26 shows the experimental effective sizes N vs. preparation time for HAP-M and theoretically calculated curves for 1-D and 2-D growth using the incremental shell model. The experimental plot is linear in its early preparation time development, only deviating upward at longer preparation time (where one expects the weaker inter-chain dipolar couplings to become more influential). The solid line represents the calculated curve for a one dimensional chains of ¹H spins in hydroxyapatite. The value of n_n in the incremental shell model was chosen to be 1, since there is only a single uncorrelated spin adjacent to each spin at the coherence boundary. The value of n_s (related to a system's dimensionality) was set to 2, representing the total number of adjacent spins outside of the coherence (the two "end spins" in a linear chain). The dipolar coupling D_{12} between a pair of nuclei is rewritten from Eq I-50 in the Part I as

$$D_{12} = (\gamma^2 h)(1 - 3\cos^2\theta_{12})/2r_{12}^3 \qquad \text{(in Hz)}. \tag{II-77}$$

For two neighboring intra-chain protons 344 pm apart (the distance in hydroxyapatite⁵⁹) and parallel to the external field, D_{12} = 2.957 kHz, which is 1/3 of the Pake doublet splitting that would be obtained in a ¹H spectrum. We used in the simulation an average D_{12} , 1.32 kHz, whose value is the root mean square value of D_{12} over all powder orientations. Since the value of $P_2(\cos\theta_{12})$, $(1-3\cos^2\theta_{12})$, is averaged out over all orientations but that of $P_2(\cos\theta)^2$ is not, an average D_{12} is obtained from the square root of an average D_{12}^2 . This follows the approach used by Levy and Gleason.³⁶ For a 1-D system, a more reasonable approach is to sum the powder-weighted responses foe each orientation of the 1-D chain. The experimental slope is three times larger than the predicted slope. The dashed line shown in Fig. II-24 is the calculated curve for a two dimensional

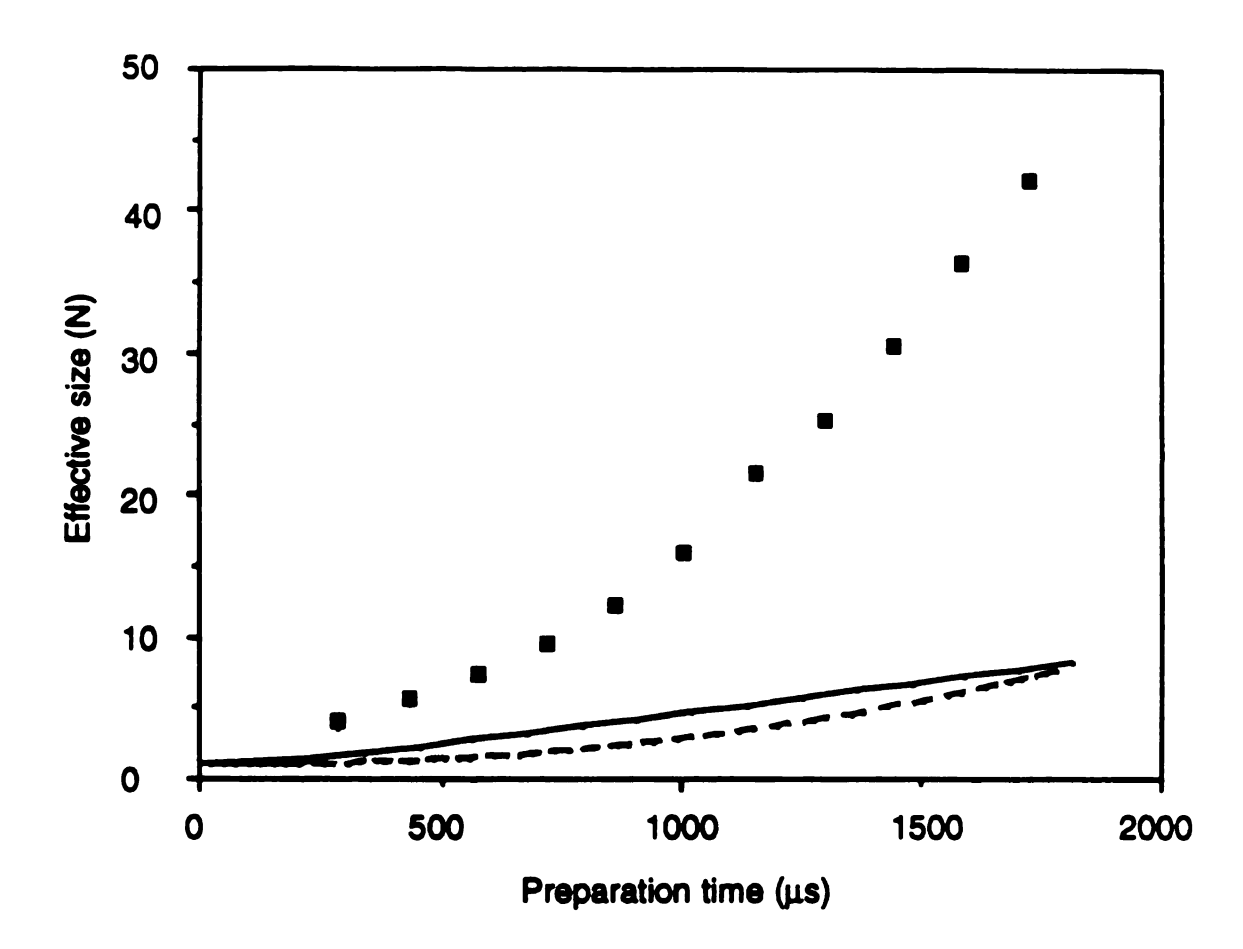


Figure II-24. Effective size N versus MQ preparation time for HAP-M. The solid line is a theoretical calculation using the incremental shell model for a one-dimensional spin system with the appropriate dipolar coupling strength and bo adjustable parameters (see text). The theoretical calculation of a two-dimensional system is represented as the dashed line.

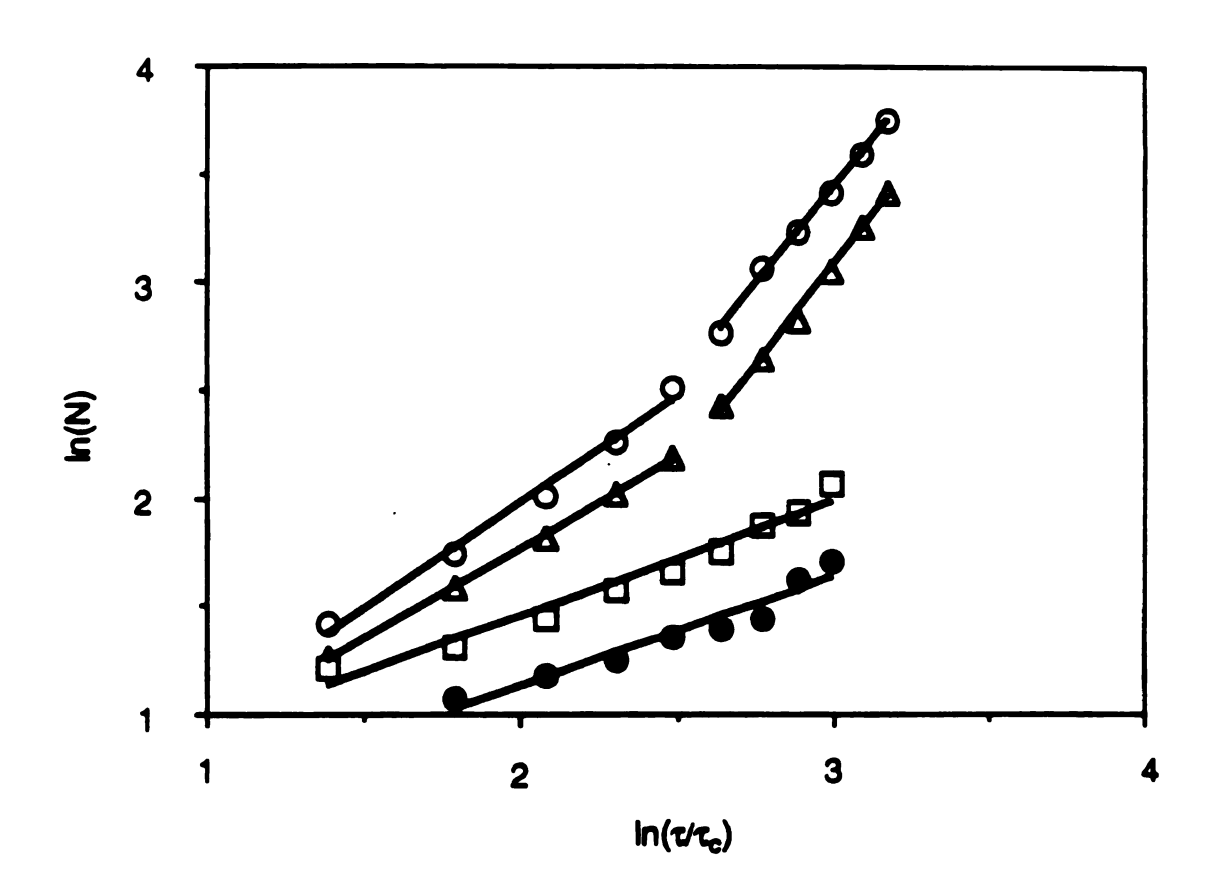


Figure II-25. ln(N) vs. $ln(\tau/\tau_c)$ for all of the samples of hydroxyapatite and fluorohydroxyapatite. Solid lines indicate the slopes of data points that are obtained using least squares fitting. HAP-M (open circle), HAP-N (open triangle), FOHAP x=0.24 (open square), and FOHAP x=0.41 (black circle).

system assumed to consist of the six nearest protons in adjoining columns in the hydroxyapatite structure. The calculation was performed by using an inter-chain nearest-neighbor powder-average dipolar coupling D_{12} of 64 Hz. The value of n_n was set to 6, the number of planar neighbors, and n_s was chosen to be $4M^{1/2}$.

The effective size N grows as some power of the preparation time τ ($N \propto \tau^{\alpha}$). It is convenient to plot ln(N) versus ln(τ/τ_c) to obtain the growth exponent α as shown in Figure II-25, where τ_c is the basic cycle time. The growth exponent for effective size vs. preparation time is equal to the slope of this plot. The MQ data for HAP-M and HAP-N show bi-exponential characteristics. The slopes of HAP-M and HAP-N for short preparation times (shorter than 864 μ s) are 0.98 (correlation coefficient = 0.988) and 0.83 (correlation coefficient = 0.998), and those for long preparation times (longer than 1008 μ s) are 1.78 and 1.82 respectively. FOHAP x=0.24 and FOHAP x=0.41 have single exponential characters. The slopes for FOHAP x=0.24 and FOHAP x=0.41 are 0.54 (correlation coefficient = 0.963) and 0.50 (correlation coefficient = 0.936) respectively.

The decays of the absolute intensity of the sum of all multiple-quantum coherences of the apatite samples are shown in Figure II-26a as a function of preparation times. The decay function corresponding to irreversible relaxation can be assumed to be exponential:

$$I(\tau) \propto \exp(-\tau/T_d)$$
. (II-78)

The different relaxation times T_d of the different MQ coherences can be distinguished by taking the logarithm of Eq. II-78. Figure II-26b shows a plot of $\ln(I(\tau))$ vs. the preparation time τ . Since the T_d relaxation time is the inverse of the slope in Figure II-26b, we have offset the intercept in order to see the slope more clearly. The T_d relaxation times of HAP-M, HAP-N, FOHAP x=0.24, and FOHAP

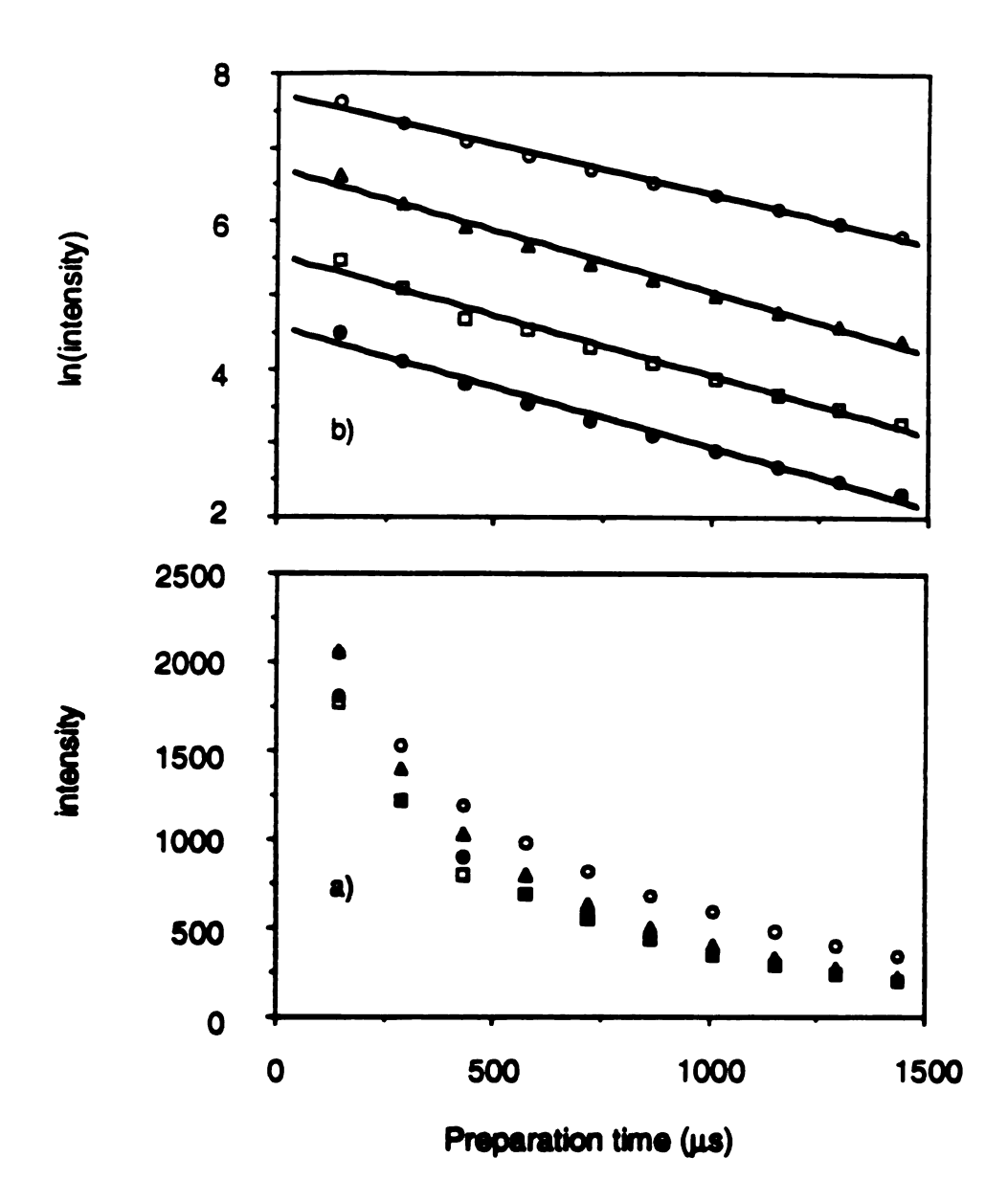


Figure II-26. Decay of absolute MQ coherence intensity of apatites. HAP-M (open circle), HAP-N (open triangle), FOHAP x=0.24 (open square), and FOHAP x=0.41 (black circle). a) Intensity vs. Preparation time. b) In(intensity) vs. preparation time, arbitrarily offset in the vertical direction.

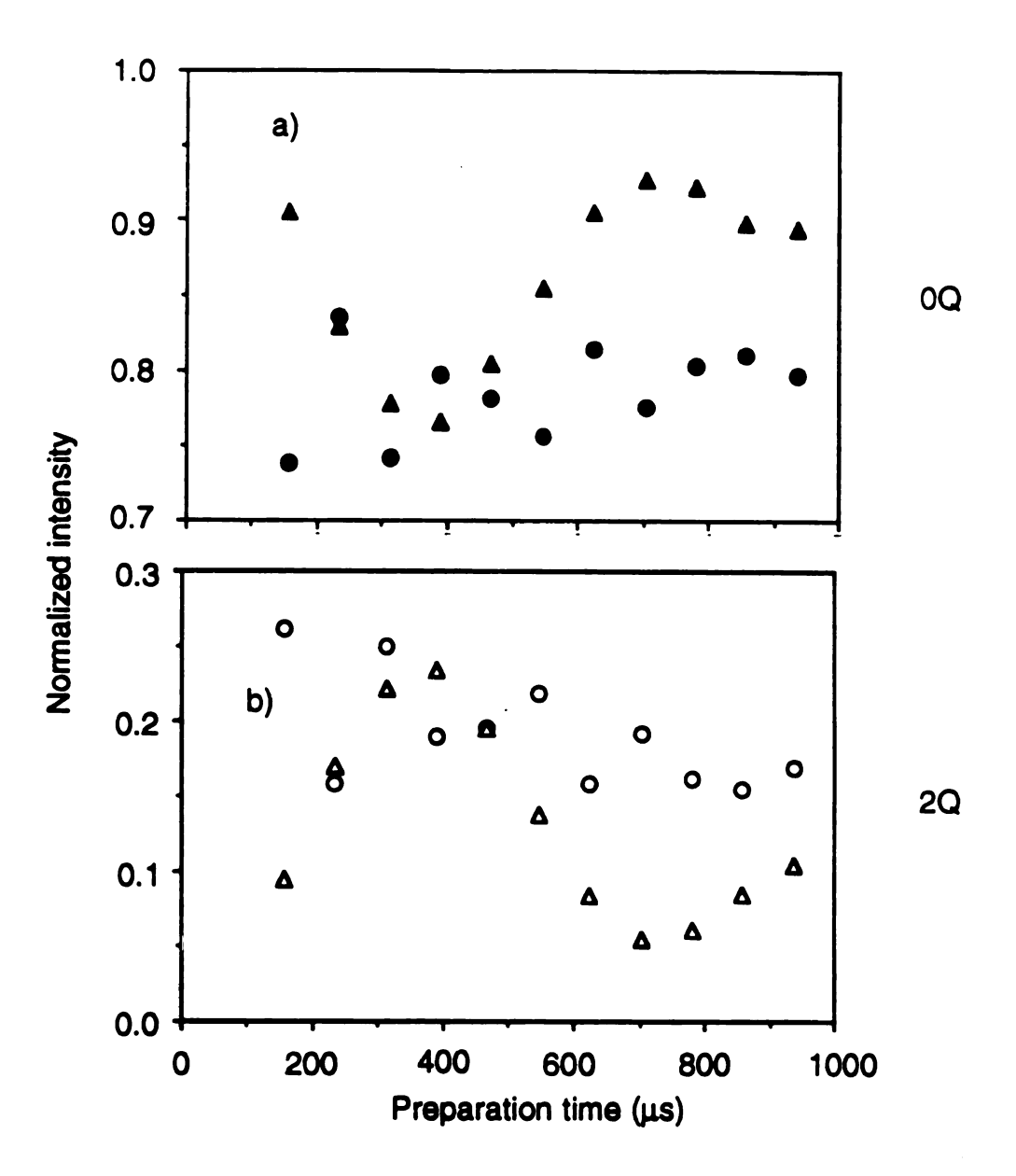


Figure II-27. The normalized intensities of 0Q and 2Q coherences of a single crystal mineral sample of FAP vs. preparation time at two orientations with respect to the external magnetic field. a) 0Q at 90° (black circle) and 0Q at 62° (black triangle). b) 2Q at 90° (open circle) and 2Q at 62° (open triangle).

Figure II-28. In(absolute intensity of MQ orders) vs. preparation time of single-crystal fluorapatite at two different orientations. 90° orientation (open circle) and 62° orientation (open triangle).

x=0.41 are 742, 601, 615, and 610 μ s respectively.

C. ¹⁹F Multiple-Quantum NMR of a Single Crystal of Fluorapatite

Figures II-27a and b show the intensity of the zero-quantum and two-quantum coherences of a single crystal FAP at two orientations (c axis making the angles 62° and 90° with respect to the external magnetic field). Unlike a powder sample (see Fig. II-23), an oscillatory behavior is observed for the zero and two quantum intensities. The frequency of the oscillations of the MQ coherences for single-crystal FAP is proportional to the dipolar coupling. The dipolar coupling intra-chain of single-crystal FAP at 90° is approximately 2.95 times larger than that at 62°.

The logarithm of the absolute total multiple-quantum intensity for the single-crystal FAP sample at two orientations vs. preparation time τ is shown in Figure II-28. The T_d relaxation times of this single-crystal mineral FAP are 694 μ s and 645 μ s at 62° and 90° respectively.

5. DISCUSSION

A. Effect of Resonance Offsets in the PI-MQ NMR Pulse Sequence on the Formation of Multiple-Quantum Coherence

Figures II-18, 21, and 22 show the effect of a resonance offset on multiplequantum coherences. We can give a possible explanation for this effect. In the rotating frame, when only the static magnetic field is present, the effective field is represented by the vector equation

$$\vec{H}_{eff} = \vec{H}_0 - \vec{\omega}/\gamma \tag{II-79}$$

where \vec{H}_0 is the vector of the main static magnetic field and the magnitude of $\vec{\omega}$ is the angular frequency of rotation of the unit vector at rf carrier frequency. We

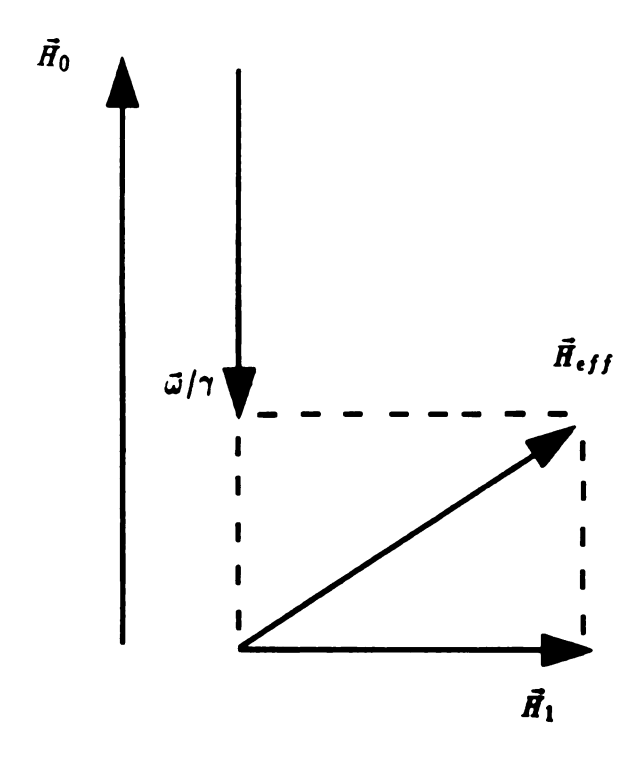


Figure II-29. The effective magnetic field \vec{H}_{eff} in the rotating frame in the presence of an applied rf field \vec{H}_1 . The effective magnetic field is the vector sum of the applied static field \vec{H}_0 , the fictitious field $\vec{\omega}/\gamma$, and the rf field \vec{H}_1 .

can express the effective field in the rotating frame in the presence of an rf pulse as the vector sum of $\vec{H}_0 - \vec{\omega}/\gamma$ and \vec{H}_1 (see Figure II-29)

$$\vec{H}_{eff} = \left(\vec{H}_0 - \vec{\omega}/\gamma\right) + \vec{H}_1$$
 (II-80)

where $ec{H}_1$ is the radiofrequency field. The magnitude of the effective field is represented by

$$H_{eff} = \left[(H_0 - \omega/\gamma)^2 + H_1^2 \right]^{1/2}$$

$$= (1/\gamma) \left[(\gamma H_0 - \omega)^2 + (\gamma H_1)^2 \right]^{1/2}$$

$$= (1/\gamma) \left[(\omega_0 - \omega)^2 + \omega_1^2 \right]^{1/2}$$
(II-81)

where $\omega_0 - \omega$ is a resonance offset frequency and $\omega_1 = -\gamma_I H_I$ is the radiofrequency field strength. The Hamiltonian of the radiofrequency along the x direction in a frame rotating at the carrier frequency can be represented by

$$\mathcal{H}_{rf} = -\gamma_I H_1 I_z. \tag{II-82}$$

A 90° pulse along the x direction flips the initial magnetization ($M_z = \gamma I_z$) into the y direction ($M_z = \gamma I_y$) on-resonance. However, the magnetization of off-resonance peaks after a 90° pulse is not in the y direction. As mentioned in the background section, the average dipolar Hamiltonian generated by the 8-pulse cycle with the proper delays (PI-MQ pulse sequence shown in Fig. II-4) is a driving force for creating the multiple-quantum coherences. The effectiveness of the average Hamiltonian is determined by the preciseness of the 90° pulse length. An increase of the resonance offset results in an increase of the difference between \vec{H}_{eff} and \vec{H}_1 (an imperfect 90° pulse when an off-resonance).

The system evolves under the influence of the internal Hamiltonian alone after the 90° pulse. The time development of the system in the absence of relaxation is represented by

$$\rho(t) = exp(-iH_{int}t)I_y exp(iH_{int}t). \tag{II-83}$$

The average double-quantum Hamiltonian H_{yx} is used instead of the internal Hamiltonian H_{int} in MQ NMR experiments. There is no resonance-offset correction to zero order for the average double-quantum Hamiltonian used in our experiments, 40 but higher order terms quickly contribute to the resonance-offset effects. Even if the pulses are "hard" δ -pulses that perfectly rotate I_z to I_y for all offsets, the existence of the off-resonance term $\Delta \omega I_z$ changes the time development of the density operator in Eq. II-83, due to the resonace-offset correction in some order of the average double-quantum Hamiltonian as time increases.

The extent to which resonance-offset effects influence the MQ spectrum is sample dependent. The 1 H CSA of hexamethylbenzene is nearly zero due to the fast reorientation of the methyl groups, and that of hydroxyapatite is estimated to be roughly 14 ppm. 74 The placement of the transmitter carrier frequency away from the isotropic chemical shift for hexamethylbenzene shows a severe destructive interference of the multiple-quantum coherences for a preparation time of 504 μ s. The 2-quantum order seems to be more influenced by resonance offset effects than are the higher orders. As resonance offsets increase, the intensities of the 2-Q coherence become weaker and more out-of-phase. To illustrate the magnitude of off-resonance error in the 1 H MQ spectrum of powdered HAP-M, the MQ spectra of HAP-M was recorded with the transmitter positioned at 2ppm (800Hz) upfield, and in a separate experiment 2 ppm downfield, of the highest position in the pattern. For a preparation time of 862 μ s, the MQ spectra show no distortion, but for a preparation time of 1872 μ s the spectra were distorted due to the cumulative effect of off-resonance terms.

B. Dimensionality Effects in the Multiple-Quantum NMR of Hydroxyapatite

Different samples show different growth curves of MQ coherences with in-

creasing preparation time. However, it has been demonstrated by Gleason et. al. that when the preparation time is scaled by the square root of the second moments of the individual samples, samples having the same dimensionality show universal MQ growth curves.³⁶ Therefore, the growth of MQ coherences is related to the dimensionality.36 The study of dimensionality using MQ NMR has been performed with two- and three-dimensional spin systems. Hydroxyapatite is a good model for studying one-dimensional spin systems since it has linear chains of uniformlyspaced proton spins, fairly widely separated from each other. The growth of MQ coherences for HAP-M at preparation times up to 864 μ s in Fig. II-24 is linear as is the calculated one-dimensional growth in the incremental shell model. In qualitative agreement with the calculation for two dimensional growth, an upward curvature in the experimental curve at longer preparation times may reflect growth to other columns of spins. Lacelle⁵³ has discussed the possible significance of the different growth exponents observed for various spin systems. The growth exponents of 1- and 2-dimensional spin systems obtained from the incremental shell model prediction after the initial induction time are 1.00 and 2.05 respectively. The bi-exponential character of the curve for HAP-M shown in Figure II-27 suggests a growth of MQ coherences with a change in the dimensionality. The growth exponents of HAP-M (0.98 for preparation times shorter than 864 μ s and 1.78 for times longer than 1004 μ s), which are close to those predicted by the incremental shell model for 1- and 2-dimensional growth, show a 1-dimensional character at short preparation times arising from intra-chain dipolar couplings, and a higher slope at longer preparation times arising from the more 2-dimensional spin system corresponding to inter-chain dipolar couplings. Of course, the representation of the inter-chain growth as 2-dimensional is inexact, since it has some three-dimensional character. Further more, when the intensities of the orders of HAP-M are fit to an exponential, the fit is somewhat improved over a Gausian fit, and the parameter characterizing the exponential fit is observed to increase linearly at all preparation time. Thus, the effects of different dimensionalities will require further study, possibly by using powdered fluorapatite samples.

C. One-Dimensional Cluster Model

Clustered samples give rise to a strong intensity of the zero quantum peak compared to non-clustered samples.⁷⁵ From Figure II-23, the strong normalized zero quantum intensities of HAP-N, FOHAP x=0.24 and FOHAP x=0.41 compared to that of HAP-M qualitatively demonstrate the existence of vacancies and/or fluorine ion substitutions that make clusters in a one-dimensional chain. The growth exponent of an infinite 1-dimensional chain theoretically predicted by the incremental shell model is 1.00. The growth exponent of HAP-N at early preparation times (0.83) clearly shows evidence for a hydroxyl deficiency. The lesser slopes of FOHAP with increasing mole fraction of fluoride ion in Fig. II-25 indicate that the FOHAP samples having higher mole fractions of fluorine contain higher defect densities. Thus, MQ NMR shows evidence of the interruption of hydroxyl groups in apatite samples.

Figure II-30 shows hydroxyl groups in an apatite chain segmented by vacancies and/or fluorine ions. The run number of a group of hydroxyls is defined as the number of contiguous hydroxyl groups between two "defects" on either side, which can be either vacancies or fluoride ions. Since MQ coherences are created by the homonuclear dipolar interaction, the existence of vacancies and/or fluoride ions between hydroxyl groups in an apatite chain hinders the propagation of MQ coherences. In order to compare experimental MQ spectra with calculated MQ

spectra for given defect densities by the statistical model, we assume the following:

- 1. defects are randomly distributed (ideal solid solution);
- 2. MQ coherence growth occurs only along the linear chains;
- 3. MQ coherence do not grow across vacancies or fluorine atom substitutions;
- 4. MQ results for stoichiometric hydroxyapatite (HAP-M) yield effective size for each preparation time τ .

Since the sum of the intensity of all MQ orders in the absence of decay of MQ coherences is the same regardless of preparation times, it can be normalized to one. The intensities of MQ orders, $I_n(\tau)$, can be represented using the normalized factor⁷⁴ from Eq. II-39 as

$$I_{n}(\tau) = CZ_{n}/4^{N} \tag{II-84}$$

where C is equal to 1 for a non-selective experiment and 2 for an even-selective experiment. Since the intensity of each order of MQ coherence depends on the run number and the mole fraction of spins present in a given run number, the intensity of each order of coherence for a defect-containing sample can be calculated by summing over the contribution from each run number combined with a Gaussian distribution, as given by the following equation

$$I(n,\tau) = \sum_{r=2}^{6} \chi_r {2N_r \choose N_{r-n}} (4^{N_r})^{-1} + \qquad \text{for } N_r \le 6$$

$$\sum_{r=7}^{\infty} \chi_r (N_r \pi)^{-1/2} exp(-n^2/N_r) \qquad \text{for } N_r > 7.$$
(II-85)

where χ_r is the mole fraction of spins in a run number, and N_r is set equal to the run number for run lengths up to the effective size. The value of N_r is set equal to the run number when the run number is less than effective size; otherwise, N_r is set equal to the effective size.

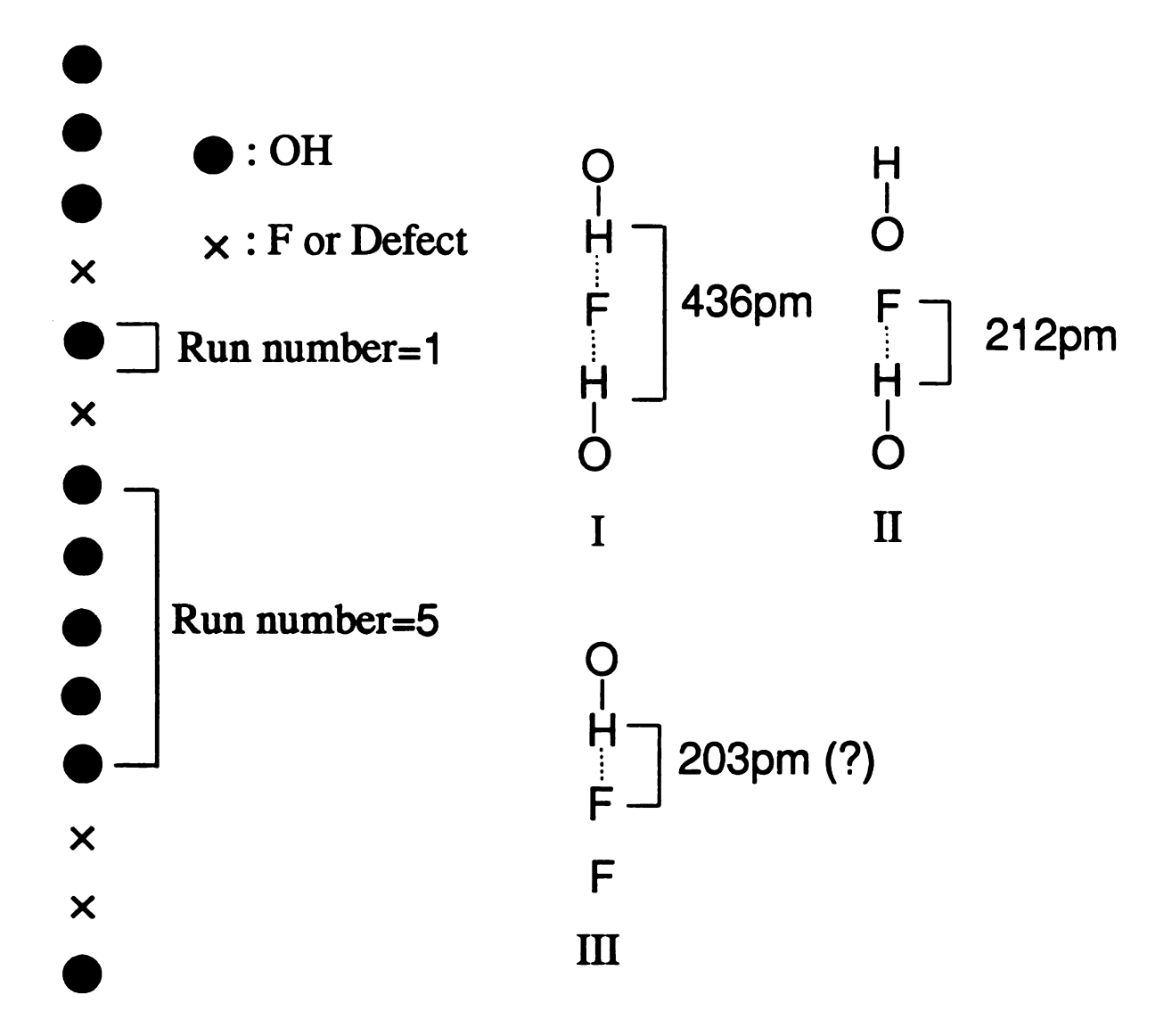


Figure II-30. Arrangement of hydroxyl groups separated by vacancies and/or fluoride ion substitutions in apatite samples. The distance between hydroxyl groups and fluoride ions has been obtained by NMR studies.^{76,77} The substitution of fluoride ions gives three configurations (I-III) along the crystallographic c axis in FOHAP. The dotted lines denote hydrogen bonds.

D. Estimation of Defect Densities Using the 1-D Cluster Model.

Even if the MQ intensities of experimental data obey a Gaussian distribution perfectly, the theoretical MQ intensities of defect-containing samples obtained from Eq. II-85 may not be fitted very well by a Gaussian distribution due to the summing of contributions by different run numbers. Therefore, the comparison between theoretical and experimental 4Q/2Q intensities for a given preparation time is more relevant than a comparison of effective sizes. Experimentally, since MQ intensities do not correspond to a Gaussian distribution exactly due to strong intensities of the higher order peaks, we recalculated the effective size of HAP-M using the 4Q/2Q intensity at each preparation time. Since the contribution of MQ intensities from a 2-D spin system complicates the calculation of defect density at longer preparation times, we use MQ data from the linear portion of the curve corresponding to 1-dimensional growth in Fig. II-24. The mole fraction of the run numbers in a 1-dimensional chain can be calculated by percolation theory.⁷⁸ Figure II-31 shows run number distributions for various defect densities. The center of mass of a given run number distribution moves to a larger run number value as the defect ratio decreases.

7.0

The result of calculations based on this 1-D cluster model and experimental data is shown in Figure II-32. The calculation program is given in Appendix C. The HAP-N from MQ data are closer to the curve calculated for an 8% defect density (that obtained from ¹H MAS-NMR) than o that calculated for a 19% defect density (that obtained from IR). The experimental curves for the FOHAP samples are lower than the calculated curves. There are several possible explanations for the deviation between the calculated and experimental curves for FOHAP samples. First, hydroxyl vacancies exist in the one dimensional chains of precipitated

apatites (compare the difference between HAP-M and HAP-N). These vacancies in the hydroxyl chains can create additional defects in addition to those created by fluoride substitutions, and could explain the discrepancy between the calculated and experimental curves of FOHAP. The experimental curve of the FOHAP x=0.24 sample is close to the theoretical curve for a 41% defect density corresponding to a 22% hydroxyl deficiency. Secondly, if fluoride ions substitute randomly for hydroxyl groups, the molar ratio of the configuration III to configurations I or II shown in Figure II-30 for FOHAP x=0.24 is 0.32. Yesinowski et. al. have shown that the peak arising from the configuration III is not detected with ¹H MAS-NMR.⁶⁹ If configurations I and II are more preferable than configuration III, the decrease of the number of fluorine ions in a row increases the mole fraction of small run number. Therefore, non-random substitutions of fluoride ions in FOHAP can result in the lower experimental intensity compared to the calculated one. Thirdly, the eight-pulse MQ sequence for solids shown in Fig. II-6 ideally eliminates heteronuclear dipolar couplings and J couplings of ¹H and ¹⁹F.⁷⁵ In these experiments, we have given applied the MQ pulse sequence at the proton frequency. The effectiveness of the decoupling is determined by the basic cycle time, the time scale of mutual spin flips of the irradiated spin system T_{2H} and the strength of the heteronuclear dipolar coupling between ¹H and ¹⁹F. A heteronuclear dipolar coupling between two different spin 1/2 nuclei is represented by

$$D_{IS} = (\gamma_I \gamma_s h)(1 - 3\cos^2 \theta_{12})/3r_{12}^3.$$
 (II-86)

The ¹H-¹⁹F dipole coupling in configuration I parallel to the external magnetic field is equal to 7.27 kHz. The isotropic chemical shift of hydroxyl groups not adjacent to a fluoride ion is 0.2 ppm and those of configurations I and II are 1.2 ppm and

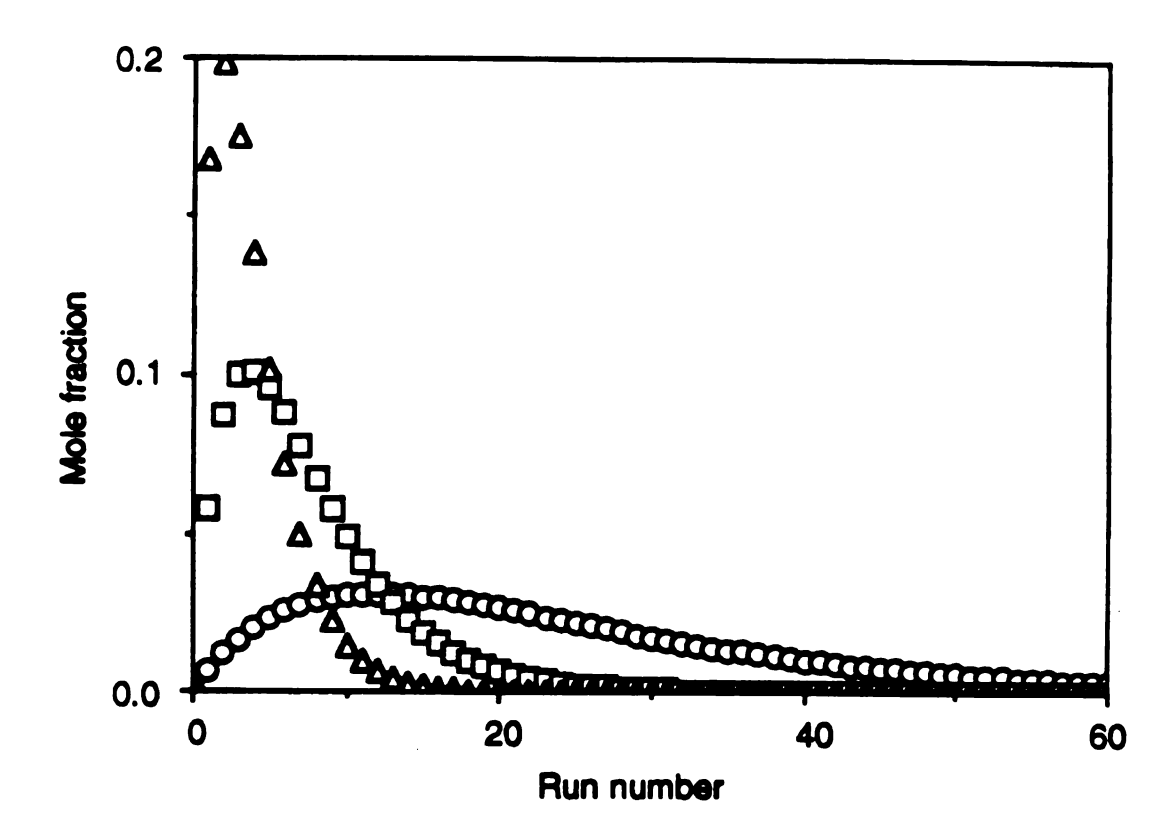


Figure II-31. Run number distributions for various defect densities in a one-dimensional chain. The mole fraction of spins in a given run number is calculated by percolation theory⁷⁸; 8% (open circle), 24% (open square), and 41%(open triangle).

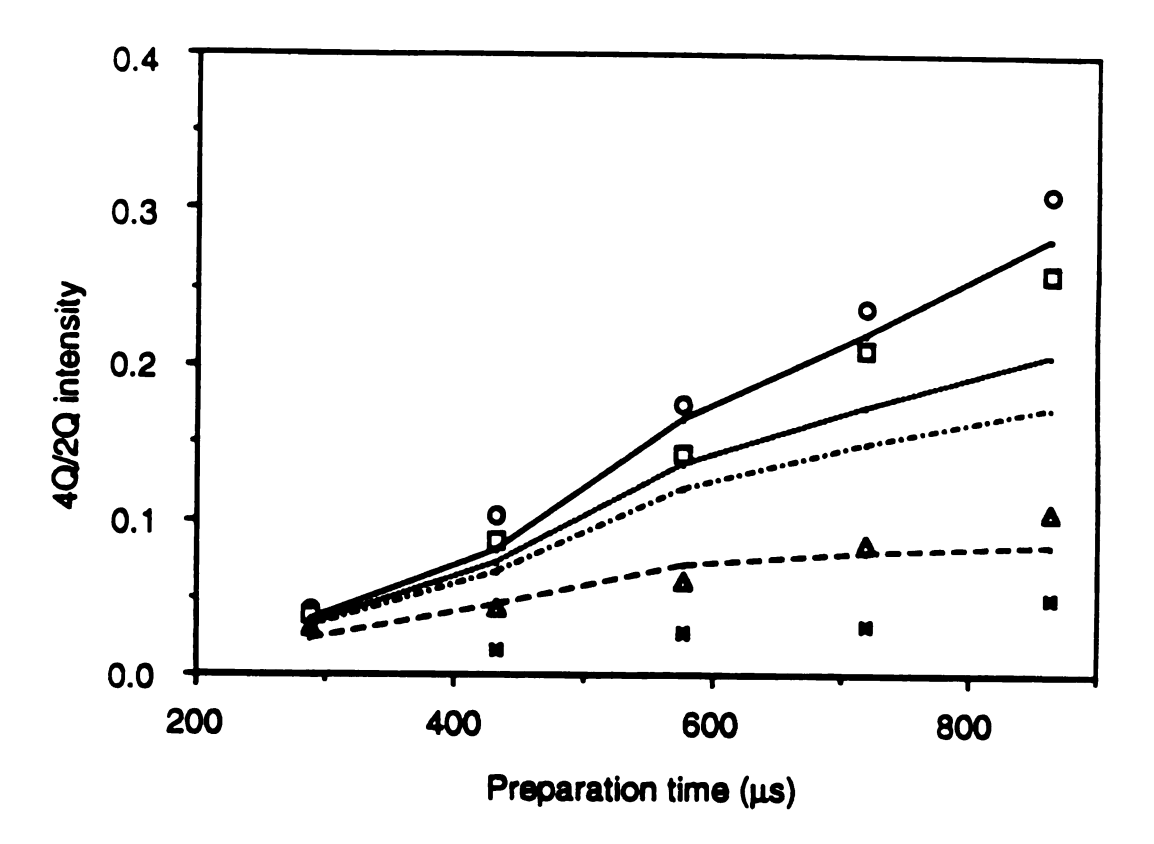


Figure II-32. 1-D cluster model of MQ growth for various defect densities in apatite, compared to experimental data. Lines for the various defect densities are calculated using Eq. II-84. From top to bottom, lines correspond to 8%, 19%, 24%, and 41% defect densities. HAP-M (open circle), HAP-N (open square), FOHAP x=0.24 (open triangle), and FOHAP x=0.41 (crosses).

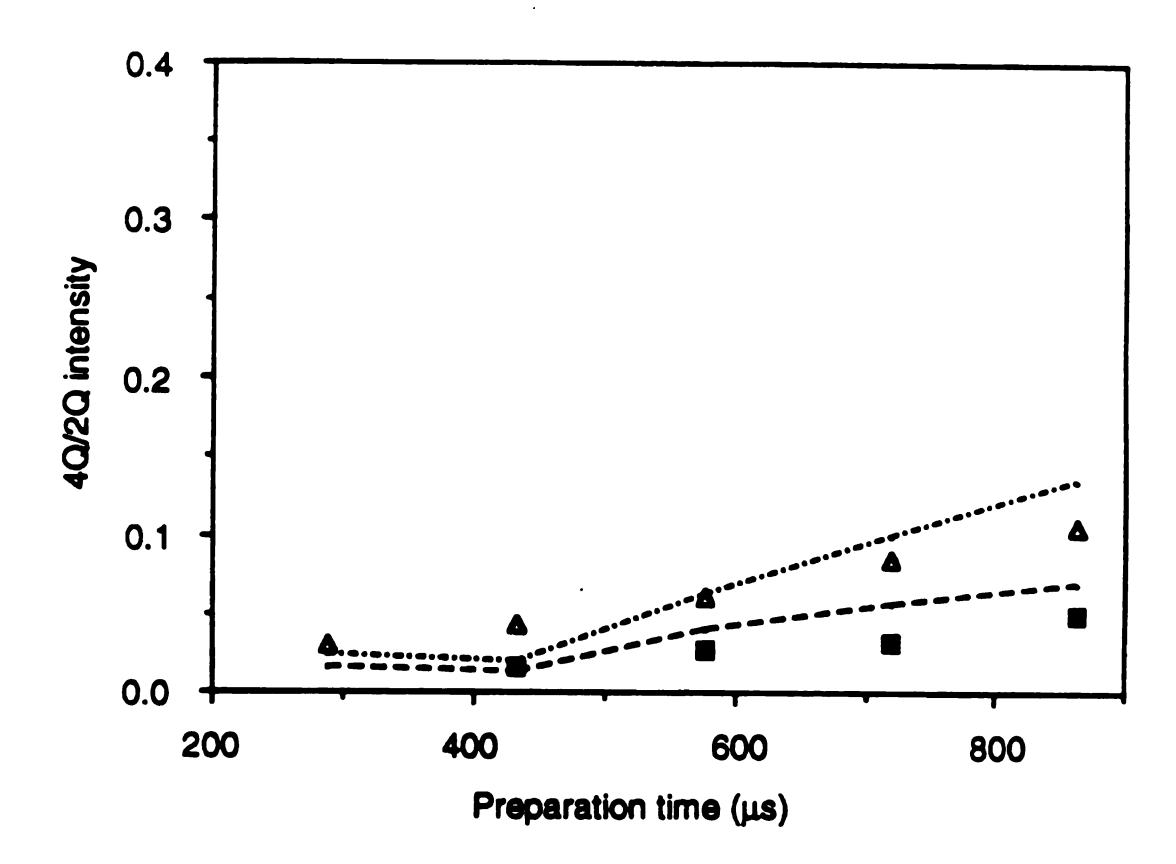


Figure II-33. Comparison between experimental 4Q/2Q intensities and calculated 4Q/2Q intensities for FOHAP samples after excluding the two hydroxyl groups adjacent to fluoride ion. From top to bottom, lines correspond to 24% and 41%. FOHAP x=0.24 (open triangle) and FOHAP x=0.41 (black square).

1.5 ppm respectively.⁶⁹ However, the proton adjacent to a fluorine atom will be split into a Pake doublet. This splitting produces a resonance for these protons of typically several kHz, sufficient to prevent them from effectively participating in normal MQ coherence growth. Thus, we assume that the protons adjacent to a fluorine atoms do not participate in MQ coherences. Figure II-33 shows a recalculation of the 4Q/2Q intensities for 24 % and 41 % defect densities using Eq. II-85, when terminal OH···F groups in a run are excluded. The experimental 4Q/2Q intensities of FOHAP x=0.24 and FOHAP x=0.41 in Fig. II-33 are closer to the calculated 4Q/2Q intensities than those in Fig. II-32, suggesting that this resonance offset effect may be at least partially responsible for the initial discrepancy. Finally, a different coherence in the decay time of different run numbers of spins and/or the different MQ order might result in a difference between calculated and experimental 4Q/2Q intensities. However, the logarithmic plots in Figure II-26b do not show two different slopes for a the decay time within experimental limits, which means that different MQ coherences do not have different decay times.

D. ¹⁹F Multiple-Quantum NMR Dynamics of Single Crystal Fluorapatite.

The oscillatory behavior of MQ dynamics in a liquid crystal has been previously shown experimentally and theoretically for finite spin systems.^{51,56} Munowitz has theoretically predicted such oscillations for small oriented linear arrays of uniformly spaced spins under the Hamiltonian \mathcal{H}_{zz} where

$$\mathcal{H}_{zz} = 1/3 \sum_{j < k} D_{jk} (I_{zj} I_{xk} + I_{xj} I_{zk}).$$
 (II-87)

The theoretically predicted oscillations are periodic for two spins but are damped for larger arrays (very small oscillations for arrays of 6 spins).⁵⁰ The oscillatory frequency of the intensities of 1 Q and 2Q coherences for a 2 spin system under

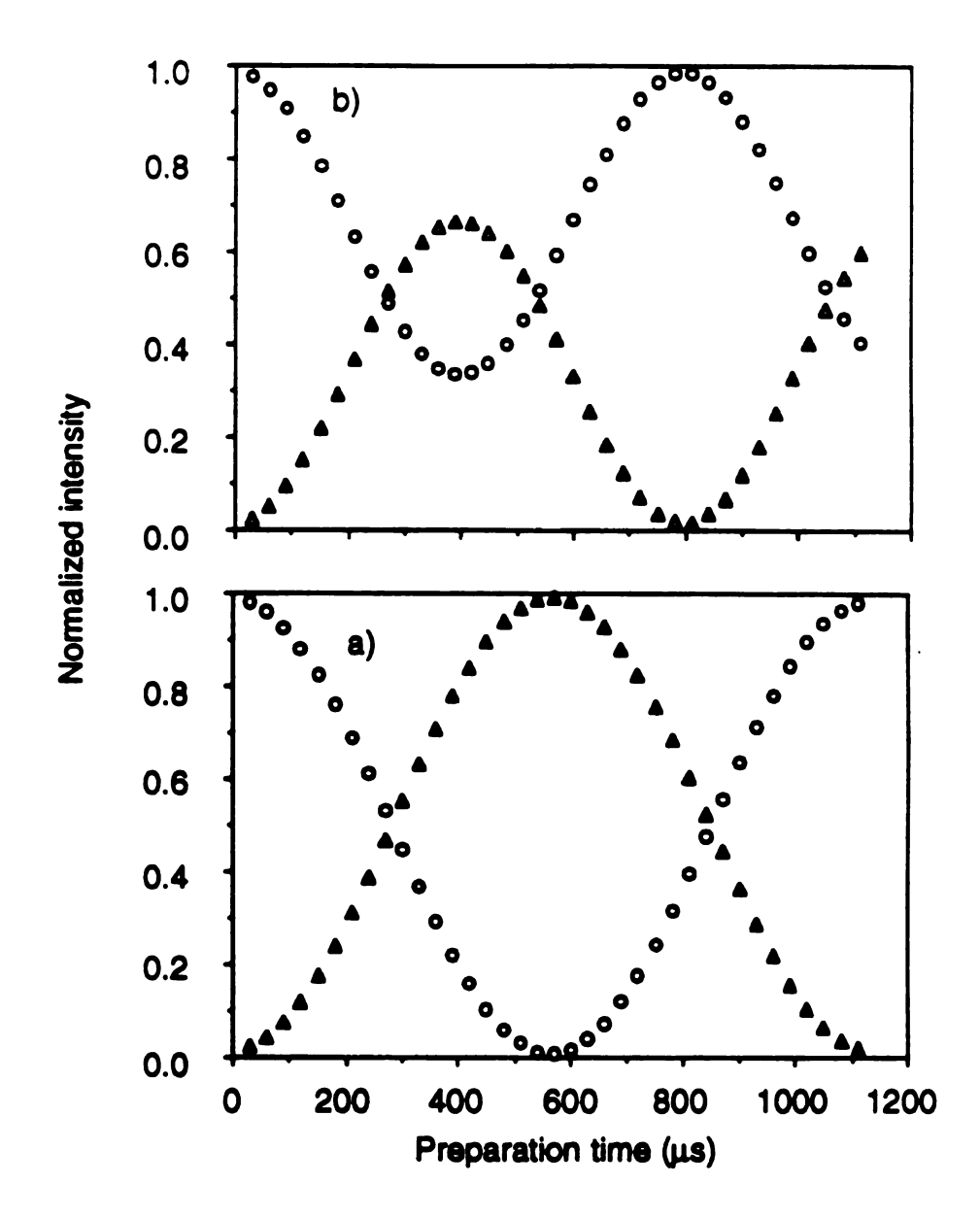
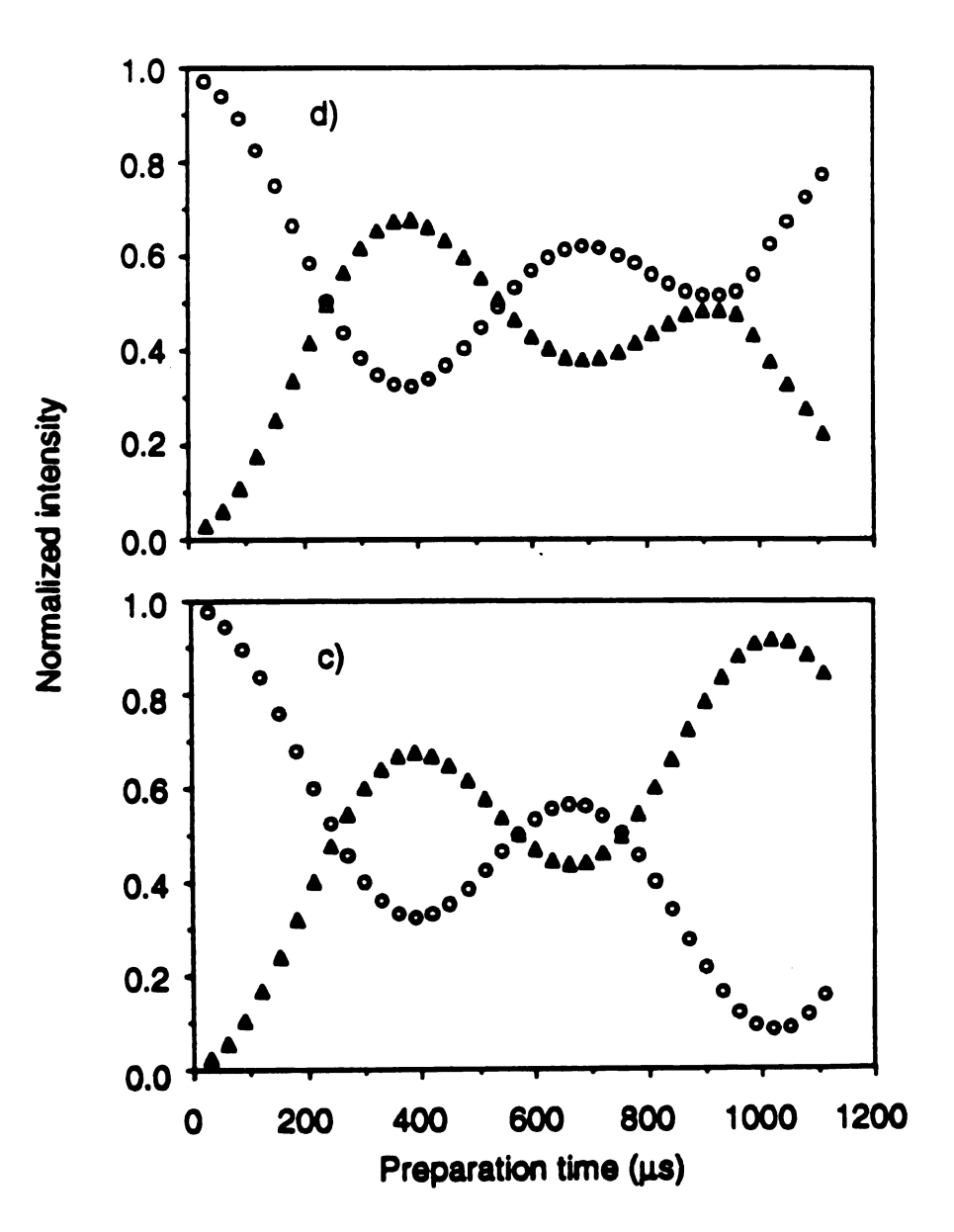


Figure II-34. Simulated MQ dynamics of 2, 3, 4, and 5 spin systems under \mathcal{H}_{yx} for an oriented linear chain using ANTIOPE⁶⁶ (see text). a) 2 spin system; b) 3 spin system; c) 4 spin system; d) 5 spin system. 0Q (open circle) and 2Q (open triangle).



 \mathcal{H}_{zx} is (1/3) D_{12} .

Figure II-34 shows the simulated MQ dynamics for oriented chains of 2, 3, 4, and 5 spin systems under the Hamiltonian \mathcal{H}_{yz} as a function of preparation times using ANTIOPE. ⁶⁶ The distance between nuclei is 344 pm; the same as that in fluorapatite, and a 62° orientation with respect to the external magnetic field was chosen for simulations. The MQ dynamics of the 2 spin system (Fig. II-34a) are both oscillatory and periodic. The dipolar interaction between two spins ($d_{12} = 344$ pm) is 442.6 Hz, and the periodicity of the MQ dynamics for two spin system is 1129.6 μ s [1/(2*442.6 Hz)]. An increase in the size of the spin system results in a apparent disappearance of periodicity in the MQ dynamics. This is likely due to the destructive interference of the many frequencies present when there are a larger number of unequal dipolar couplings present in a spin system: the actual periodicity may occur at time intervals too long to be revealed by the simulation. The MQ dynamics of a 5 spin system (Fig. II-34d) shows the oscillatory behavior, but no apparent periodicity.

The theoretical calculation of MQ dynamics under even different Hamiltonians $(\mathcal{H}_{zz}]$ and \mathcal{H}_{yz} show the periodicity and oscillatory and periodic behavior for both 2 and 3 spin systems. The oscillatory behavior of MQ dynamics in single crystal fluorapatite appears to be damped and periodic. We have no independent measurements of the defect density in this particular crystal of mineral fluorapatite, although mineral fluorapatite generally contain defects caused by substitutions such as hydroxyl and chloride ions. We can attempt to model the observed MQ dynamics of this defect-containing sample somewhat along the lines of the 1-D cluster model previously described. However, the intensities of the various orders will be obtained in a different manner. For each run number, we will use the

intensities of the individual orders of MQ coherence calculated from the ANTIOPE simulation. The overall intensities of a given order n at preparation time τ i given by following expression

$$I(n,\tau) = \sum_{r=2}^{5} \chi_r I_r(n,\tau)$$
 (II-88)

where r refers to the spin system of size r. The obvious limitation of this approach is that run lengths < 5, which are expected to yield high-damped oscillation, are ignored, since no calculations are available. Figure II-35 shows the mole fraction of spins in various run numbers from 1 to 5 and the sum of the mole fraction with different defect densities obtained by using percolation theory. For defect densities larger than 40%, the sum of the mole fraction of spins in runs \le 5 is about 0.8. Therefore, the contribution of runs having more than 5 spins to the MQ dynamics for defect densities larger than 40% is small. However, for smaller defect densities, the larger runs will dominate MQ dynamics. Nevertheless, since these runs will exhibit more damped behavior, we can hope to reproduce the essential features of the experimentally-observed oscillations.

Theoretical intensities of MQ coherences for an oriented spin system are calculated by using Eq. II-88. Figure II-36a and b show a comparison between the experimental 2Q intensities of single crystal FAP, and calculated 2Q intensities for assumed 30% and 50% defect densities at two different orientations (62° and 90° with respect to the external magnetic field) as a function of preparation time. The calculated 2Q intensities for both 30% and 50% defect densities at the two different orientations show similar oscillatory behaviors. Although the defect density of single crystal mineral fluorapatite cannot be reliably estimated, the agreement does not appear to improve as the defect density decreases from 50% to 30%, especially in the positions of the maxima and minima in Figure II-36a. A defect

density less than 30%, which is quite reasonable, would appear to yield even better agreement if the same trend occurs. ¹⁹F MQ NMR spectra of single crystal FAP (not shown here) at two orientations (62° and 90°) display 6Q peaks at shorter than 1ms. This indicates that a considerable mole fraction of larger than 6 spin systems is present in mineral single crystal FAP. Thus, since the sum of the mole fraction of defect densities larger than 50% is greater than 90%, we can presume that the defect density is less than 50%. The contribution of larger than 6 spin systems to the MQ dynamics hinders the reliable measurement of the defect density from comparisons between calculated and experimental plots. In spite of the existence of a variety of spin system in single crystal fluorapatite, the oscillatory behavior of MQ intensities of single crystal FAP in Fig. II-27 indicates that the fluorine atoms in chains are interrupted by defects.

6. Conclusions

We have shown that multiple-quantum dynamics in an essentially one-dimensional distribution of spins leads to an initial linear dependence of effective size N upon preparation time, in qualitative agreement with predictions of the incremental shell model. Turther work is needed to determine whether the lack of good quantitative agreement in this initial region arises from experimental considerations, or instead from limitations of the theoretical model, and whether further refinements of the model may improve its predictive accuracy. The MQ growth exponents also distinguish the different dimensionalities of spin systems and the presence of clustering. The contribution of the two different dimensionalities to the growth of the MQ coherences is visually illustrated by the MQ growth exponent plot. Two growth exponents of HAP-M agree well reasonably with those of the

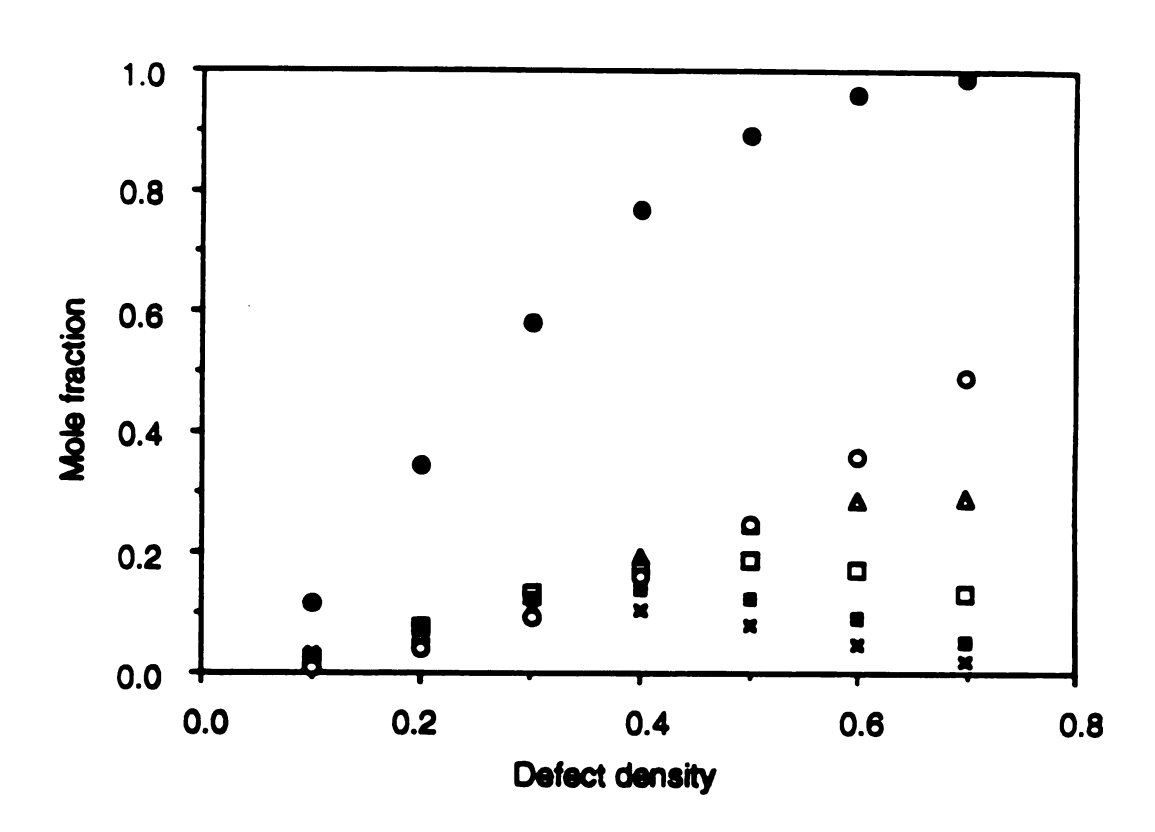


Figure II-35. Mole fraction of spins in various run numbers and sum of the mole fraction with different defect densities using percolation theory.⁷⁷ Run number = 1 (open circle), run number = 2 (open triangle), run number = 3 (open square), run number = 4 (cross in open square), run number = 5 (cross), and sum of 1 - 5 spins (black circle).

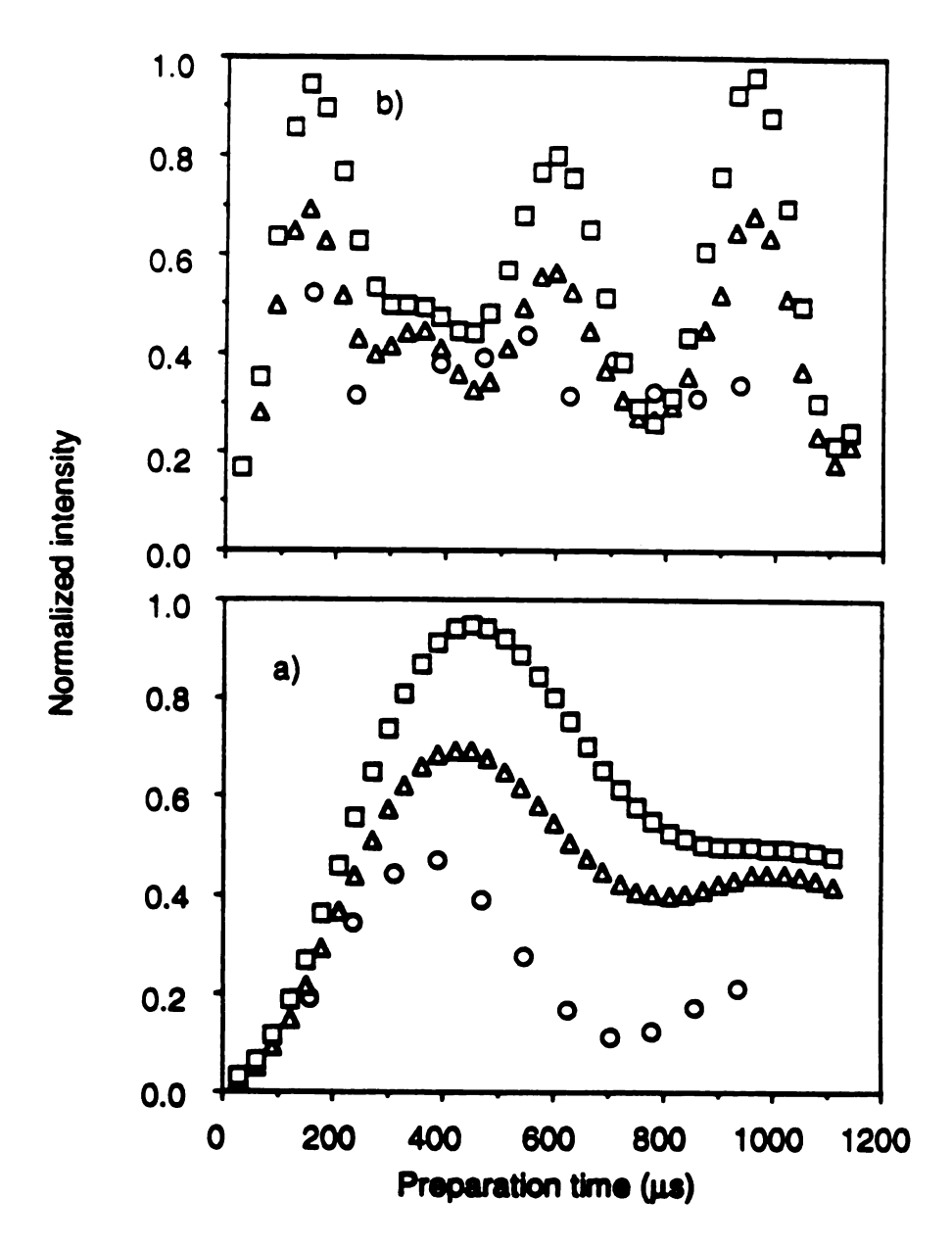


Figure II-36. Comparison between experimental 2Q intensities (open circle) of single crystal FAP and calculated 2Q intensities for two assumed defect densities [30% (open circle) and 50% (open square)] at two different orientations. a) 62° orientation with respect to the external magnetic field; b) 90° orientation with respect to the external magnetic field.

incremental shell model. Linear behavior of the effective sizes vs. preparation time has previously been observed generally only for finite clusters, but the slope at longer preparation times in these cases is observed to level off,⁵⁷ in contrast to our results. It is interesting to note that the hopping model also predicts a linear dependence for clusters of 21 spins, but it cannot treat infinite spin systems, and has not predicted MQ dynamics for different dimensionalities.

It is feasible to model the one-dimensional chains due to their simple configuration. ¹H MQ-NMR is sensitive to defects in one-dimensional apatite chains, and the defect density can be estimated by using the one-dimensional cluster model. The comparison of 4Q/2Q intensities between HAP-M and HAP-N for given preparation times directly shows the presence of vacancies in the non-stoichiometric hydroxyapatite sample. The defect density of HAP-N obtained using MQ NMR is in good agreement with the 8% defect density obtained from ¹H MAS-NMR;⁶⁸ however, the calculated 4Q/2Q intensities based on the defect densities of the FOHAP samples deviate considerably from MQ experimental 4Q/2Q intensities. This discrepancy may arise from three possible sources; additional defects in the hydroxyl chains other than fluorine atoms (i. e. vacancies), non-random fluorine substitutions, and/or off-resonance effects caused by dipolar coupling of the hydroxyl protons to ¹⁹F nuclei. Partially deuterated hydroxyapatite could be used to test the 1-D cluster model with knowledge of the hydroxyl content, since a deuterium randomly substitutes for a proton and the dipolar interaction between a deuterium and a proton is small. The first explanation could be tested by a detailed chemical analysis of the hydroxyl content of the crystals, which is quite difficult to perform.

Since the dipolar interaction in single crystal samples can be adjusted by

field, we hope that ¹⁹F MQ NMR of single crystal fluorapatite could be used to separate the MQ dynamics of different dimensionalities. For example, if the orientation of intra-chain fluoride ions is fixed at 54.7° (magic angle), the non-zero dipolar coupling of inter-chain fluoride ions would create MQ coherence in a 2-D or fashion. Our ¹⁹F MQ-NMR results for a single crystal of mineral FAP show an oscillatory behavior of the MQ peaks that does not permit measurement of the effective size at each preparation time. A less deficient synthetic single crystal sample might give information about dimensionality in more detail. Since the orientation of individual crystallites can be selected by relating them to a position in the CSA powder pattern, MQ-NMR can be performed on a specific orientation by selectively saturating all but a single frequency in the pattern.⁷⁹ Selecting the orientation in a powdered sample thus also permits the relative magnitude of the

intra- and inter-chain dipolar couplings to be "tuned" at will.

7. References

- 1. W. A. Anderson, Phys. Rev. 104, 850 (1956)
- 2. J. I. Kaplan and S. Meiboom, *Phys. Rev.* 109, 499 (1957)
- 3. S. Yatsive. Phys. Rev. 113, 1522 (1959).
- 4. W. A. Anderson, R. Freeman, and C. A. Reilly, *J. Chem. Phys.* **39**, 1518 (1963).
- 5. K. A. McLauchlan and D. H. Whiffen, Proc. Chem. Soc., 144 (1962).
- 6. A. D. Cohen and D. H. Whiffen, Mol. Physics, 7, 449 (1964).
- 7. J. I. Musher, J. Chem. Phys. 40, 983 (1964).
- 8. M. L. Martin, G. J. Martin, and R. Couffignol, J. Chem. Phys. 49, 1985 (1968).
- 9. K. M. Worvill, J. Magn. Reson. 18, 217 (1975).
- 10. P. Bucci, M. Martinelli, and S. Santucci, J. Chem. Phys. 52, 4041 (1970).
- 11. P. Bucci, M. Martinelli, and S. Santucci, J. Chem. Phys. 53, 4524 (1970).
- 12. G. Lindblom, H. Wennerstroem, and B. Lindman, J. Mag. Reson. 23, 177 (1976)
- 13. R. B. Creel, E. D. von Meerwall, and R. G. Barnes, *Chem Phys. Lett.* **49**, 501 (1977).
- D. Dubber, K. Deorr, H. Ackmann, F. Fujara, H. Grupp, M. Grupp, P. Heitjans,
 A. Keoblein, and H. J. Steockmann, Z. Physik A, 282, 243 (1977).
- 15. R. R. Ernst and W. A. Anderson, Rev. Sci. Instr. 37, 93 (1966).
- 16. H. Hatanaka, T. Terao, and T. Hashi, J. Phys. Soc. Jpn. 39, 835 (1975).
- 17. W. P. Aue, E. Bartholdi, and R. R. Ernst, J. Chem. Phys. 64, 2229 (1976)
- 18. G. Bodenhausen., Prog. NMR Spectrosc. 14, 137 (1981).
- U. Piantini, O. W. Sorenson, and R. R. Ernst, J. Am. Chem. Soc. 104, 6800 (1982).

- 20. A. Bax, R. Freeman, and S. P. Kempsell, *J. Am. Chem. Soc.* **102**, 4849 (1980).
- 21. A. Bax, R. Freeman, and S. P. Kempsell, J. Magn. Reson. 41, 349 (1980).
- 22. A. Bax, R. Freeman, T. A. Frenkiel, and M. H. Levitt, *J. Magn. Reson.* 43, 478 (1981)
- 23. A. Bax, R. Freeman, and T. A. Frenkiel, *J. Am. Chem. Soc.* **103**, 2102 (1981).
- 24. L. Braunschweiller, G. Bodenhausen, and R. R. Ernst, *Mol. Phys.* 48, 535 (1983).
- 25. M. H. Levitt and R. R. Ernst, Chem. Phys. Lett. 100, 109 (1983).
- 26. W. S. Warren, D. P. Weitekamp, and A. Pines, *J. Chem. Phys.* **73**, 2084 (1080).
- 27. W. S. Warren and A. Pines, *J. Chem. Phys.* **74**, 2808 (1981).
- 28. S. Sinton, D. B. Zax, J. B. Murdoch, and A. Pines, Mol. Phys. 53, 333 (1984).
- W. S. Warren, S. Sinton, D. P. Weitekamp, and A. Pines, *Phys. Rev. Lett.* 43, 1792 (1979).
- 30. Y. S. Yen and A. Pines, J. Chem. Phys. 66, 5624 (1983).
- 31. J. Baum, M. Munowitz, A. N. Garroway, and A. Pines, *J. Chem. Phys.* **83**, 2015 (1985).
- 32. A. N. Garroway, J. Baum, M. Munowitz, A. Pines, *J. Magn. Reson.* **60**, 337 (1984).
- 33. J. Baum, K. K. Gleason, A. Pine, A. N. Garroway, and J. A. Reimer, *Phys. Rev. Lett.* **56**, 1377 (1986).
- 34. K. K. Gleason, M. A. Petrich, and J. A. Reimer, *Phys. Rev. B.* **36**, 3259 (1987).

- 35. M. A. Petrich, K. K. Gleason, and J. A. Reimer, *Phys. Rev. B.* **36**, 9722 (1987).
- 36. D. H. Levy and K. K. Gleason, J. Phys. Chem. 96, 1992 (1992).
- 37. G. Drobny, A. Pines, S. Sinton, D. P. Weitekamp, and D. Wemmer, *Faraday Symp. Chem. Soc.* **13**, 49 (1979).
- 38. R. Ryoo, S.-B. Liu, L. C. de Menorval, K. Takegoshi, B. Chmelka, M. Trecoske, and A. Pines, *J. Phys. Chem.* **91**, 6575 (1987).
- B. Chmelka, J. G. Pearson, S.-B. Liu, R. Ryoo, L. C. de Menorval, and
 A. Pines, J. Phys. Chem. 95, 303 (1991).
- 40. D. N. Shykind, J. Baum, S.-B. Liu, A. Pines, and A. N. Garroway, *J. Magn. Reson*.

76, 149 (1988).

- 41. S. Sinton and A. Pines, Chem. Phys. Lett. 76, 263 (1980).
- 42. M. Munowitz and A. Pines, Science 233, 525 (1986).
- 43. W. V. Gerasimowicz, A. N. Garroway, and J. B. Miller, *J. Am. Chem. Soc.*112, 3726 (1990).
- 44. B. E. Scruggs and K. K. Gleason, *J. Magn. Reson.* **99**, 149 (1992).
- 45. B. E. Scruggs and K. K. Gleason, *Macromolecules*, **25(7)**, 1864 (1992).
- 46. M. Goldman, "Quantum Description of High-Resolution NMR in Liquids" (Oxford University Press, New York, 1988).
- 47. C. P. Slichter, "Principles of Magnetic Resonance", 3rd ed. (Springer-Verlag, New-York, 1989).
- 48. R. R. Ernest, G. Bodenhausen and A. Wokaun, "Principles of Nuclear

 Magnetic Resonance in One and Two Dimensions" (Oxford University Press,

 New York, 1987).

- 49. D. P. Weitekamp, Adv. Magn. Reson. 11, 111 (1983).
- 50. M. Munowitz, Mol. Phys. 71, 959 (1990).
- 51. B. E. Scruggs and K. K. Gleason, *Chem. Phys.* **166**, 367 (1992).
- 52. M. Munowitz and A. Pines, Adv. Chem. Phys. 66, 1 (1987).
- 53. S. Lacelle, Advances in Magnetic and Optical Resonance 16, 173 (1991).
- 54. A. Wokaun and R. R. Ernst, Mol. Phys. 36, 317 (1978).
- 55. J. Baum and A. Pines, J. Am. Chem. Soc. 108, 7447 (1986).
- 56. J. B. Murdoch, W. S. Warren, D. P. Weitekamp and A. Pines, *J. Mag. Reson.*60, 205 (1984).
- 57. M. Munowitz, A. Pines, and M. Mehring, J. Chem. Phys. 86, 3172 (1987).
- 58. M. I. Kay, R. A. Young and A. S. Posner, *Nature (London)*, **204**, 1050 (1964).
- 59. J. C. Elliott, P. E. Mackie, and R. A. Young, *Science*, **180**, 1055 (1980).
- 60. A. Abragam, "Principles of Nuclear Magnetism" Oxford Univ. Press, Oxford (1961).
- 61. M. Munowitz, "Coherence and NMR" Wiley, New York (1988).
- 62. J. von Neumann, "Mathematical Foundations of Quantum Mechanics", Princeton University Press, Princeton, NJ (1955).
- 63. U. Haeberlen, "High Resolution NMR in Solids: Selective Averaging", *Adv. Magn. Reson.*, Supplement 1, . Academic Press, New York (1976).
- 64. U. Haeberlen and J. S. Waugh, Phys. Rev. 175, 453 (1968).
- 65. J.L. Carolan, Chem. Phys. Lett. 12 (1971) 389.
- 66. F. S. de Bouregas and J. S. Waugh, *J. Magn. Reson.* **96**, 280 (1992)
- 67. B.O. Fowler, Inorg. Chem. 13 (1974) 207.
- 68. J. Arends, J. Christofferson, M. R. Christofferson, H. Eckert, B. O. Fowler,
 - J. C. Heughebaert, G. H. Nancollas, J. P. Yesinowski and S. J. Zawacki,

- J. Cryst. Growth 84, 515 (1987).
- 69. J. P. Yesinowski and H. Eckert, J. Am. Chem. Soc. 109, 6274 (1987).
- 70. E.C. Moreno, M. Kresak, and R.T. Zaradnik, Caries Res. Suppl.1 142 (1977)
- 71. J.P. Yesinowski and M.J. Mobley, J. Am. Chem. Soc.105 6191 (1983);
 J.P. Yesinowski, R. Wolfgang, and M.J. Mobley, in Adsorption on and
 Surface Chemistry of Hydroxyapatite, Misra, D. N., Ed., Plenum: New York,
 pp151–175.
- 72. R. W. C. Wyckoff, *Crystal Structures (Interscience New York)*, **6**, part 1, 386 (1963).
- 73. E. R. Andrew, J. Chem. Phys. 18, 607 (1950).
- 74. L. B. Schreiber and R. W. Vaughan, Chem. Phys. Lett., 28, 586 (1974).
- 75. K. K. Gleason, Concepts in Magn. Reson. Appeared.
- 76. W. Van der Lugt, D. I. M. Knottnerus, and W. G. Perdok, *Acta Crysallogr., Sect. B: Crystallogr. Cryst. Chem.* **B27**, 1509 (1971).
- 77. A. M. Vakhrameev, S. P. Gaguda, and R. G. Knubovets, *J. Struct. Chem.* (Engl. Transl.), **19**, 256 (1978).
- 78. D. Stauffer and A. Aharony, "Introduction to Percolation Theory" Taylor & Francis, London, Washington, DC (1992).
- 79. L. B. Moran and J. P. Yesinowski, Chem. Phys. Lett., To be submitted.

APPENDIX A

= getval("delp");

delp

Pulse program for even-order selective phase-incremented or TPPI multiplequantum pulse sequence for solids for Varian VXR spectrometer. This program is courtesy of T. Barbara of Varian Associate.

```
/*Pulse sequence: G_INMQ_LOCK*/
/*Pseudo 1-D even order MQ generation with a detection using spin locking sequence.
Phase cycle to remove odd order quanta by alternating excitation phase between x and
-x and adding memory.*/
/* VARIABLES:
del: delay between 8 pulses \mus
delp: delay between 8 pulses, 2*del+pw \mu s
mloop: the number of loop (basic cycle time*mloop = preparation time)
shift: the angle phase incrementation (determine the maximum detectable MQ order)
tlinc: the time to increment the phase
d3: the time between mixing and detection period to eliminate the remaining transverse
magnetization
d4: the evolution time*/
#include <standard.h>
static int table 1[4] = \{0, 2, 2, 0\};
static int table 2[4] = \{ 0, 0, 2, 2 \};
static int table 3[4] = \{ 2, 0, 0, 2 \};
static int table 4[4] = \{1, 1, 3, 3\};
static int table 5[4] = \{3, 3, 1, 1\};
static int table 6[4] = \{0, 2, 0, 2\};
static int table 7[4] = \{1, 3, 1, 3\};
pulse sequence()
double del, delp, ddelp, mloop, shift, d3, d4, t1inc;
        trig[MAXSTR];
char
extern double getval();
        = getval("del");
del
```

```
mloop = getval("mloop");
shift
         = getval("shift");
d3
         = getval("d3");
d4
         = getval("d4");
         = getval("tlinc");
tlinc
getstr("trig",trig);
ddel
        = del - rof1 - rof2;
ddelp = del - rof1 - rof2;
settable(t1, 4, table1);
settable(t2, 4, table2);
settable(t3, 4, table3);
settable(t4, 4, table4);
settable(t5, 4, table5);
settable(t6, 4, table6);
settable(t7, 4, table7);
setreceiver(t7);
stepsize(shift,TODEV);
initval(mloop,v1);
initval(np/2.0,v7);
initdelay(tlinc,DELAY5);
assign(zero,v10);
loop(v7,v9);
if(trig[0]=='y')
{
  xgate(1.0);
}
xmtrphase(v10);
delay(d1); delay(rof1);
incr(v10);
rcvroff();
starthardloop(v1);
delay(ddel);
rgpulse(pw,t1,rof1,rof2); /* x -x -x x */
delay(ddelp);
rgpulse(pw,t1,rof1,rof2);
delay(ddel);
rgpulse(pw,t1,rof1,rof2);
delay(ddelp);
```

```
rgpulse(pw,t1,rof1,rof2);
delay(ddel);
rgpulse(pw,t3,rof1,rof2); /* -x x x -x */
delay(ddelp);
rgpulse(pw,t3,rof1,rof2);
delay(ddel);
rgpulse(pw,t3,rof1,rof2);
delay(ddelp);
rgpulse(pw,t3,rof1,rof2);
endhardloop();
xmtrphase(zero); /* reset small angle shift to zero */
delay(d4);
                                /* generate t1 delay If tlinc=0, TPPI*/
incdelay(v10,DELAY5);
                                   /*otherwise, phase incremented method*/
starthardloop(v1);
 delay(ddel);
 rgpulse(pw,t4,rof1,rof2); /* y y -y -y */
 delay(ddelp);
 rgpulse(pw,t4,rof1,rof2);
 delay(ddel):
 rgpulse(pw,t4,rof1,rof2);
 delay(ddelp);
 rgpulse(pw,t4,rof1,rof2);
delay(ddel);
rgpulse(pw,t5,rof1,rof2); /* -y -y y y */
delay(ddelp);
rgpulse(pw,t5,rof1,rof2);
delay(ddel);
rgpulse(pw,t5,rof1,rof2);
delay(ddelp);
rgpulse(pw,t5,rof1,rof2);
endhardloop();
rcvron();
                  /* delay to allow decay of transverse coherences */
delay(d3);
rgpulse(pw, t6, rof1, rof2); /* x -x x -x */
rgpulse(p1, t7, rof1, rof2); /* y -y y -y spin locking*/
delay(alfa);
acquire(2.0,1/sw);
endloop(v9);
```

APPENDIX B

Selection rule of 1-spin/2-quantum average Hamiltonian Hyx in hopping model

If the spin angular momentum operator I_{α} is expressed for a spin with index s_j by a ket $|s_j\alpha_j\rangle$, the Liouville state that is formed is a product of K single-spin operators that can be written by the abbreviated notation

$$|Knp\rangle = |s_1\alpha_1 \cdots s_k\alpha_k\rangle \tag{A-1}$$

where

$$n = \sum_{j=1,K} \alpha_j. \tag{A-2}$$

The scalar product between two Liouville state vectors is orthornormal and is defined as

$$(A|B) = Tr\{A^+B\} \tag{A-3}$$

where A^+ is the Hermitian adjoint of A. Since the superoperator $\hat{\hat{\mathcal{H}}}$ is defined by

$$\hat{\mathcal{H}}(A) = |[\mathcal{H}, A]|, \tag{A-4}$$

matrix elements involving the superoperator are given by

$$\left(A\middle|\hat{\mathcal{H}}\middle|B\right) = \left(A\middle|\left[\hat{\mathcal{H}},B\right]\right) = Tr\{A^{+}[\mathcal{H},B]\}. \tag{A-5}$$

The selection rules in the Liouville space from the Hamiltonian in Eq. II-47 are calculated using Eq. A-5 and the commutation relations

$$[I_{zi}, I_{\pm j}] = I_{\pm}\delta_{ij} \tag{A-6a}$$

and

$$[I_{+i}, I_{-j}] = 2I_z \delta_{ij}$$
 (A-6b)

Since the selection rule of the average dipolar Hamiltonian from the pulse sequence in Fig. II-4 can be evaluated using the numerator of Eq. II-47, we can rewrite Eq. A-5 as

$$\left(Knp\middle|\hat{\mathcal{H}}_{D}\middle|K'n'p'\right) = \left(Knp\middle|\left[\hat{\mathcal{H}}_{D}, K'n'p'\right]\right). \tag{A-7}$$

After $K^{'}=1$ and $n^{'}=0$ (I_{1z}) is chosen as an initial condition, the square bracket

part of Eq. A-7 can be written using only the spin operators

$$[I_{+1}I_{+2} + I_{-1}I_{-2}, I_{1z}] = [I_{+1}I_{+2}, I_{1z}] + [I_{-1}I_{-2}, I_{1z}]$$
(A-8)

using a commutator algebra

$$[A, B + C] = [A, B] + [A, C].$$
 (A-9)

Since I_{+2} and I_{-2} commute with I_{1z} , we can rewrite Eq. A-8 using the commutation relations in Eq. A-6 as

$$= I_{+2}[I_{+1}, I_{1z}] + I_{-2}[I_{-1}, I_{1z}] = -I_{+2}I_{+1} - I_{-2}I_{-1}$$
(A-10)

$$[A, BC] = [A, B]C + B[A, C].$$
 (A-11)

The values of K and n of the first term in Eq. A-10 are 2 and 2, and those of the second term in Eq. A-10 are 2 and -2 respectively. Therefore, the solution of Eq. A-7 is

$$= \langle Knp| - I_{+2}I_{+1} - I_{-2}I_{-1} \rangle = \langle Knp|2, 2, p' \rangle + \langle Knp|2, -2, p' \rangle. \tag{A-12}$$

Since the scalar product of the Liouville state is orthonormal, Eq. A-12 is non-zero at K=2, n=2 and K=2, n=-2.

When K'=2 and n'=2 (from the $I_{+2}I_{+1}$ term), $\left[\mathcal{H}_D,K'n'p'\right]$ can be also written using the spin operators

$$[I_{+1}I_{+2} + I_{-1}I_{-2}, I_{+2}I_{+1}] = [I_{+1}I_{+2}, I_{+2}I_{+1}] + [I_{-1}I_{-2}, I_{+2}I_{+1}]$$
(A-13)

Since the first term $[I_{+1}I_{+2}, I_{+2}I_{+1}]$ commutes, we solve for the second term $[I_{-1}I_{-2}, I_{+2}I_{+1}]$ using Eq. A-11

$$=I_{+2}[I_{-1}I_{-2},I_{+1}]+[I_{-1}I_{-2},I_{+2}]I_{+1}=-I_{+1}I_{-1}I_{2z}+I_{1z}I_{-2}I_{+2}$$
(A-14)

Therefore, only when K=3 and n=0 is $\langle Knp|\mathcal{H}_D|2,2,p\rangle$ non-zero. The detailed calculation of the selection rule for K'=2 and n'=-2 is omitted since it is similar to the calculation of the selection rule for K'=2 and n'=2. Only when K=3 and n=0 is $\langle Knp|\mathcal{H}_D|2,-2,p\rangle$ non-zero too.

We will calculate the general solution of the selection rule using Eq. A-7. The square bracket in Eq. A-7 can be represented by

$$\left[\mathcal{H}_{D}, K' n' p'\right] = \left[\sum_{i>j} (I_{+i} I_{+j} + I_{-i} I_{-j}), K' n' p'\right]$$
 (A-15)

We can rewrite Eq. A-15 using Eq. A-9 and A-11 as

$$= \sum_{i>j} I_{+i} \Big[I_{+j}, K'n'p' \Big] + \sum_{i>j} \Big[I_{+i}, K'n'p' \Big] I_{+j}$$

$$+ \sum_{i>j} I_{-i} \Big[I_{-j}, K'n'p' \Big] + \sum_{i>j} \Big[I_{-i}, K'n'p' \Big] I_{-j}.$$
(A-16)

The solutions of $\sum\limits_{i>j}\left[I_{+j},K^{'}n^{'}p^{'}\right]$ and $\sum\limits_{i>j}\left[I_{+i},K^{'}n^{'}p^{'}\right]$ do not change the value of $K^{'}$ but change $n^{'}$ to $n^{'}+1$ due to the commutation relations (Eq. A-6a and A-6b). The lowering operators in the square brackets of Eq. (A-16) do not change the value of $K^{'}$ but decrease $n^{'}$ to $n^{'}-1$. Since the operators outside the square brackets in Eq. A-16 increase $K^{'}$ to $K^{'}+1$, and change $n^{'}$ to $n^{'}\pm1$ according to $\left\langle Knp|\mathcal{H}_{D}|K^{'}n^{'}p^{'}\right\rangle$ is non-zero when K is equal to $K^{'}+1$ and n is equal to $n^{'}\pm2$.

When we solve the Eq. A-7 as $\Big(Knp|\mathcal{H}_D|K^{'}n^{'}p^{'}\Big)=\Big([Knp,H_D]|K^{'}n^{'}p^{'}\Big)$, the non-zero condition of $\Big\langle Knp|\mathcal{H}_D|K^{'}n^{'}p^{'}\Big\rangle$ is that K is equal to $K^{'}-1$ and n is equal to $n^{'}\pm 2$.

Therefore, the selection rule of the average Hamiltonian \mathcal{H}_{yx} in the Liouville space is $K=K^{'}\pm 1$ and $n=n^{'}\pm 2$.

APPENDIX C

C programs for calculation of the ratio of 4Q/2Q intensities for a 1-D chain with different defect densities.

These programs calculate the ratio of the 4Q/2Q intensities of defect containing 1D chains for various preparation times using the statistical model, combined with percolation theory expressions that provide the mole fraction of spins in a run number.

```
/* Calculation of 4Q/2Q intensity using the statistical model and the percolation theory*/
#include <stdio.h>
#include <stdlib.h>
#include <math.h>
double x,y;
double exp(),sqrt(),exp2(),pow();
main()
{
 int i,j,n,l,m,p;
 float k,s,h,sum2,pp,sump2,sum2p,sum4,sump4,sum4p,rat2,rat4;
 char filename[20];
 FILE *fp;
 printf("Enter filename: \n");
scanf("%s",filename);
 fp=fopen(filename,"wr");
 printf("What is the ratio of the defect?\n");
 fprintf(fp,"What is the ratio of the defect?\n");
 scanf("%f",&k);
 fprintf(fp,"%f\n", k);
 printf("What is the maximum run number?\n");
fprintf(fp,"What is the maximum run number?\n");
 scanf("%d",&l);
```

```
fprintf(fp,"%d\n", 1);
 printf("What is the effective size?\n");
 fprintf(fp,"What is the effective size?\n");
scanf("%f",&h);
fprintf(fp,"%f\n", h);
s=1.0-k;
sum2=0.0;
sum 4=0.0;
sum2p=0.0;
sum4p=0.0;
/*The first part of Eq. II-82 for 2-Q intensity. The decimal number (effective size from
Gaussian function) cannot be used to calculate a factorial so that the round up values are
used.*/
if(h \le 6.0)
   for(i=2;i \le l;i++)
     x=(double)i;
     if(x \le h)
       {
        sum2+=x*pow(k,2.0)*pow(s,x)*fac(2*i)/(fac(i-2)*fac(i+2))/pow(4.0,x);
      else
        p=round(h);
        pp=(float)p;
        sum2 +=x*pow(k,2.0)*pow(s,x)*fac(2*p)/(fac(p-2)*fac(p+2))/pow(4.0,pp);
      }
   }
/*The first part of Eq. II-82 for 4-Q intensity. The decimal number (effective size from
Gaussian function) cannot be used to calculate a factorial so that the round up values are
used.*/
```

for(i=4;i<=l;i++)

```
x=(double)i;
     if(x \le h)
     {
        sum4 +=x*pow(k,2.0)*pow(s,x)*fac(2*i)/(fac(i-4)*fac(i+4))/pow(4.0,x);
       else
      {
        p=round(h);
       pp=(float)p;
       sum4 +=x*pow(k,2.0)*pow(s,x)*fac(2*p)/(fac(p-4)*fac(p+4))/pow(4.0,pp);
     }
   }
}
/*The second part of Eq. II-82 for 2-Q and 4Q intensity. */
else
for(i=2;i<=6;i++)
{
 x=(double)i;
 sum2p +=x*pow(k,2.0)*pow(s,x)*fac(2*i)/(fac(i-2)*fac(i+2))/pow(4.0,x);
 for(i=4;i<=6;i++)
   x=(double)i;
  sum4p +=x*pow(k,2.0)*pow(s,x)*fac(2*i)/(fac(i-4)*fac(i+4))/pow(4.0,x);
  for(i=7;i \le l;i++)
   x=(double)i;
  if (x \le h)
    {
     sum2p +=x*pow(k,2.0)*pow(s,x)/(sqrt(x)*1.77)*exp(-4.0/x);
      sum4p +=x*pow(k,2.0)*pow(s,x)/(sqrt(x)*1.77)*exp(-16.0/x);
     }
  else
        sum2p +=x*pow(k,2.0)*pow(s,x)/(sqrt(h)*1.77)*exp(-4.0/h);
```

```
sum4p +=x*pow(k,2.0)*pow(s,x)/(sqrt(h)*1.77)*exp(-16.0/h);
    }
  }
}
printf("The ratio of each multiple quantum signal\n");
fprintf(fp,"The ratio of each multiple quantum signal\n");
sump2=(sum2+sum2p)/(sum2+sum2p);
sump4=(sum4+sum4p)/(sum2+sum2p);
printf("2quantum ==> %f, 4quantum ==> %f\n",sump2,sump4);
fprintf(fp,"2quantum ==> %f, 4quantum ==> %f\n",sump2,sump4);
fclose(fp);
}
/*Calculation of factorial*/
      fac(m)
     int m;
      {
        int i, fac;
        fac=1;
        for(i=1;i \le m;i++)
         fac=fac*i;
        return(fac);
      }
/* Calculation of round up*/
     round(x)
     float x;
        int ix;
        float fx, gx;
       gx=x;
       ix=(int)gx;
      fx=(float)ix;
     gx=fx;
       if(gx >= 0.5) ix += 1;
      return(ix);
     }
```

MICHIGAN STATE UNIV. LIBRARIES
31293010269862